ABSTRACT

ELECTRON BEAM SHAPING AND ITS APPLICATIONS

Aliaksei Halavanau, Ph.D.
Department of Physics
Northern Illinois University, 2018
Philippe Piot, Director

Transverse and longitudinal electron beam shaping is a crucial part of high-brightness electron accelerator operations. In this dissertation, we report on the corresponding beam dynamics research conducted at Fermilab Accelerator Science and Technology facility (FAST) and Argonne Wakefield Accelerator (AWA). We demonstrate an experimental method for spatial laser and electron beam shaping using microlens arrays (MLAs) at a photoinjector facility. Such a setup was built at AWA and resulted in transverse emittance reduction by a factor of 2. We present transverse emittance partitioning methods that were recently employed at FAST facility. A strongly coupled electron beam was generated in an axial magnetic field and accelerated in 1.3 GHz SRF cavities to 34 MeV. It was then decoupled in Round-To-Flat beam transformer and beams with emittance asymmetry ratio of 100 were generated. We introduce the new methods of measuring electron beam canonical angular momentum, beam transformer optimization and beam image analysis. We also describe a potential longitudinal space-charge amplifier setup for FAST high-energy beamline. As an outcome, a broadband partially coherent radiation in the UV range could be generated.

NORTHERN ILLINOIS UNIVERSITY
DE KALB, ILLINOIS

AUGUST 2018

ELECTRON BEAM SHAPING AND ITS APPLICATIONS

BY

ALIAKSEI HALAVANAU

A DISSERTATION SUBMITTED TO THE GRADUATE SCHOOL

IN PARTIAL FULFILLMENT OF THE REQUIREMENTS

FOR THE DEGREE

DOCTOR OF PHILOSOPHY

DEPARTMENT OF PHYSICS

Dissertation Director:
Philippe Piot

ACKNOWLEDGEMENTS

First and foremost I would like to express appreciation to my dissertation advisor Philippe Piot for his enormous patience and encouragement throughout my graduate student journey. I am grateful to my Fermilab mentors Charles Thangaraj and Daniel Mihalcea for the useful discussions and help with Elegant and Impact-T simulations. I would like to thank NIU faculties Stephen Martin, David Hedin, Jahred Adelman, Michael van Veenendaal, and Andreas Glatz for their excellent classes. I appreciate all the hard work and help of Fermilab scientists Vladimir Shiltsev, Alexander Valishev, Alexander Romanov, Alexander Shemyakin, Valery Lebedev and Sergei Nagaitsev during my PARTI-2011 summer internship and Joint Fermilab-University PhD program. I am indebted to Wei Gai, John Power, Eric Wisniewski, Charles Whiteford, Nicole Neveu, Gwanghui Ha and the rest of the Argonne Wakefield Accelerator group for the excellent experience and superb efficiency during my time there. This dissertation would be impossible without the previous work done by Marwan Rihaoui, Yin-e Sun, Timothy Maxwell and Christopher Prokop. I want to thank Anthony Gee, my partner in crime, who I shared the NICADD office with during long overnighters, my fellow Physics graduate students Francois Lemery, Harsha Panuganti, Ivan Viti, Tyler Burch, Daniel Stange, Graham Stoddard, Jing Xu and Andrew Palm for being great friends. I am thankful to Elon R. Musk of SpaceX who motivated me to work harder and set aspirational goals. I was lucky to meet Tracie and Drew Wells and participate in The Doorstep Project in DeKalb. It has been a privilege to play in NIU Men's Soccer club and in particular with Marvin Vargas and Mikael Ayele. ¡Gracias amigos! I am wholeheartedly grateful to my one and only Xiaoling Xiang, for endless, invaluable and unconditional support which was absolutely crucial during my graduate student career. This work is supported by the US Department of Energy under contract No. DE-SC0011831 with Northern Illinois University. The facilities

used during this research at Fermilab and Argonne National Laboratories are respectively operated by the US Department of Energy under contracts No. DE-AC02-06CH11357 and AC02-07CH11359.

DEDICATION

I dedicate this dissertation to my mother who fostered my interest in Science.

TABLE OF CONTENTS

LIST OF TABLES

LIST OF FIGURES

Figure Page

Figure Page

Figure Page

Figure Page

Figure Page

Figure Page

CHAPTER 1

ACCELERATOR AND BEAM PHYSICS CONCEPTS

Electron accelerators have been an active topic of research since the 1930s. They have become an inseparable part of material science, medicine, homeland security and fundamental science. The first electron accelerators were high static-voltage Cockroft-Walton/Van de Graaff generators that produced electrons in the keV-energy range. Modern accelerators based on electromagnetic (EM) field acceleration can provide electron beams in the sub-TeV range, and future machines are expected to reach TeV and possibly PeV energies. With rapid progress of acceleration technology, electron beam shaping remains a vitally important method for delivering beams with the required specifications in different applications. Below are the areas of Accelerator Physics where the results reported in this dissertation can be directly applied.

Electron beam transport. Radio frequency (RF) and superconducting RF (SRF) technologies remain the major accelerating techniques in current generation machines. In the last 20 years, the advancements in SRF acceleration drastically increased the energy efficiency and reduced the footprints of electron accelerators. The 1.3-GHz SRF accelerating cavity was originally developed in the context of the TESLA linear-collider project [1]. It was included in the baseline design of the future International Linear Collider (ILC) [2] and in the design of various other operating or planned accelerator facilities. Projects based on such a cavity include electron- [2, 3], muon- [4], and proton-beam accelerators [5] supporting fundamental science and compact high-power industrial electron accelerators [6]. A modern 1.3 GHz SRF accelerating cavity provides a gradient of up to 45 MeV/m. When combined with other cav-

ities in series it forms a cryomodule. The backbone of the ILC is such a cryomodule which consists of 8 cavities operating at 32 MeV/m. An ILC-type cryomodule was first commissioned with the operational parameters at the Fermilab Accelerator Science and Technology (FAST) facility as a main part of the electron injection beamline for the Integrable Optics Test Accelerator (IOTA) [7]. Electron beam transport properties of a single ILC-type cavity are discussed in this work.

Electron machines also serve as test accelerators for advanced nonlinear beam optics development. IOTA is such an accelerator that is being commissioned at the FAST facility. IOTA nonlinear lattice design requires 150 MeV electron beams to be delivered by FAST electron injector. It will comprise a nonlinear magnet in its beamline to achieve accelerator optics integrability. The transport properties and the injector beamline optimization were investigated as a part of this dissertation.

Photoinjectors. Currently there are three main types of electron sources that are distinguished by the emission process: thermionic ("hot") emission, field ("cold") emission and photoemission. Each of the emission types have their own areas of application. Particle distribution mimicking the original laser distribution is the advantage of a photoemission RF-gun. The process of generating photoelectrons with the ultraviolet (UV) laser starts at a metallic or semiconductor plate (photocathode) with high a quantum efficiency. When a plate is impinged on by a laser pulse, photoelectrons are born in the bulk of a plate material and overcome the vacuum potential barrier. They freely drift to the surface where they are dragged out of the metal with a strong electric field due to Schottky effect. In a typical source, electrons are initially accelerated, then focused with a solenoidal magnetic field and the entire setup forms a photoemission RF-gun. Typically such a setup produces 5-10 MeV photoelectrons within ~50 cm for further acceleration downstream of the machine.

Photoemission electron sources serve in an increasing number of applications including, accelerator-based light sources, ultra-fast electron diffraction setups, high-energy particle

accelerators, including the FAST injector and Argonne Wakefield Accelerator (AWA). For a given photoemission electron-source design, the beam properties, notably its brightness, are ultimately limited by the initial conditions set by the laser pulse impinging on the photocathode. Nonuniformities in the transverse electron-beam density can lead to transverse emittance dilution or intricate correlations. A challenge common in most applications is the ability to produce an electron beam with uniform transverse density. Generating and transporting a laser pulse while preserving a homogeneous transverse density is challenging and has been an active area of work. For instance, producing UV laser pulses requires the use of a nonlinear conversion process of amplified infrared (IR) pulses. This frequency upconversion mechanism often introduces transverse inhomogeneities owing to the nonlinearity of the conversion. In this dissertation we discuss a mechanism of improving the electron beam quality by shaping the laser transverse profile.

Electron and electron-ion colliders. Electrons or positrons are elementary particles meaning they do not possess any known internal structure. Colliding electrons or positrons poses an excellent opportunity for further exploration of the fundamental natural forces. As proton colliders approach their technological limits, multiple future electron collider projects have been proposed (e.g. ILC, JLEIC [8]). Such a facility, when completed, will be able to produce and register processes with much smaller cross sections than current generation colliders. They will recreate the conditions and processes that occured in the early Universe aiding in exploration of fundamental natural phenomena. Improved transverse and longitudinal uniformity of an electron beam increases the number of collisions per second and therefore the total luminosity of such a collider.

Electron beams are commonly used for cooling of proton and ion beams [9, 10]. Conventional electron cooling process includes an electron beam co-propagated with a proton or ion beam. In the beam's rest frame electron charge density exerts Coulomb force on the

protons/ions. Such beamline sections are called electron lenses and were famously developed and tested at Fermilab to increase proton beam quality in Tevatron collider.

Prevalent angular motion ("magnetization") in electron beam increases the time of interaction and improves the cooling efficiency [11]. As a part of the future electron-ion colliders, a cooling section involving strong angular-momentum-dominated beams is proposed. This technique was initially developed at Fermilab's A0 facility [12, 13, 14]. Further improvements were researched at the FAST facility and are reported in this document. A mechanism of removal of angular motion or round-to-flat beam (RTFB) transformation can generate beams with better current profiles which also increase the luminosity of the future electron colliders and serve as alternative to electron damping rings. A method of "magnetized" beam generation and RTFB transformation are discussed theoretically and demonstrated experimentally in this dissertation.

Light sources. Electrons generate synchrotron radiation when moving on a bent trajectory. The total radiated power for a given beam energy depends on the relativistic Lorentz factor as $P \sim \gamma^4$. This effect is most prominent for electrons due to their relatively low mass. Synchrotron radiation produced by an electron beam, in general, has a broadband spectrum. However, when sent through an undulator, the radiation consists of coherent ultra-short intense pulses of X-rays that can unveal the intrinsic properties of matter beyond the scope of any other scientific instrument. Additionally, coherent synchrotron radiation can be produced in the THz range and used in medical tomography, structural diagnostics, and security cargo scanning. The electron accelerators tailored for such purposes are commonly referred as *light sources* and are widely employed in various configurations aroung the world.

Modern light sources require sophisticated beam shaping techniques to prepare the beam distribution in a way to maximize radiation power output. Such techniques involve dielectric wakefield beam current shaping, microbunching, space-charge corrections, emittance growth

mitigation, emittance exchange, electron-laser interaction, electron beam transverse shaping, etc. Many of these methods were developed at Fermilab, and in particular, a novel experimental radiation generation setup for FAST high energy beamline is considered numerically in this thesis. It can be applied elsewhere as a complimentary part of an electron linear accelerator.

1.1 Relativistic particle motion

In this chapter we will introduce accelerator elements and concepts that will be used throughout the text. Consider a motion of a particle with mass m, charge q, relativistic momentum $\boldsymbol{p}$ and located at $\boldsymbol{r}$ in the presence of an axially symmetric electro-magnetic field. In this case the Lorentz force will act on the particle as:

$$\boldsymbol{F}(\boldsymbol{r},t) = q[\boldsymbol{E}(\boldsymbol{r})\sin\Psi(t) + \boldsymbol{v}\times\boldsymbol{B}(\boldsymbol{r})\cos\Psi(t)], \tag{1.1}$$

where $\Psi(t) \equiv \omega t + \psi_0$ (with $\omega \equiv 2\pi f$), f is the frequency, $\boldsymbol{v}$ is the particle velocity, the external $(\boldsymbol{E},\boldsymbol{B})$-fields are generated by vector potential $\boldsymbol{A}$ as $\boldsymbol{B} = \nabla\times\boldsymbol{A}$ and scalar potential ϕ as $\boldsymbol{E} = -\nabla\phi - \frac{\partial\boldsymbol{A}}{\partial t}$. Since $\boldsymbol{p} = \gamma m\boldsymbol{v}$, where γ is the Lorentz factor, the motion of electron with $q = e$ can be described in a general form by the following equation of motion [15, 16, 17]:

$$\gamma m\frac{d\boldsymbol{v}}{dt} + m\boldsymbol{v}\frac{d\gamma}{dt} = e(-\nabla\phi - \frac{\partial\boldsymbol{A}}{\partial t} + \boldsymbol{v}\times\nabla\times\boldsymbol{A}) \tag{1.2}$$

Additionally, fields $(\boldsymbol{E},\boldsymbol{B})$ obey Maxwell's equations in a free space:

$$\nabla\times\boldsymbol{E} = -\frac{\partial\boldsymbol{B}}{\partial t}, \qquad \nabla\cdot\boldsymbol{B} = 0$$

Relativistic Hamiltonian of a relativistic particle in the presence of $(\boldsymbol{E}, \boldsymbol{B})$ fields generated by $(\boldsymbol{A}, \phi)$ potentials can then be written as [17]:

$$H = c(m^2c^2 + (\mathbf{p} - q\mathbf{A})^2)^{1/2} + e\phi - mc^2,$$

where c is the speed of light and $\boldsymbol{p}$ is the particle momentum. Note, that:

$$-\frac{\partial H}{\partial \theta} = \frac{dp_\theta}{dt} = 0,$$

therefore θ is a cyclic variable and $p_\theta = \gamma m r^2\dot{\theta} + erA_\theta = const$ is a **constant of motion**. p_θ is also commonly labeled as canonical angular momentum (CAM), and its conservation is also known as Busch's theorem [18]. It can be rewritten in the following form:

$$L = \gamma m r^2\dot{\theta} + \frac{1}{2}eB_z(z)r^2 + \mathcal{O}(r^4), \tag{1.3}$$

where L corresponds to the canonical angular momentum (CAM), $B_z(z)$ is the axial component of the magnetic field and (r, θ, z) are cylindrical coordinates. CAM beams have a variety of applications and can be further manipulated to form beams with asymmetric transverse emittances or flat beams [19].

1.2 Electron beam phase-space parameters

Electron motion can be fully characterized by its coordinates and momemnta in 6D phase-space (x, p_x, y, p_y, z, p_z). It is customary to define the 6D trace-space as $(x, x', y, y', z, \delta)$, where $x' \equiv p_x/p_z$ and $y' \equiv p_y/p_z$ due to significance of the p_z in comparison to other momemnta, and $\delta = \Delta p_z/p_z$ is the fraction momentum spread. The condition $p_z \gg p_{x,y}$ is also labeled as

paraxial approximation. Due to the implication of the Liouville's theorem, the total trace-space volume $d\Gamma \equiv dxdydzdx'dy'dp_z = const$ remains constant at all times in the accelerator.

Consider an ensemble of electrons travelling together at ultra-relativistic speeds. Such an ensemble is conventionally called electron *bunch* and is characterized by its total charge and statistical properties of its particle distribution.

Let particle density distribution in (x, x')-plane be described by $F(x, x')$. Then the following statistical central moments can be defined:

$$\langle x \rangle = \int_{-\infty}^{+\infty} \int_{-\infty}^{+\infty} xF(x, x')dxdx' \approx \frac{1}{N} \sum_{i=1}^{N} x_i \tag{1.4a}$$

$$\langle x' \rangle = \int_{-\infty}^{+\infty} \int_{-\infty}^{+\infty} x'F(x, x')dxdx' \approx \frac{1}{N} \sum_{i=1}^{N} x'_i \tag{1.4b}$$

$$\langle x^2 \rangle = \int_{-\infty}^{+\infty} \int_{-\infty}^{+\infty} x^2F(x, x')dxdx' \approx \frac{1}{N} \sum_{i=1}^{N} x_i^2 \tag{1.4c}$$

$$\langle x'^2 \rangle = \int_{-\infty}^{+\infty} \int_{-\infty}^{+\infty} x'^2F(x, x')dxdx' \approx \frac{1}{N} \sum_{i=1}^{N} x_i'^2 \tag{1.4d}$$

$$\langle xx' \rangle = \int_{-\infty}^{+\infty} \int_{-\infty}^{+\infty} xx'F(x, x')dxdx' \approx \frac{1}{N} \sum_{i=1}^{N} x_i x_i', \tag{1.4e}$$

where N is the number of particles in the bunch. Additionally, the quantities $\sigma_x = \sqrt{\langle x^2 \rangle}$ and $\sigma'_x = \sqrt{\langle x'^2 \rangle}$ are called distribution RMS size in (x, x'). Similarly, the calculation for $(y, y'), (x, y), (x', y), (xy'), (x'y')$ planes yields its second central statistical moments. First order moments $\langle x \rangle, \langle x' \rangle, \langle y \rangle, \langle y' \rangle$ are often assumed to be 0.

Longitudinal bunch distribution is also commonly described by its RMS bunch length $\sigma_z = \sqrt{\langle z^2 \rangle}$ and energy spread $\sigma_\delta = \sqrt{\langle \Delta\gamma^2 \rangle}/\langle \gamma_0 \rangle$, where γ_0 is the Lorentz factor of the

bunch's center of mass. To characterize longitudinal temporal profile, a *bunching factor* is defined as [20]:

$$b(\omega) = \frac{1}{N}\left|\sum_n \exp(-i\omega t_n)\right|, \tag{1.5}$$

where $t_n = z_n/c$ is the temporal coordinate of the n-th particle, N is the total number of particles and $\omega \equiv kc$.

1.2.1 Beam moments matrix

The second-order transverse statistical moments form a *covariance matrix* or *beam matrix*:

$$\mathbf{\Sigma} = \begin{pmatrix} \langle x^2\rangle & \langle xx'\rangle & \langle xy\rangle & \langle xy'\rangle \\ \langle x'x\rangle & \langle x'^2\rangle & \langle x'y\rangle & \langle x'y'\rangle \\ \langle yx\rangle & \langle yx'\rangle & \langle y^2\rangle & \langle yy'\rangle \\ \langle y'x\rangle & \langle y'x'\rangle & \langle y'y\rangle & \langle y'^2\rangle \end{pmatrix}. \tag{1.6}$$

From Eqs. (1.4) it can be concluded that the matrix (1.6) is symmetric. In case of a round beam at waist Eq. (1.6) takes a simplified diagonal form:

$$\mathbf{\Sigma} = \begin{pmatrix} \langle x^2\rangle & 0 & 0 & 0 \\ 0 & \langle x'^2\rangle & 0 & 0 \\ 0 & 0 & \langle y^2\rangle & 0 \\ 0 & 0 & 0 & \langle y'^2\rangle \end{pmatrix}. \tag{1.7}$$

Such a matrix obeys the condition of $|\mathbf{\Sigma}| \geq 0$. In case of a round uncoupled beam the beam matrix takes 2×2 block diagonal form. An upper(lower) block can be parameterized as

$$\mathbf{\Sigma_{2\times 2}} = \begin{pmatrix} \langle x^2 \rangle & \langle xx' \rangle \\ \langle x'x \rangle & \langle x'^2 \rangle \end{pmatrix} = \epsilon_x^2 \begin{pmatrix} \beta_x & -\alpha_x \\ -\alpha_x & \gamma_x \end{pmatrix}, \tag{1.8}$$

where $\epsilon_x = \sqrt{\langle x^2 \rangle \langle x'^2 \rangle - \langle xx' \rangle^2}$ is *geometric emittance* and $(\alpha_x, \beta_x, \gamma_x)$ are *Twiss* or *Courant-Snyder* parameters. Note, that $\gamma_x \equiv (1 + \alpha_x^2)/\beta_x$. The product of geometric emittances $\epsilon_x \epsilon_y$ is conserved. It is also useful to define a *normalized emittance* as $\epsilon_{nx} = \beta\gamma\epsilon_x$, where β is the beam velocity and γ - Lorentz factor. The ratio $B_\perp = Q/\epsilon_x\epsilon_y$, where Q is the bunch charge, is referred as the beam's transverse brightness. For the most of practical applications it is important to minimize beam emittance, and therefore maximize the beam brightness.

1.3 Accelerator beamline elements

In this section we will briefly review the common linear accelerator elements that are routinely used in electron beamlines. Eq. (1.2) can be rewritten in cylindrical coordinates as [17]:

$$r'' + g_1(z)r' + g_2(z)r - g_3(z)/r^3 = 0, \tag{1.9}$$

where r is the particle's radial coordinate $r = \sqrt{x^2 + y^2}$, $g_1(z) = \gamma'/\gamma\beta^2$, $g_2(z) = \gamma''/2\gamma\beta^2 + (e\boldsymbol{B}/2mc\beta\gamma)^2$, $g_3(z) = (p_\theta/mc\gamma\beta)^2$, $r' = \frac{dr}{dz}$. Eq. (1.9) can be linearized and a solution can be represented in a matrix form:

$$\begin{pmatrix} r_f \\ r'_f \end{pmatrix} = \begin{pmatrix} R_{11} & R_{12} \\ R_{21} & R_{22} \end{pmatrix} \begin{pmatrix} r_i \\ r'_i \end{pmatrix}, \tag{1.10}$$

where $\begin{pmatrix} r_{i,f} \\ r'_{i,f} \end{pmatrix}$ are initial(final) positions of a particle and $\boldsymbol{R}$ is the transport matrix. Under the transformation (1.10) the determinant of the beam matrix (1.6) is conserved:

$$|\boldsymbol{\Sigma_f}| = |\boldsymbol{R}\boldsymbol{\Sigma_0}\tilde{\boldsymbol{R}}| = |\boldsymbol{\Sigma_0}|,$$

where $\tilde{\boldsymbol{R}}$ is $\boldsymbol{R}$ transposed. In case of no acceleration applied, $g_1(z) = 0$, additionally when $p_\theta = 0$ the nonlinear term vanishes $g_3(z) = 0$, therefore the motion can be uncoupled and considered separately in (x, y, z)-space. The Eq. (1.9) then takes form:

$$x'' + K_x(s)x = 0, \qquad y'' + K_y(s)y = 0, \qquad z'' + K_z(s)z = 0, \tag{1.11}$$

where $K_{x,y,z}(s)$ is a function of path length s. Eqs. (1.11) is commonly referred as Hill's equations. The most general solution of the Hill's equation is a pseudo-harmonic oscillation. However, very often the solution is found in small oscillation amplitude approximation which corresponds to the paraxial approximation discussed above.

In practice, the solution of the Eq. (1.9) is found numerically for each particle in the distribution. The particle tracking codes used in this dissertation are ASTRA, IMPACT-T AND ELEGANT [21, 22, 23]. ASTRA and IMPACT-T solve the Eq. (1.9) directly, while ELEGANT is based on transfer matrices approach.

A typical accelerator consists of an electron source and solenoidal lenses, which form electron gun, along with drift spaces, dipole and quadrupole magnets, and accelerating cavities. Additionally, accelerators can also include sextupole and octupole magnets for abberations compensation. Most of the accelerator-transport elements are described in terms of a paraxial approximation as a solution of Eq. (1.11). A rigorous derivation of first and second order accelerator optics can be found in [24].

1.3.1 Solenoidal lens

In case of a pure axially-symmetric magnetic field the equation (1.9) is further reduced to:

$$r'' + k^2 r = 0, \tag{1.12}$$

where $k^2 \equiv (e\boldsymbol{B}/2mc\beta\gamma)^2$ or $\omega_L^2/(\beta^2 c^2)$, where ω_L is called Larmor frequency. Larmor frequency defines the rotation of the beam around its axis inside the solenoidal lens. The rotation stops upon exiting the solenoid field, therefore such a lens not just images the electron beam, but also rotates it. The angle of rotation can be computed as [17]:

$$\theta_{rot} = -\mu_0 eNI/2mc\beta\gamma, \tag{1.13}$$

where μ_0 is magnetic permeability, N is the number of coil turns, I is the current. The focal length f of the solenoidal lens can be calculated from [17]:

$$\frac{1}{f} = \frac{\theta_{rot} \sin \theta_{rot}}{l}, \tag{1.14}$$

where l is the total length of the solenoid with its fringe fields. The focusing provided by the solenoid is radial, so it affects the beam equally in all radial directions.

Due to the properties defined by Eqs (1.13) and (1.14), solenoidal lenses are commonly used in electron gun setups for initial optics matching out of the photocathode. Typically, three solenoids are used in the RF-gun setup. First two are called Bucking and Focusing, which are wired to have opposite direction of current to cancel out the magnetic field at the photocathode surface. When electrons exit the photocathode material, the residue field of the Focusing solenoid provides an inward force to reduce the beam's divergence and size. A

third solenoid, conventionally referred to as Main solenoid, provides additional flexibility in initial Twiss parameters mathching downstream of the RF-gun. Note, that it is sufficient to have just two solenoids in the RF-gun setup, however in practice three magnets provide better beam dynamics control.

Solenoidal lenses can be used further in the accelerator beamline as well as additional radial focusing elements. Such a beamline provides excellent beam matching capabilities and is commonly built for advanced phase-space manipulation purposes.

1.3.2 Drift element

In the external field-free region the particles in electron beam are subject to internal Coulomb fields and their motion can be described as

$$r'' - \frac{Kr}{a^2} = 0, \tag{1.15}$$

where a is the transverse size of the beam, $K = eI/2\pi\epsilon_0 mc^3\beta^3\gamma^3$ is the generalized perveance or *space-charge* parameter and I is the beam current. One can rewrite the space-charge parameter as:

$$K = \frac{2I}{I_0\beta^3\gamma^3}, \tag{1.16}$$

where $I_0 = e/2\pi\epsilon_0 mc^3 \approx 17$kA for electrons. One can also define a plasma frequency ω_p as $\omega_p = \beta c\sqrt{2K}/a$ and the radial motion of the electron will be described by $\ddot{r} = \omega_p^2 r/2$ [17]. If space-charge forces are neglected there $\ddot{r} = 0$ and $r' = r'(0)$ is a constant.

For sake of simplicity of the analysis space-charge parameter is often omitted, so the linearized axial motion of electrons can be represented in a matrix form as follows:

$$\boldsymbol{R}_d = \begin{pmatrix} 1 & L & 0 & 0 \\ 0 & 1 & 0 & 0 \\ 0 & 0 & 1 & L \\ 0 & 0 & 0 & 1 \end{pmatrix}, \tag{1.17}$$

where L is the length of the field-free region. Hereafter we will refer to Eq. (1.17) as *drift* element $\boldsymbol{R}_d$.

1.3.3 Dipole correctors

Dipole magnetic correctors are required to align the beam in the beamline. The dipole magnet effect can be characterized as a change of beam momentum in the transverse plane as $p_\perp(MeV/c) = 299.8B(T)R(m)$, where R is the bending radius. Dipole correctors are commonly arranged in pairs to account for vertical/horizontal kick, which can be summarized in the following form:

$$\begin{pmatrix} \delta p_x \\ \delta p_y \end{pmatrix} = \begin{pmatrix} d_x \\ d_y \end{pmatrix}. \tag{1.18}$$

Here (d_x, d_y) is a constant vector, where $d_{x,y}$ corresponds to the dipole kick value in x, y plane.

1.3.4 Quadrupole lens

Magnetic quadrupole lenses are commonly used for beam transport. The magnetic fields in the quadrupole are not axisymmetric, therefore its focusing properties are different in x and y directions. The electron motion in a quadrupole lens is convinient to describe using Eq. (1.11):

$$x'' + \frac{2e\beta cB_0}{\gamma md}x = 0, \qquad y'' - \frac{2e\beta cB_0}{\gamma md}y = 0, \tag{1.19}$$

where B_0 is the amplitude of the field and d is the lens aperture. The matrix solution of the Eq. (1.19) is also called *thick-lens* approximation and can be written as:

$$\boldsymbol{R}_q = \begin{pmatrix} \cos L\sqrt{\kappa} & 1/\sqrt{\kappa}\sin L\sqrt{\kappa} & 0 & 0 \\ -\sqrt{\kappa}\sin L\sqrt{\kappa} & \cos L\sqrt{\kappa} & 0 & 0 \\ 0 & 0 & \cosh L\sqrt{\kappa} & 1/\sqrt{\kappa}\sinh L\sqrt{\kappa} \\ 0 & 0 & \sqrt{\kappa}\sinh L\sqrt{\kappa} & \cosh L\sqrt{\kappa} \end{pmatrix}, \tag{1.20}$$

where κ is defined as $\kappa = 2eB_0/\gamma md\beta c$ and L is the length of the magnet. For convinience, one can also intoduce *thin-lens* approximation as (taking the limit $L\sqrt{\kappa} \ll 1$ and Taylor expand to the 1st order):

$$\boldsymbol{R}_q = \begin{pmatrix} 1 & 0 & 0 & 0 \\ q & 1 & 0 & 0 \\ 0 & 0 & 1 & 0 \\ 0 & 0 & -q & 1 \end{pmatrix}, \tag{1.21}$$

where $q = 1/f = \pm\kappa L$ is the focusing strength of the magnet and f is the focal length. The matrix of a skewed quadrupole can be obtained via transfomation in the form of $\boldsymbol{R}_{-\pi/2}\boldsymbol{R}_q\boldsymbol{R}_{\pi/2}$ Thin-lens approximation for a skewed quadrupole would then have form:

$$\boldsymbol{R}_q = \begin{pmatrix} 1 & 0 & 0 & 0 \\ 0 & 1 & q & 0 \\ 0 & 0 & 1 & 0 \\ q & 0 & 0 & 1 \end{pmatrix}. \tag{1.22}$$

For the IOTA/FAST quadrupole magnets the following relation is used to calculate it's current: $I_q = (1.8205K \times p\,[MeV/c])/405.4$, where $K = q/L_{eff}$ and $L_{eff} = 16.7cm$ is the effective length of the quadrupole. Focusing and defocusing quadrupoles are generally arranged in sections known as FODO cells.

1.3.5 Accelerating cavity in $TM_{010,\pi}$ mode

The oscillating EM-field in a periodic conducting structure can be tuned in a way that particles receive maximum energy gain upon arriving in a structure. Such structures are called accelerating cells and are commonly grouped together to form an accelerating multi-cell cavity. In this section we consider a standing-wave accelerating structure operating in the $TM_{010,\pi}$ mode. The transverse beam dynamics associated to such a cavity has been extensively explored over the last decade and focused essentially on numerical simulations of single-bunch emittance dilution due to the field asymmetries [25, 26, 27, 3] and multibunch effects due to trapped modes [28]. Most recently, experiments aimed at characterizing the transverse beam dynamics in this type of SRF cavity were performed [29, 30, 31].

1.3.5.1 Analytical model of the cavity

An analytical model of the $TM_{010,\pi}$ cavity was first derived by Chambers [32] and ammended by Serafini and Rosenzweig [33, 34]. Consider the transverse motion of the particle in a standing wave RF field with axial field $E_z(z,t) = E_0 \sum_n a_n \cos(nkz)\sin(\omega t + \phi)$, where E_0 is the peak field, nk is the wave number associated to n-th harmonic of amplitude a_n, ϕ is an arbitrary phase shift, and z is the longitudinal coordinate along the cavity axis.

The radial component of the Lorentz force given by Eq. (1.1) (or ponderomotive-focusing force) can be obtained under the paraxial approximation as

$$F_r = -e(E_r - vB_\theta) \approx er\frac{\partial E_z}{\partial z}, \tag{1.23}$$

where $v \simeq c$ is the particle velocity along the axial direction.

Ref. [33] shows that the force averaged over one RF-period in the first order of perturbation theory yields the focusing strength $\bar{K} = -(E_0 e)^2/8(\beta\gamma mc^2)^2$, for the case of a "pure" standing wave resonator (where the spatial profile of the axial field is modeled as $E_z(z) \propto \cos(kz)$ inside the cavity) originally considered in Ref. [32]. The equation of motion Eq. (1.9) in Cartesian coordinates then takes form:

$$x'' + \left(\frac{\gamma'}{\gamma}\right)x' + \bar{K}\left(\frac{\gamma'}{\gamma}\right)^2 x = 0, \tag{1.24}$$

where x is the transverse coordinate, $x' \equiv \frac{dx}{dz}$, $\gamma' \equiv \frac{d\gamma}{dz} = eE_0\cos(\phi)/m_0c^2 \equiv \bar{G}_{RF}/m_0c^2$ is the normalized energy gradient and γ is the Lorentz factor.

The solution of the Eq. 1.24 through the cavity can be linearized in the form of $\mathbf{x}_f = \boldsymbol{R}\mathbf{x}_i$, where $\mathbf{x} \equiv (x, x')^T$, here $\boldsymbol{R}$ is a 2×2 matrix, and the subscripts i and f indicate upstream and

downstream particle coordinates respectively. According to Chambers' model, the elements of $\boldsymbol{R}$ are given by [32, 33, 34, 35, 36]:

$$\begin{aligned} R_{11} &= \cos\alpha - \sqrt{2}\cos(\phi)\sin\alpha, \\ R_{12} &= \sqrt{8}\frac{\gamma_i}{\gamma'}\cos(\phi)\sin\alpha, \\ R_{21} &= -\frac{\gamma'}{\gamma_f}\left[\frac{\cos(\phi)}{\sqrt{2}} + \frac{1}{\sqrt{8}\cos(\phi)}\right]\sin\alpha, \\ R_{22} &= \frac{\gamma_i}{\gamma_f}[\cos\alpha + \sqrt{2}\cos(\phi)\sin\alpha], \end{aligned} \tag{1.25}$$

where $\alpha \equiv \frac{1}{\sqrt{8}\cos(\phi)}\ln\frac{\gamma_f}{\gamma_i}$, $\gamma_f \equiv \gamma_i + \gamma' L\cos\phi$ is the final Lorentz factor (where L is the cavity length). The determinant associated to the 2×2 block of the matrix is $|\boldsymbol{R}|_{2\times 2} = \gamma_i/\gamma_f$. The latter equation also holds for the vertical degree of freedom (y, y') owing to the assumed cylindrical symmetry. Under such an assumption the equations for the vertical degree of freedom are obtained via the substitutions $x \leftrightarrow y$, and indeces $1 \leftrightarrow 3$ and $2 \leftrightarrow 4$. The total transverse transfer matrix determinant is then $|\boldsymbol{R}|_{4\times 4} = (\gamma_i/\gamma_f)^2$.

The axially-symmetric electromagnetic field assumption invoked while deriving Eq. (1.25) is often violated, e.g., due to asymmetries introduced by the input-power (or forward-power) and high-order-mode (HOM) couplers. The input-power coupler provides the RF power to the cavity while the HOM couplers damp the harmful trapped fields potentially excited as long trains of bunches are accelerated in the SRF cavities. In addition to the introduced field asymmetry, the coupler can also impact the beam via geometrical wakefields [37, 38].

1.4 Canonical angular momentum (CAM) dominated beams

We now consider an electron source submerged in strong axial magnetic field and focus on electron beam transverse trace-space (x, x', y, y') dynamics. The latter case corresponds

to non-zero canonical angular momentum L defined by Eq. (1.3). Additionally, the relativistic Hamiltonian defined in Sec. 1.1 can be factored out into transverse and longitudinal components. The conservation of L yields that the mechanical angular momentum (MAM) of electron in the magnetic-field-free zone is:

$$|\boldsymbol{L}| = \gamma m |\boldsymbol{r} \times \frac{d\boldsymbol{r}}{dt}| = \frac{1}{2} e B_{0z} r_0^2, \tag{1.26}$$

where B_{0z} is the axial field at the emission point, r_0 is the electron coordinate at the emission point and r is the electron coordinate at the measurement location downstream of the cathode. The norm of $|\boldsymbol{L}|$ can be computed as $|\boldsymbol{L}| = |\boldsymbol{r} \times \boldsymbol{p}| = xp_y - yp_x$. In case of an axially symmetrical particle distribution, one can introduce $\langle L \rangle = eB_{0z}\sigma_0^2$ as a mean CAM averaged over the distribution, where σ_0^2 is the RMS size of the beam at the emission point. Also $\langle L \rangle = eB_{0z}\sigma_0^2 = const$ is a conserved quantity.

Following Ref. [39], we introduce the *magnetization* $\mathcal{L} \equiv \langle L \rangle / 2\gamma mc$. At the emission point the covariance matrix will take form:

$$\boldsymbol{\Sigma_{cyl}} = \begin{pmatrix} \sigma^2 & 0 & 0 & \mathcal{L} \\ 0 & \sigma'^2 & -\mathcal{L} & 0 \\ 0 & -\mathcal{L} & \sigma^2 & 0 \\ \mathcal{L} & 0 & 0 & \sigma'^2 \end{pmatrix}, \tag{1.27}$$

where σ and σ' are respectively the round-beam RMS size and divergence. Let's define an effective emittance as $\epsilon_{4D} \equiv \sqrt[1/4]{det\ \boldsymbol{\Sigma_{cyl}}} = \sqrt[1/4]{det\ \mathbf{J}\boldsymbol{\Sigma_{cyl}}} = \sqrt{(\sigma^2\sigma'^2 - \mathcal{L}^2)}$ and projected emittance as $\epsilon_0 \equiv \sigma\sigma'$, therefore $\epsilon_{4D}^2 = \epsilon_0^2 - \mathcal{L}^2$. Here $\mathbf{J}$ is a 4×4 skew symplectic unit matrix. It can be proved that the eigenvalues of $\boldsymbol{R}\boldsymbol{\Sigma_{cyl}}\tilde{\boldsymbol{R}}$ are conserved for any linear symplectic

transformation $\boldsymbol{R}$. The solution of the eigenvalue problem $det\,(\mathbf{J}\boldsymbol{\Sigma}_{\mathbf{cyl}} - \mathbf{I}\lambda) = 0$ yields two positive eigenemittances [11, 40, 19, 41, 42]:

$$\begin{aligned}\epsilon_- &\equiv \sqrt{\epsilon_0^2 + \mathcal{L}^2 - 2\mathcal{L}\epsilon} = \sqrt{(\epsilon_0 - \mathcal{L})^2} = \sqrt{\mathcal{L}^2 + \epsilon_{4D}^2} - \mathcal{L} \approx \frac{\epsilon_{4D}^2}{2\mathcal{L}} \\ \epsilon_+ &\equiv \sqrt{\epsilon_0^2 + \mathcal{L}^2 + 2\mathcal{L}\epsilon} = \sqrt{(\epsilon_0 + \mathcal{L})^2} = \sqrt{\mathcal{L}^2 + \epsilon_{4D}^2} + \mathcal{L} \approx 2\mathcal{L}. \end{aligned} \tag{1.28}$$

A beam is said to be *magnetized* when $\mathcal{L} \gg \epsilon_{4D}$. The eigenemittance ratio is often referred to as *flatness* and takes the form:

$$\frac{\epsilon_+}{\epsilon_-} = \frac{4\mathcal{L}^2}{\epsilon_u^2} = \frac{1}{p_z^2} e^2 B_{0z}^2 \frac{\sigma_0^2}{\sigma_0'^2}.$$

1.4.1 Round-to-flat beam transformation

The CAM can be removed from electron beam by propagating it through the series of three skewed quadrupoles such to apply a torque. Such a quadrupole channel is conventionally called Round-to-Flat Beam (RTFB) adapter or transformer. RTFB transformation projects eigenemittances onto conventional emittances, thereby creating a *flat* beam.

Let the RTFB transformer be described by a matrix product $\boldsymbol{R}_{RTFB} = \boldsymbol{R}_{q3}\boldsymbol{R}_{d3}\boldsymbol{R}_{q2}\boldsymbol{R}_{d2}\boldsymbol{R}_{q1}$, where $\boldsymbol{R}_{qi}, \boldsymbol{R}_{di}$ are the quadrupole (drift) matrices respectively. $\boldsymbol{R}'_{RTFB} = \boldsymbol{R}_{-\pi/2}\boldsymbol{R}_{RTFB}\boldsymbol{R}_{\pi/2}$, where $\boldsymbol{R}_\phi$ is the rotation matrix. The beam second order moment matrix $\boldsymbol{\Sigma}_0 = \begin{pmatrix} \Sigma_{XX} & \Sigma_{XY} \\ \Sigma_{YX} & \Sigma_{YY} \end{pmatrix}$ is transformed as $\boldsymbol{\Sigma}_f = \boldsymbol{R}_{RTFB}\boldsymbol{\Sigma}_0\tilde{\boldsymbol{R}}_{RTFB}$, where $\Sigma_{\{X,Y\},\{X,Y\}}$ are 2×2 blocks of $\boldsymbol{\Sigma}$ matrix, $\boldsymbol{\Sigma}_0$ is the beam matrix at the entrance of the RTFB transformer, $\boldsymbol{\Sigma}_f$ is the beam matrix at the

exit of the transformer. RTFB transformer transfer matrix can be rewritten in block form as $\boldsymbol{R}_{RTFB} = \begin{pmatrix} A & B \\ C & D \end{pmatrix}$ and the condition to remove CAM $\Sigma_{fXY} = 0$ yields [43]:

$$A\Sigma_0\tilde{B} + B\Sigma_0\tilde{A} + A\Sigma_C\tilde{A} + B\tilde{\Sigma}_C\tilde{B} = 0. \tag{1.29}$$

The latter matrix equation can be solved analytically in case of cylindrically symmetric distribution with a beam waist located at the entrance of the RTFB transformer and yields two sets of solutions for quadrupole strength $q = 1/f$, where f is focal length; see also Ref. [44]:

$$\begin{aligned} q_1 &= \pm\sqrt{\frac{-d_2(d_T s_{21} + s_{11}) + d_T s_{22} + s_{12}}{d_2 d_T s_{12}}}, \\ q_2 &= \frac{(d_2 + d_3)(q_1 - s_{21}) - s_{11}}{d_3(d_2 q_1 s_{11} - 1)}, \\ q_3 &= \frac{d_2(q_2 - q_1 q_2 s_{12}) - s_{22}}{d_2(d_3 q_2 s_{22} + q_1 s_{12} - 1) + d_3(s_{12}(q_1 + q_2) - 1)}, \end{aligned} \tag{1.30}$$

where q_i is the quadrupole strength, d_2, d_3 are the distances between first and second, and second and third quadrupole respectively, s_{ij} are the elements of 2×2 symplectic matrix $\boldsymbol{S}$. Matrix $\boldsymbol{S}$ can be defined as a correlation matrix $\boldsymbol{Y} = \boldsymbol{S}\boldsymbol{X}$, where $\boldsymbol{X}, \boldsymbol{Y}$ are the trace space vectors, or as in [39]:

$$\boldsymbol{S} = \pm\frac{1}{\epsilon_0}\begin{pmatrix} \Sigma_{12} & -\Sigma_{11} \\ \Sigma_{22} & -\Sigma_{12} \end{pmatrix}, \tag{1.31}$$

where $\epsilon_0 = \sqrt{\epsilon_{4D}^2 + \mathcal{L}^2}$. Additionally, it should be noted that the solution provided by Eqs. (1.30) does not depend on the value of $\mathcal{L}$.

The sign of q_1 in Eq. (1.30) determines the eigenemittance projection orientation. Positive sign $+q_1$ corresponds to the mapping $(\epsilon_- \to \epsilon_x, \epsilon_+ \to \epsilon_y)$, thereby representing a *vertical flat beam* solution. Negative sign $-q_1$ corresponds to $(\epsilon_- \to \epsilon_y, \epsilon_+ \to \epsilon_x)$ which generates a *horizontal flat beam* solution.

In case of a most general form of Eq. (1.6) with all couplings, the Eq. (1.29) yields a coupled system of degree 6 polynomials and the solution can only be computed numerically. In case of a general magnetized distribution, RTFB settings should be calculated for each value of $\mathcal{L}$. Note, that Eqs. (1.30) are derived in thin-lens approximation and the actual settings for the RTFB transformer should be reoptimized. It can be done with a particle tracking program ELEGANT [23] or with a MAGNETOPTIMIZER toolbox written by the author [45]. ELEGANT has higher-order corrections implemented for the accelerator elements and uses simplex optimization for solving Eq. (1.29).

Previously, experimental generation of CAM and flat beams was demonstrated at Fermilab's A0 facility and an emittance ratio of 100 was achieved at the beam energy of 15 MeV and bunch charge of 0.5 nC [46, 44, 12, 47].

1.5 Magnetic bunch compressor (chicane)

A magnetic bunch compressor (or a chicane) is comprised of four dipole magnets to utilize energy dependent path lengths in order to change total bunch length. The chicane is usually designed to be achromatic in the bending plane. Lower energy particles will be bent more, therefore will be travelling a longer path rather than higher energy particles. Using this correlation it is possible to compress and decompress the electron bunch; see Fig. 1.2. When the initial energy correlation is such that lower energy particles are placed in the bunch head and higher energy particles are in the bunch tail, the chicane will perform

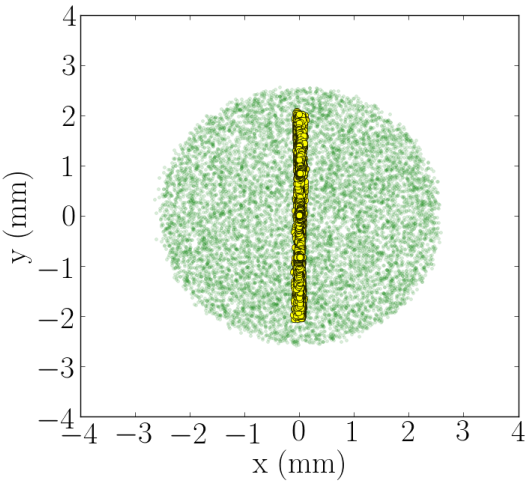

Figure 1.1: Demonstration of CAM removal in ELEGANT simulations for the case of ϵ_{4D} = 2 μm and ϵ_+/ϵ_- = 400. Original magnetized round beam (green) was shaped into flat beam (yellow).

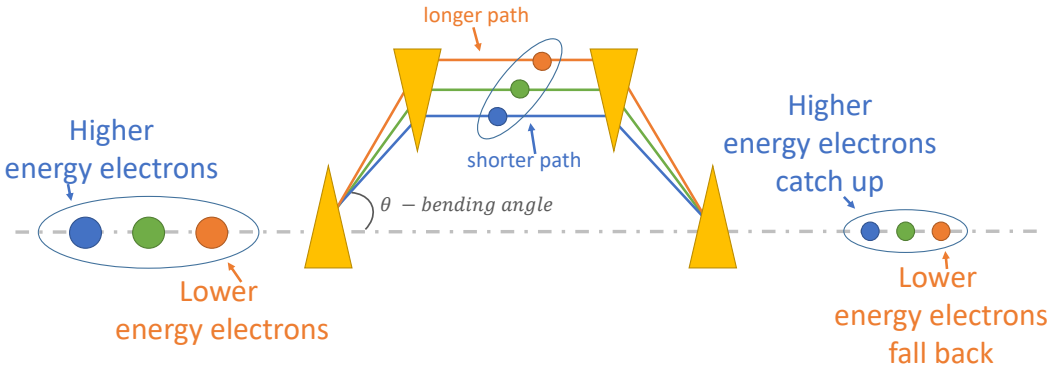

Figure 1.2: Compression of the electron beam in the magnetic chicane. Energy correlation imposed on the beam results in different path lengths and compression in longitudinal direction. Yellow wedges represent four identical dipole magnets with the bending angle θ.

a bunch compression, and in the opposite case - decompression. The transformation of the longitudinal trace-space (z, δ) in the chicane is described by:

$$\boldsymbol{R}_{BC} = \begin{pmatrix} 1 & R_{56} \\ 0 & 1 \end{pmatrix}, \tag{1.32}$$

where R_{56} is referred to as a longitudinal dispersion. The i-th particle longitudinal coordinate is then transformed as:

$$z_f = z_i + R_{56}\delta_i, \tag{1.33}$$

where $\delta_i = \Delta p_i / p_0$, p_0 is the bunch center of mass and $\delta_f = \delta_i$. The final RMS bunch length is then transformed as:

$$\sigma_{z_f} = \sqrt{\sigma_{z_i}^2 + R_{56}\langle z_i \delta_i \rangle + R_{56}^2 \sigma_{\delta_i}^2}. \tag{1.34}$$

One can define longitudinal phase-space (LPS) chirp as $C \equiv \langle z_i \delta_i \rangle / \sigma_{z_i}^2$. The case of chirp $C = -1/R_{56}$ corresponds to the maximum longitudinal compression. In practice, the chirp is imposed on the electron beam via off-crest acceleration in the cavities. In the FAST beamline the chicane dipoles have a bending angle of θ = 18 degrees yielding R_{56} = -0.18 m. In our convention, $R_{56} < 0$ provides compression when the tail ($z < 0$) of the bunch has a higher energy than its head.

CHAPTER 2

EXPERIMENTAL FACILITIES

In this Chapter we will describe the photoinjector facilities utilized to perform dissertation research. Most of the work reported in the thesis was done at FAST facility. Additionally, several experiments with transverse electron bunch shaping were conducted at the Argonne Wakefield Accelerator (AWA). Both facilities share similar injector design concepts, with FAST relying on SRF- and AWA on normal conducting acceleration. The main purpose of FAST injector is two-fold: provide electron beam to IOTA ring and deliver low- and high-energy electrons to the experimental areas. AWA facility is mostly dedicated to the wakefield driven acceleration and transverse-to-longitudinal emittance exchange experiments.

2.1 Fermilab Accelerator Science and Technology (FAST) facility

Fermilab Accelerator Science and Technology (FAST) facility includes a high-brightness and high repetition rate electron injector and the Integrable Optics Test Accelerator (IOTA) electron ring. The injector beamline comprises of low- and high-energy sections, which accelerate electrons up to maximum of 301 MeV. For the IOTA ring operations the linac will supply 150 MeV electrons to the insertion point. IOTA/FAST facility beamline is diagrammed on Fig. 2.1. The electron source is a high quantum efficiency Cs_2:Te photocathode placed in a L-band $1 + \frac{1}{2}$ cavity RF gun. The photocathode is impinged on by a 263 nm wavelength UV laser directed on the emitting surface at 45 degrees. The photocathode diameter is 8 mm with 5 mm photosensitive area. The laser is driven by a Yb-doped Calmar

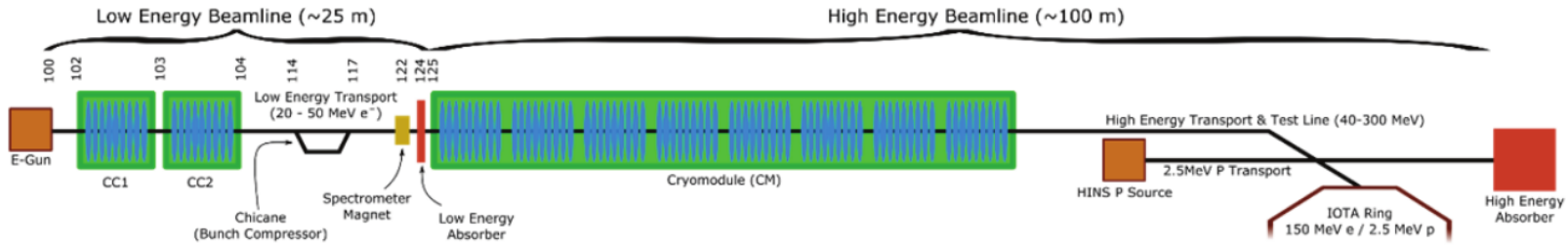

Figure 2.1: IOTA/FAST beamline schematics. Photoelectrons are born and initially are accelerated in a normal conducting L-band RF gun, then further boosted up to 52 MeV in two L-band SRF booster cavities. The electron beam is then matched in the quadrupole channel into the ILC-type cryomodule that gives the beam its final energy of 301 MeV. For IOTA operations the cryomodule is operated at a lower gradient to obtain 150-MeV electrons. Both low and high energy beamlines have experimental areas located near low- and high-energy adsorbers. Key beamline elements positions are provided in Tab. 2.2. Figure is the courtesy of FAST collaboration.

seed fiber laser which has frequency of 81.25 MHz. Pockels cells are used to form pulse trains (up to 1 ms long with pulse repeated at 3 MHz) that are further amplified in a chain of YLF crystal-based amplifiers ($\lambda = 1.064\mu$m). Finally, two frequency-doubling crystals are installed in the light path to achieve the required UV wavelength.

The gun is surrounded by a bucking and main solenoids, set up in a way that they nominally yield a vanishing magnetic field B_{0z} at the photocathode surface. The maximum peak field of each solenoid is 0.28 Tesla (for an excitation current of 500 A). The solenoids can be tuned to provide a non-vanishing axial magnetic field B_{0z} at the cathode and generate CAM beams. Table 2.1 provides nominal electron beam and machine operational parameters. For a detailed description of the facility, please see Refs. [48, 49, 50, 7].

Table 2.1: Low-energy beamline parameters of the IOTA/FAST injector.

Parameter	**Value**	**Units**
Transverse emittance (norm.)	<1	μm
Beam energy	50	MeV
Slice energy spread	<5	keV
Nominal charge	250	pC
Minimum charge	10	fC
Maximum charge	3.2	nC
Bunch length	5	ps
Beta-function (CC2 exit)	8	m
Chicane slit mask width, w	50	μm
Energy chirp, C	-5.56	m^{-1}
Chicane dispersion, η	-0.3	m
Longitudinal dispersion, R_{56}	-0.18	m

2.1.1 Low-energy beamline

An initially photoemitted electron beam is accelerated to ~ 5 MeV in the RF gun and subsequently boosted in two 1.03 m long 1.3-GHz SRF accelerating Nb cavities [labeled as CC1 and CC2 in Fig. 2.1] up to maximum of ~ 52 MeV. Each cavity is cooled to ~2 K with liquid He with an independent cryostat. The total length of the low energy beamline is

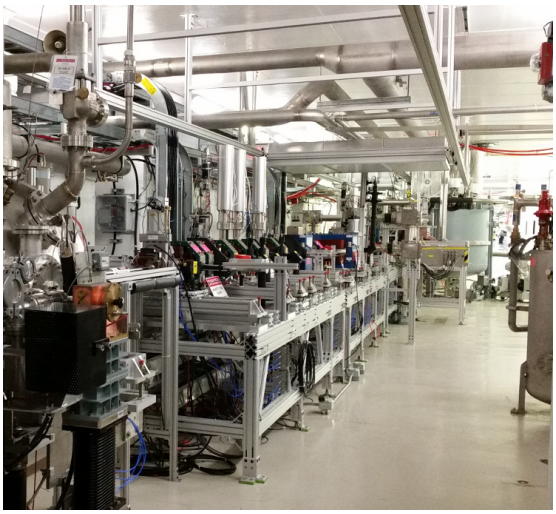

Figure 2.2: Overview of the FAST low-energy beamline during 2017 comissioning run.

about 25 m; see Fig. 2.2. The RF gun solenoids and the cavities provide initial focusing of the beam and set the Twiss parameters before entering the quadrupole channel. The beam is then matched in the series of FODO sections to the desired values of Twiss parameters at the entrance of the cryomodule. Electron bunch can be additionally compressed in the magnetic chicane.

The FAST injector optics can be matched and loaded in the machine on-the-fly via recently developed control tools [51]. The low-energy beamline has a number of vertical and horizontal multislit diagnostic stations located up-/downstream of the bunch compressor (at X107 and X118 locations), that allow measurement of the beam emittance in both transverse

Table 2.2: FAST low-energy beamline key components and their locations. The skew-quadrupole names are denoted in italic font.

Quadrupoles	Position (m)	**YAG screens**	Position (m)
Q106	8.682	X107	8.905
Q107	8.883	X111	10.540
Q108	9.491	X121	17.420
Q109	9.873	**Cavities**	-
Q110	10.255	CC1	4.030
Q111	10.459	CC2	5.500
Q112	11.004	**Slits**	-
Q113	11.205	X107	8.905
Q120	16.285	X118	15.900

planes [52]. The injector also contains multiple YAG:Ce (cerium-doped yttrium aluminum garnet) scintillating viewers, which are used to measure the beam transverse density. An additional multislit mask is installed inside the magnetic chicane to allow formation of microbunched beams for future radiation-generation experiments.

The beamline also contains beam position monitors (BPMs), resistive wall current monitors and loss monitors to measure the beam centroid positon, its current and the losses respectively. Each BPM consists of four electromagnetic pickup "button" antennae located 90° apart at the same axial position and at a radial position 35-mm from the beamline axis. The beam position $u = (x, y)$ is inferred from the beam-induced voltage on the antenna using a 7-th order polynomial $u = \sum_i a_{u,i} F(\Phi_j)$ where Φ_j $(j = 1, 2, 3, 4)$ are the induced voltages on each of the four BPM antenna and the coefficients $a_{u,i}$ are inferred from a lab-bench calibration procedure using a wire-measurement technique; see Ref. [53]. The low energy beamline contains its own spectrometer dipole magnet that directs beam into the low-energy adsorber.

2.1.1.1 Accelerating cavity design and simulations

FAST electron injector booster cavity was originally designed as a part of TESLA project [1]. In order to understand the operation of the cavity, a 3D electromagnetic model, including auxiliary couplers, was implemented in HFSS [54]. The simulated 3D electromagnetic field map was imported as an external field in the ASTRA particle-tracking program [21]. The program ASTRA tracked particles in the presence of external field from first principle via a time-integration of the Lorentz equation. Additionally, ASTRA can include space-charge effects using a quasistatic particle-in-cell approach based on solving Poisson's equation in the bunch's rest frame [21]. The electromagnetic field map $\{\boldsymbol{E}(x,y,z),\boldsymbol{B}(x,y,z)\}$ in HFSS was generated over a rectangular computational domain with $x,y\in[-10,+10]$ mm from the cavity axis and for $z\in[-697.5,+697.5]$ mm with respect to the cavity center along the cavity length; see Fig. 2.3(a).

The mesh sizes in the corresponding directions were respectively taken to be $\delta x=\delta y=$ 0.5 mm and $\delta z=1$ mm. Electromagnetic simulations assume a loaded quality factor $Q\simeq 3\times10^6$ as needed for the nominal ILC operation. Such a loaded Q corresponds to the inner conductor of the input-coupler having a 6-mm penetration depth [55]. Figures 2.3(b) and (c) respectively present the axial and transverse fields simulated along the cavity axis and normalized to the peak axial field $E_0\equiv\max[E_z(r=0,z)]$. As can be seen in Fig. 2.3(c) the impact of the coupler, aside from shifting the center of the mode, also introduces *time-dependent* transverse electromagnetic fields that will impact the beam dynamics. Given the field map loaded in ASTRA, the program introduces the time dependence while computing the external Lorentz force experienced by a macroparticle at position $\boldsymbol{r}\equiv(x,y,z)$ at a given time t as in (1.1). In the latter equation the time origin is arbitrarily selected to ensure $\phi=0$ corresponds to on-crest acceleration.

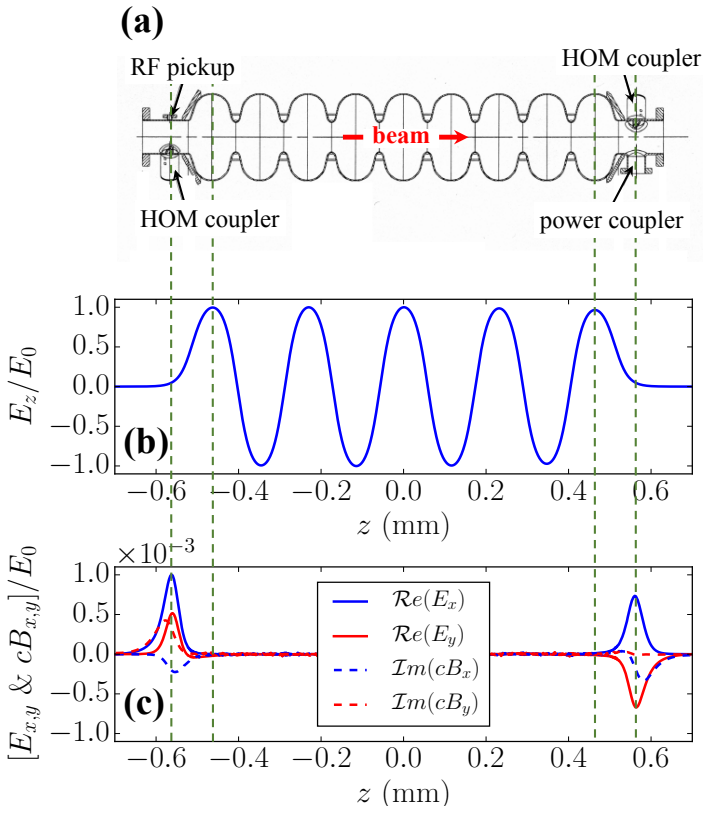

Figure 2.3: Schematics of the booster cavity considered in the present study (a) along with the axial $E_z \equiv E_z(r = 0, z)$ (b) and transverse (c) electromagnetic fields simulated on the cavity geometric axis $r = 0$. In (b) and (c) the fields are saved at a time where the electric E_x, E_y, and E_z are real while the magnetic cB_x and cB_y fields are imaginary. All the fields are normalized to the maximum axial electric field E_0.

In order to deconvolve the impact of the auxiliary couplers from the dominant ponderomotive focusing of the cavity, numerical simulations based on a cylindrical-symmetric model were also performed. For these calculations the axial electric field $E_z(r = 0, z)$ displayed in Fig. 2.3(b) is imported in ASTRA where the corresponding transverse electromagnetic fields at given positions (r, θ, z) are computed assuming an ideal TM_{010} mode and under the paraxial approximation as $E_r = -\frac{r}{2}\frac{\partial E_z(r=0,z)}{\partial z}$ and $B_\phi = \frac{i\omega r}{2c^2}E_z(r = 0, z)$ [56]. The simulations and measurements generally indicate that higher spatial harmonics do not play a significant role for the case of the FAST cavity.

2.1.2 High-energy beamline

High-energy beamline starts with a cryomodule that consists of 8 9-cell 1.3 GHz SRF cavities that boost the beam up to 301 MeV; see Fig. 2.4. Each cavity has been previously conditioned to operate at up to 31.5 MeV/cavity energy gradient. The RF power to the cryomodule is supplied by a single 5 MW klystron. The operating temperature is 2 K and the detailed description of the ILC-type cryomodule cryogenics design is provided by Ref. [57]. The accelerated electron beam is matched with high-energy quadrupoles and can be either

Figure 2.4: FAST ILC-type cryomodule capable of boosting electron beam up to 301 MeV. Image is a courtesy of FAST facility.

injected into the IOTA ring or directed to a high-energy experimental area. The high-energy beamline also has several YAG stations to register beam transverse density distribution. In the future, the installation of additional cryomodules from the original design [49] is foreseen.

2.2 Argonne Wakefield Accelerator (AWA) facility

The Argonne Wakefield Accelerator (AWA) facility is an electron facility dedicated mostly to the wakefield acceleration and emittance exchange experiments. It comprises of two beamlines labeled as AWA drive beamline (AWA-DB) and AWA witness beamline (AWA-

WB) respectively. For a detailed description of the facility, the reader is referred to Ref. [58, 59].

2.2.1 Drive beamline

The electron source of the AWA-DB is a high quantum efficiency Cs_2:Te photocathode placed in a $1+\frac{1}{2}$ cell L-band (1.3-GHz) RF gun. The RF gun is capable to produce 5-8 MeV electron bunches according to the experimental needs. Cathode is impinged by a 248 nm UV 2 ps laser pulses. The maximum laser pulse is 20 mJ which can emit up to 100 nC bunches. The UV laser production is performed similarly to FAST facility with a frequency tripler.

The RF-gun setup contains three solenoinds: bucking, focusing and main. Bucking and focusing solenoids have the opposite polarity and minimize the axial magnetic field at the cathode, while main solenoid is used to perform initial optics matching. Gun solenoids can be alternatively configured to generated maximum of 0.1 Tesla at the photocathode plate.

After photoemission electron bunches are then further accelerated in an L-band 10 cell normal conducting cavities operating in $TM_{010,\pi/2}$ mode up to 75 MeV; see Fig. 2.6. For additional optics matching, several solenoids are installed in the beamline (referred as linac solenoids); see Fig. 2.5 Several YAG:Ce scintillating screens (YAG in Fig. 2.5) are available to measure the beam transverse density along the accelerator and emittance exchange beamline.

2.2.2 Witness beamline

The AWA "witness-beam" (AWA-WB) beamline is diagrammed in Fig. 2.7. In brief, AWA-WB accelerator incorporates an L-band $1+\frac{1}{2}$ RF gun with a Mg photocathode on its back plate that is capable of producing up to 1 nC bunches. The gun is surrounded

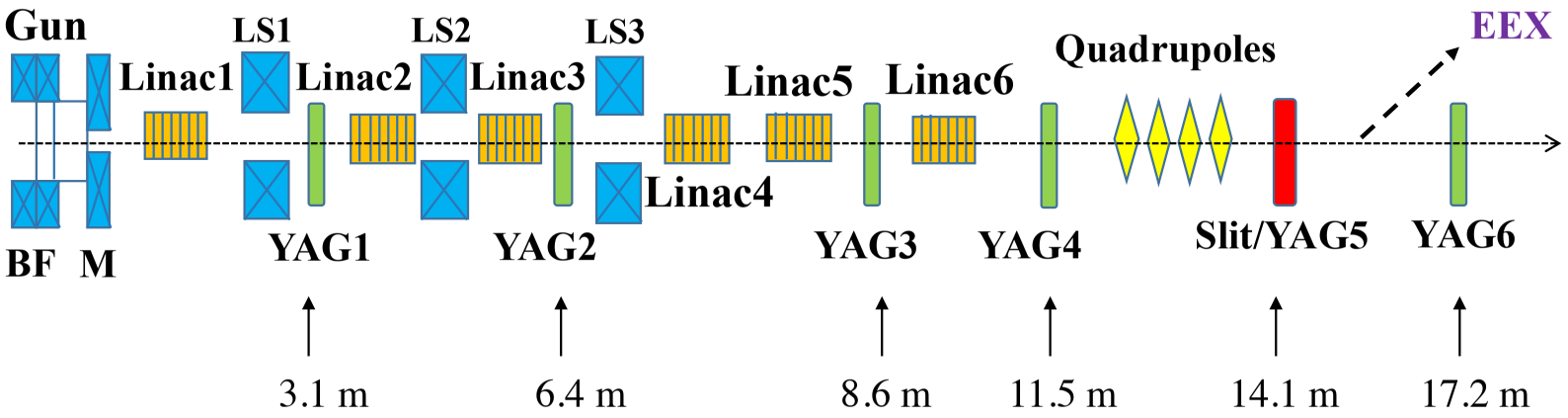

Figure 2.5: Overview of the AWA-DB beamline only showing elements relevant to the performed experiments. Bucking-focusing (BF) and matching (M) solenoids were adjusted to image the beam at the required location in the beamline. Linac solenoids (LS) and quadrupoles were used during the experiment for additional beam matching. The positions of the YAG viewers are denoted in meters. The energy gain of one accelerating cavity (linac) is 10 MeV. EEX label marks the separate double-dogleg beamline for transverse-to-longitudinal emittance exchange experiments. Figure is the courtesy of AWA group.

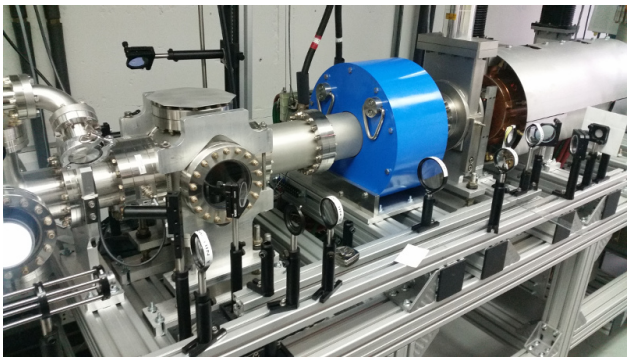

Figure 2.6: AWA-DB low-energy area. Linac 1 is followed by the linac solenoid and vacuum laser injection port.

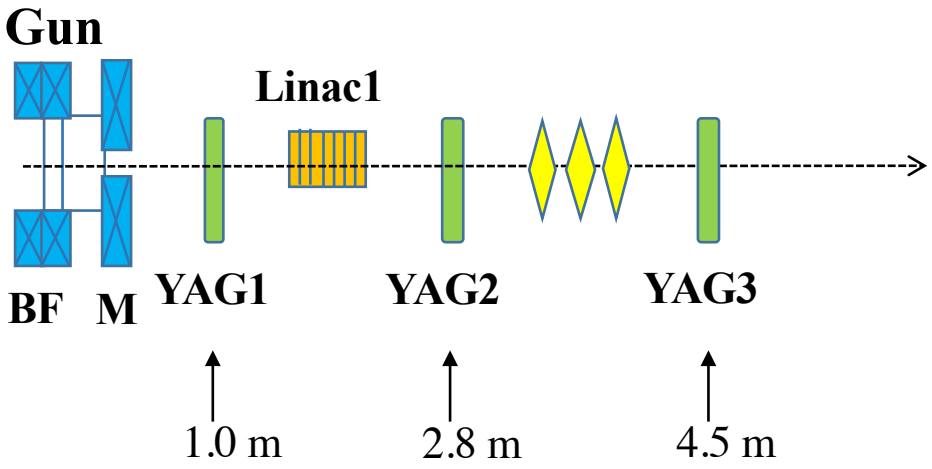

Figure 2.7: Overview of the AWA-WB beamline. The bucking (B) and focusing (F) solenoidal lenses can be setup to produce CAM-dominated beams. The positions of the YAG viewers are denoted in meters. Figure is the courtesy of AWA group.

by a bucking and focusing solenoids, nominally powered to yield a vanishing magnetic field B_{0z} at the photocathode surface. The solenoids can be tuned and provide a non-vanishing axial magnetic field B_{0z} at the cathode, similarly to AWA-DB electron gun. Nominally, the bucking and focusing solenoids have the opposite polarity, however they can be operated with the same polarity and provide significant field ($B_{0z} \sim 0.1$ T) on the photocathode. Photoelectrons are accelerated up to 8 MeV out of the RF gun and further boosted up to 18 MeV in an L-band linac; see Fig. 2.7.

CHAPTER 3

MICROLENS ARRAY (MLA) LASER TRANSVERSE SHAPING

In this Chapter we present a simple technique capable of controlling the transverse shape of a UV laser pulse. The technique employs microlens arrays (MLAs) to directly homogenize the UV laser pulse. MLAs are commonly employed as optical homogenizers for various applications [60, 61]. In addition to its homogenizing capability, we also demonstrate that the MLA-based technique can also produce a periodic transverse pattern that can form a two-dimensional array of beamlets (multi-beams). Such type of beams could find application in beam-based diagnostics of accelerator, single-shot quantum-efficiency map measurement, and coherent light sources in the THz regime or at shorter wavelength [62, 63].

3.1 Optical performances of the MLA

Qualitatively, the principle of the MLA lies in redistributing the incoming light intensity across the light beam spot. Typically, MLAs are arranged in pairs. After passing through the MLA assembly, the light rays are collected by a convex lens which focuses parallel rays from different light beamlets to a single point at the image plane. Under proper conditions (distance to the lens and its focal length), the process leads to transverse homogenizing of the beam; see Fig. 3.1. Therefore the MLA homogenization scheme is rather simple and appealing in the context of photocathode drive lasers. Alternatively, imaging the object

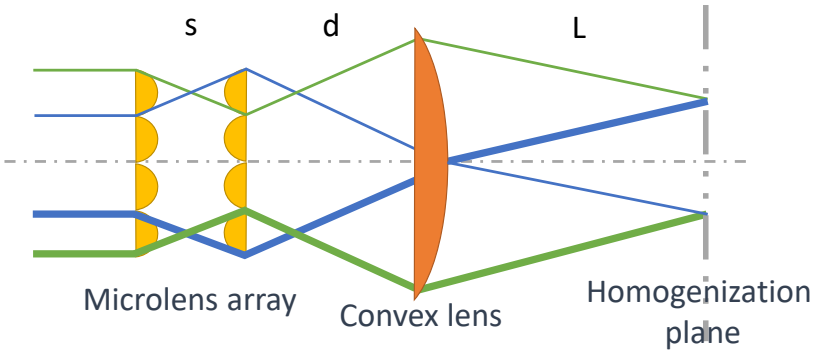

Figure 3.1: Schematics of the microlens array configuration. Initial intensity fluctuations in the beam (thin/thick ray) become evenly distributed at the homogenization plane.

plane of the single microlenses in the MLA with a convex lens produces a set of optical beamlets arranged as arrays (with a pattern mimicking the microlens spatial distributions).

The typical MLA setup is diagrammed in Fig. 3.1. To derive a few salient features relevant to the laser beam homogenization we will use ABCD formalism [60]. Consider an initial light ray to be characterized by the vector (x_0, x_0'), where x_0 and $x_0' \equiv \frac{dx_0}{dz}$ are respectively the initial ray position and divergence (here, z represents the path-length along the optical transport). As a simple example, we consider a rectangular array of microlens in the (x, y) plane with an equal pitch in both transverse directions. Using the ABCD formalism, and considering that the ray is within the aperture ρ of the lens with center located at $(x = mp, y = np)$, we can describe the MLA with the linear transformation

$$\begin{pmatrix} x_1 - mp \\ x_1' \end{pmatrix} = \begin{pmatrix} 1 & 0 \\ -1/f_2 & 1 \end{pmatrix} \begin{pmatrix} 1 & s \\ 0 & 1 \end{pmatrix} \times \times \begin{pmatrix} 1 & 0 \\ -1/f_1 & 1 \end{pmatrix} \begin{pmatrix} x_0 - mp \\ x_0' \end{pmatrix}, \tag{3.1}$$

where (x_1, x_1') is the ray vector after two MLA plates, s is the spacing between two plates, p is the array pitch, f_1 and f_2 are the focal lengths of the first and second microlens respectively. It should be pointed out that the ray initial and final coordinates satisfy $\sqrt{(x_0 - mp)^2 + (y_0 - np)^2} \leq \rho$ where n and m are integers that specify the position of each micro-lens in terms of the pitch. Then, the output ray from the MLA setup can be further propagated up to the homogenization plane as

$$\begin{pmatrix} x_h \\ x_h' \end{pmatrix} = \begin{pmatrix} 1 & L \\ 0 & 1 \end{pmatrix} \begin{pmatrix} 1 & 0 \\ -1/F & 1 \end{pmatrix} \begin{pmatrix} 1 & d \\ 0 & 1 \end{pmatrix} \begin{pmatrix} x_1 \\ x_1' \end{pmatrix}, \tag{3.2}$$

where (x_h, x_h') is the ray vector at the homogenization plane, d the distance between the convex lens and the MLA, F the focal length of the lens and L is the distance to the homogenization plane.

From the formalism above one can deduce a few useful expressions. First, we consider the case when the two MLAs are identical ($f_1 = f_2 = f$) and located in the object plane of the convex lens ($L = F$). We further assume that there is no cross-talk between the microlens and their transformation only affects rays within a finite aperture smaller than the array pitch $\sqrt{(x_0 - mp)^2 + (y_0 - np)^2} \leq p/2$. Under these assumptions, we find the diameter of the image at the homogenization plane to be

$$D_h \approx \frac{Fp}{f^2}(2f - s) \tag{3.3}$$

in the limit of small ray divergence (as indicated by the independence of the equation on d). For practical purposes, we also calculate the diameter of the beam at the convex lens plane to be

$$A_F \approx \frac{dp}{f^2}(2f - s). \tag{3.4}$$

This equation is useful to estimate the required aperture.

In practice, the assumption $L = F$ might be challenging to satisfy. In such cases, the following expression is useful to find the beam size at a given location L with respect to the convex lens:

$$D(L) \approx \frac{pL}{f^2}(2f - s) + \frac{dp(2f - s)}{f^2}\frac{F - L}{F}. \tag{3.5}$$

If $L \approx F$ the resulting image remains homogenized due to the finite size of the Airy disk. Moving away from the focal plane increases the density modulations and eventually yield an array of beamlets.

3.1.1 Optical transport design

Photoinjector setups often incorporate relatively long (multi-meter scales) optical transport lines. The optical lines include transport from the laser room to the photoinjector enclosure (generally performed in the air or in moderate vacuum pipe) and the injection in the ultra-high-vacuum accelerator beamline up to the photocathode. Consequently, it is necessary to devise an optical transport line capable of imaging the homogenized laser profile on the photocathode surface. A commonly-used imaging setup, known as $4f$-imaging, is challenging to implement in the present case as it would require some of the lenses to be located in the vacuum chamber, as the "imaging" plane has to be much farther downstream than the "object" plane upstream. However, imaging can be achieved in numerous ways while accommodating the various constraints related to MLAs (limited apertures, available focal lengths, etc...). To construct the appropriate optical line we impose the vector of a

ray in the homogenization plane (x_h, x'_h) to be transported to a downstream imaging plane (x_I, x'_I) via

$$\begin{pmatrix} x_I \\ x'_I \end{pmatrix} = \mathbf{M} \begin{pmatrix} x_h \\ x'_h \end{pmatrix}, \quad \text{with} \quad \mathbf{M} = \begin{pmatrix} \mathcal{M} & 0 \\ 0 & 1/\mathcal{M} \end{pmatrix},$$

where the magnification $\mathcal{M}$ is set to 1 for one-to-one imaging. The latter linear system yields four equations; an additional constraint comes from the total length of the imaging transport. Therefore, the problem has 5 unknowns in total with some flexibility within available lenses. Hence, it is possible to construct four-lens solution with distances between lenses as free parameters to make the corresponding system of linear equations well-defined.

The simulation of such a four-lens system was accomplished with a simple ray-tracing program where an initial set of optical rays was distributed according to a two-dimensional Gaussian distribution in the (x, x') optical trace space. The optical layout of the laser transport downstream of the MLA is depicted in Fig. 3.2(a): it includes four cylindrical-symmetric lenses, an optical window that allows for the laser beam to be injected in an ultra-high-vacuum area and an in-vacuum metallic mirror that direct the laser beam on the cathode surface. The resulting evolution of the beam size along the transport downstream of the MLA and up to the photocathode is display in Fig. 3.2(a,b) for the two RF-gun configurations available at the AWA facility. For both setups, the large beam size produced at the location of the last optical lens demands a large-aperture lens. The beam size downstream of it gradually decreases until it reaches its target transverse size on the photocathode surface (8 mm rms). The in-vacuum mirror located close to the last optical transport lens can be another limiting aperture of the optical system and generally results in beam losses. For the two cases reported in Fig. 3.2 (a) and (b) the MLA-to-cathode transmission due to the finite geometric aperture, window transmission coefficient, losses in the lenses and mirrors was computed to be 57% and 43%.

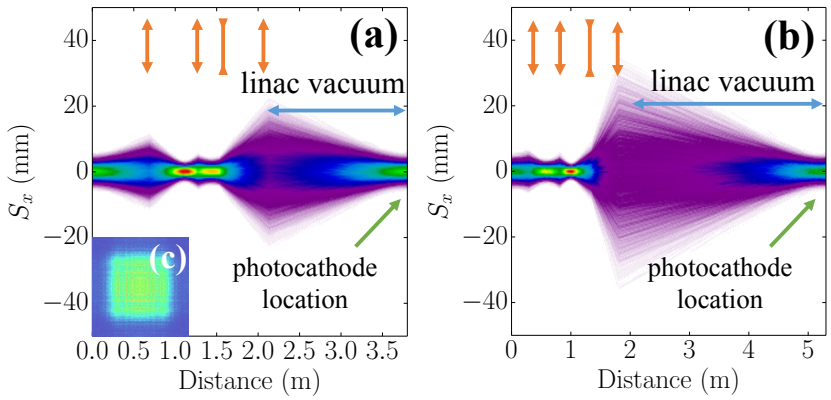

Figure 3.2: False color ray-tracing distribution of a four-lens optical line capable of imaging the homogenized beam on the photocathode surface. The configuration in (a) and (b) correspond respectively to the AWA witness-beam and drive-beam electron-source setups. The lenses type and locations are shown as red arrows. The inset (c) gives the intensity distribution simulated using the ectorial-diffraction program SRW for a 5×5 rectangular MLA.

The designs presented in the Fig. 3.2 were also simulated with the SYNCHROTRON RADIATION WORKSHOP (SRW) software [64] which is based on Fourier optics and readily include a wave-propagation treatment of the laser transport; see Fig. 3.2 (c) inset. It confirmed that diffraction effects in the setup are negligible compared to transmission losses in the optical system. In the future, the established numerical model of the MLA will be used for customizing the micro-lens profiles, arrangement, and pitch. It should be noted that linearized ABCD approach is sufficient to set up MLA system and full wave propagation simulations may be omitted in the beginning.

Finally, transverse instabilities coming from shot-to-shot jitter in the transverse distribution displayed in Fig. 3.3 (left), would result in charge fluctuations if the laser beam is collimated by an iris upstream of the MLA. To improve the stability of the laser intensity we introduced a two-lens beam reducer in front of the MLA.

3.1.2 Optical measurements

To evaluate the performance of the proposed scheme, we use two MLA's on the photocathode drive laser of the AWA [59]. The input UV (λ = 248 nm) laser pulse is obtained from frequency tripling of an amplified IR pulse originating from a Titanium-Sapphire (Ti:Sp) laser system. Downstream of the frequency tripler the UV pulse is further amplified in a two-pass excimer amplifier before transport to the accelerator vault. The setup shown in Fig. 3.1 was followed by the optical transport line shown in Fig. 3.2. A calibrated UV-sensitive screen with associated CCD camera mounted downstream of the setup directly provided a measurement of the transverse distribution achieved on the photocathode surface.

To gain confidence in the performance of the MLA setup, we first investigated the impact of a non-perfectly collimated incoming laser beam. As it can be inferred from Fig. 3.1, the homogenization can still be achieved even if the incoming beam has a small divergence. There is a critical value of beam divergence $\tan\theta = p/2f$ that causes destructive interference after the MLA and results in light loss [65].

The beam size provided by Eq. 3.3 was used in the optical relay setup and Eq. 3.4 justified the aperture value of the convex lens. Overall, we have observed a good agreement with Eq. 3.3 and Eq. 3.4. The calculated laser beam size was within the aperture of all optical elements and latter was confirmed experimentally.

Note, that the convex lens in the experimental setup should be placed at the distance $D > F$ from the array, where F is the focal length of the convex lens.

The setup was also employed to demonstrate the homogenization process and quantify its performances. The nominal UV laser pulse was used as a starting condition; see Fig.3.3(a). The inhomogeneity of the transverse distribution can be quantified using the spa-

tial Fourier transform [1]. Correspondingly, we consider the digitized image $I(x, y)$ associated to the transverse laser distribution and compute its two-dimensional (2D) Fourier transform $\tilde{I}(k_x, k_y)$ using the fast-Fourier-tranform (FFT) algorithm available in the PYTHON's NUMPY toolbox [66]. Here $k_x, k_y > 0$ are the spatial wavenumbers respectively associated to the horizontal and vertical direction. In order to simplify the comparison we further introduce the one-dimensional Fourier transform $\tilde{I}_x(k_x) = \int_0^{+\infty} \tilde{I}(k_x, k_y) dk_y$ along the horizontal axis [a similar definition holds for the vertical axis $\tilde{I}_y(k_y)$]. Figures 3.3 (d) and (g) respectively correspond to the 2D Fourier transform and the projection along the horizontal wavenumber k_x axis associated to the laser distribution displayed in Fig. 3.3 (a). It displays typical microstructures observed in previous runs at AWA, and the corresponding spectrum displays some small modulations at low frequencies with most of the spectral content below $k_i < 5$ mm^{-1}. It should be noted that the excessive beam distortion observed in Fig. 3.3(a) is the result of beam filamentation as the high-energy UV pulse propagates in the 20-m open-air optical transport system from the laser room to the accelerator vault.

When the MLA setup is configured to homogenize the beam [see Fig. 3.3(c)], the Fourier transform indicates that although the low frequency modulations seen in the original beam are suppressed, high-frequency modulations are still present for $k_x > 12$ mm^{-1}. These modulations have a bunching factor on the order of 10^{-2} and correspond to very small modulation wavelength (<0.5 mm) barely observable on the distribution; see Fig. 3.4.

Additionally, the MLA can be arranged to form a transversely-modulated laser distribution, the spectrum indicates a bunching factor at frequencies larger than the characteristic frequency associated to the total beam size; see Fig. 3.3(b,e,h). We should point out that the non cylindrical-symmetric (square shaped) pattern transferred to the electron beam is

[1] We note another popular technique to quantify the quality of an optical beam relies on the decomposition into Zernike's polynomials. Our choice to use the two-dimensional Fourier transform was motivated by the need to use one figure of merit to quantify *both* the quality of the homogenized beam and to also parameterize the modulated beam.

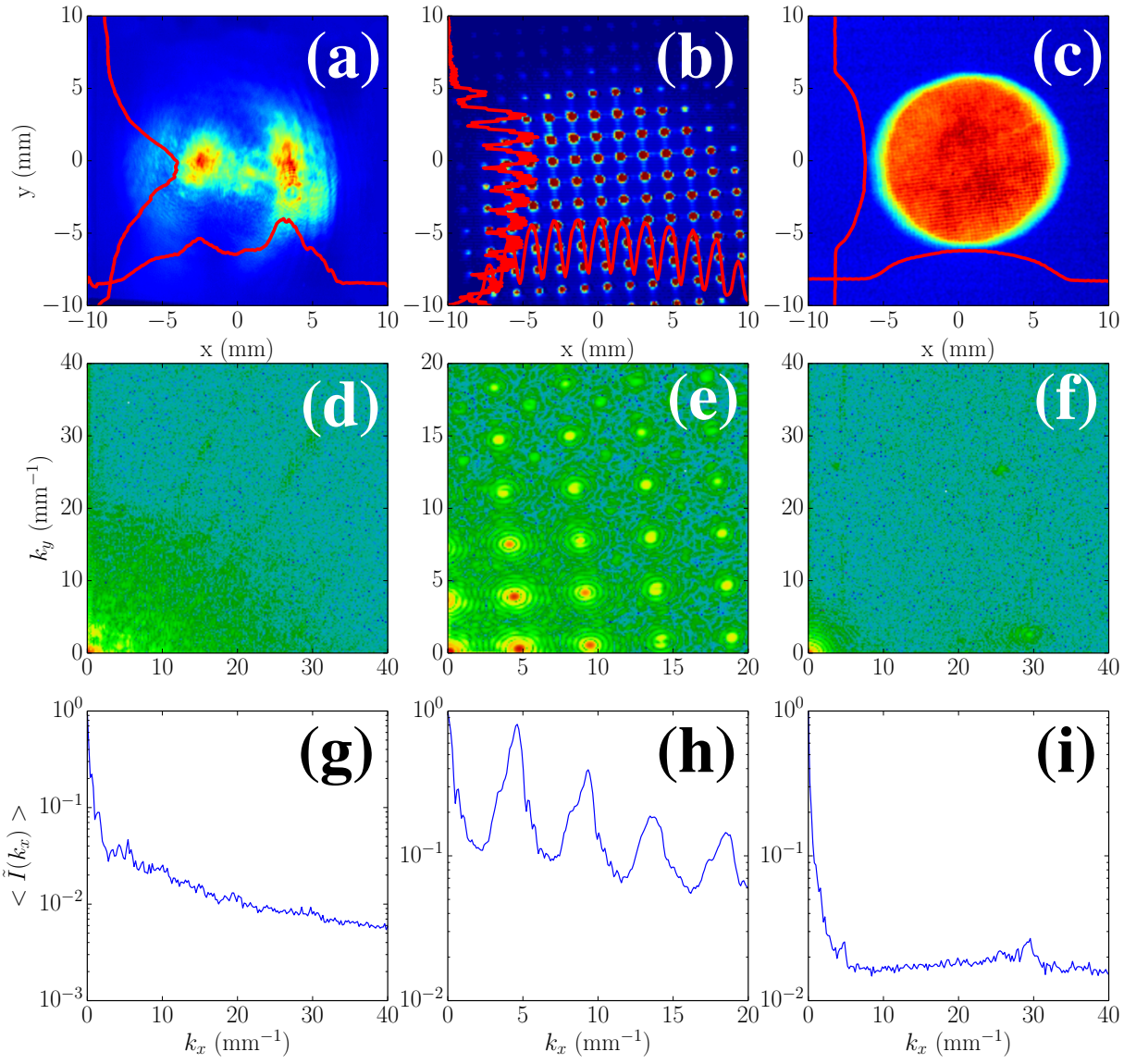

Figure 3.3: Measured UV laser without MLA (left column) and with MLA setup to produce beamlets (middle column) or as a homogenizer (right column). The upper, middle and lower rows respectively correspond to the laser transverse density distribution, its 2D FFT, and the projected spectrum along the horizontal frequency k_x.

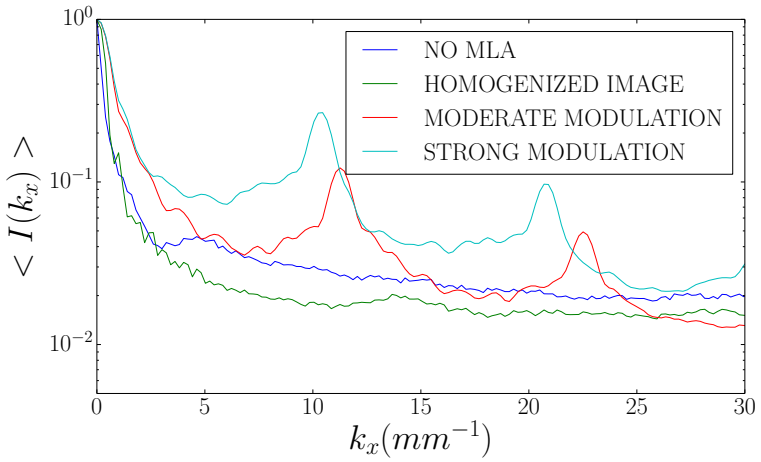

Figure 3.4: FFT spectrum along the horizontal axis $\tilde{I}(k_x)$ for the different positions of the convex lens. The blue trace corresponds to no MLA case. The green, red, and turquoise traces respectively correspond to the convex lens located at 250, 275 and 325 mm from the MLA array.

eventually rotated due to the Larmor precession in the solenoidal lenses commonly surrounding RF guns. It is therefore important to mount the MLA assembling on a rotatable optical stage for remote control of the final pattern angle. Such an approach would decouple the downstream focusing (when solenoids are employed) and ensure the final distribution does not have significant coupling between the two transverse degrees of freedom. Additionally, the fine control over the rotation of the final distribution could be used to select rotation angles with higher-order bunching to reach higher modulation frequencies, e.g., before injecting the beam in a transverse-to-longitudinal phase space exchanger to map the modulation into the temporal domain.

Figure 3.4 compares the projected horizontal Fourier spectra for four cases of MLA configurations. Each spectrum is obtained by averaging five measurements taken after f = 250 mm convex lens at 250 mm, 275 mm and 325 mm to study the off-focal modulation and pattern formation. The latter Figure confirms that in the homogenization regime, the MLA

setup significantly improves the image spectrum by suppressing the original low-frequency modulations in the beam.

Finally, we quantify the laser power loss in the devised setup. The MLA plates employed in our series of experiment do not have any UV anti-reflection (AR) coating, hence the power loss was $\sim 5\%$ per surface totaling $\sim 20\%$ for the two MLAs. Additionally, the AR-coated UV lenses introduce a power loss of $\sim 2\%$ per lens. In our optical setup the laser energy was measured to be 4.2 ± 0.1 and 2.5 ± 0.1 mJ respectively upstream and downstream of the MLA setup including the convex and four transport lenses. Such a measurement indicates an energy transmission of $\sim 60\%$ which could most likely be further improved in an optimized setup. However given the UV laser energy available during our proof-of-principle experiment and the real-estate constraints we did not performed such an optimization.

3.2 Application of the MLA as a laser homogenizer

The first set of experiments consisted in demonstrating the simple homogenization technique to improve the emittance of an accelerator. The experiment was performed in the AWA "drive-beam" accelerator (AWA-DB) diagrammed in Fig. 2.5.

3.2.1 Beam dynamics simulations

We carried out several simulations using the beam-dynamics program General Particle Tracker (GPT) [67] to explore the impact of the MLA-homogenized beam on the resulting emittance. Transverse inhomogeneities on the laser distribution at the photocathode surface are mirrored on the photoemitted electron bunch distribution. These imperfections result in asymmetric space-charge forces and eventually yield phase-space dilution

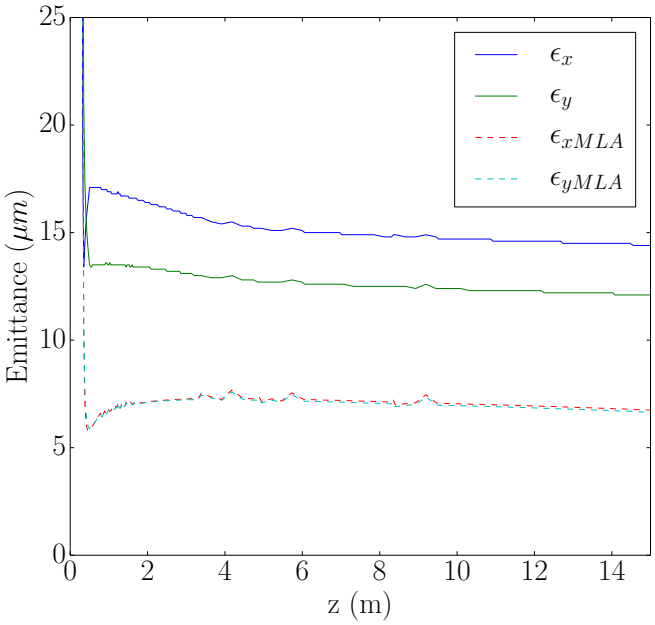

Figure 3.5: Evolution of the transverse normalized emittances along the AWA-DB beamline simulated with GPT for a 1-nC bunch. The simulations were performed using as initial condition both the measured nominal (solid trace) and homogenized (MLA, dashed traces) laser distributions. The ordinate z is the distance from the photocathode surface along the beamline.

that ultimately degrade the beam emittances [68]. Therefore the homogenized laser beam is expected to improve the beam transverse emittance.

The initial macroparticle distribution was produced using a Monte-Carlo generator using the measured transverse distribution of the laser similarly to Ref. [69]. The temporal laser distribution is taken to be Gaussian with RMS duration of σ_t = 2.5 ps, consistent with streak-camera measurements. The momentum of the macroparticle assumes an excess kinetic energy of 0.5 eV as typically considered for Cs_2Te cathodes [70]. We considered the nominal and homogenized laser distribution respectively shown in Fig. 3.3(a) and (c). To ensure a fair comparison, the total charge for both cases of distributions was set to 1 nC. Likewise, the RMS transverse sizes of the distribution was fixed to σ_c = 8 mm along both the horizontal and vertical directions. The simulations demonstrate that the beam transverse emittances

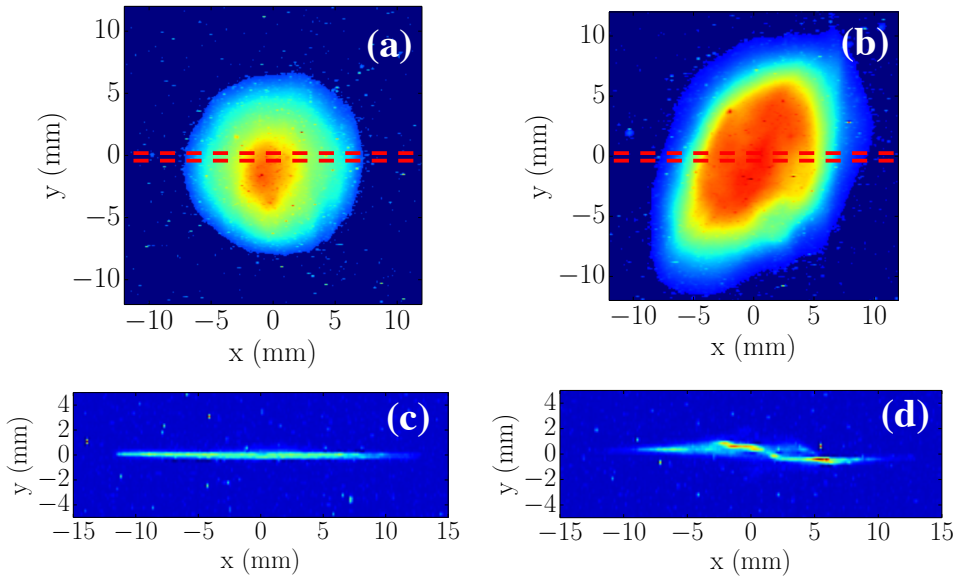

Figure 3.6: Beam transverse distribution at YAG5 (a,b) and associated distribution of the beamlet transmitted through a horizontal slit located at YAG5 location and measured at YAG6 (c,d). The set of images (a,b) [resp. (c,d)] corresponds to the case when the MLA was inserted [resp. retracted] from the laser-beam path. The horizontal dash line in (a,b) represent the aperture of the slit.

are reduced by a factor ~ 2 for the case of the homogenized laser distribution; see simulated row in Table 3.1 and Fig. 3.5.

3.2.2 Electron beam transverse emittance measurements

The experimental verification of the benefits of homogenizing the laser distribution was accomplished using the measured distribution of Fig. 3.3(a) and (c). For the homogenized distribution displayed in Fig. 3.3(c), a circular iris was used to clip the laser distribution and ensure it had the same rms value as in Fig. 3.3(a) $\sigma_c = 8 \pm 0.2$ mm. The resulting electron beam was transported through the nominal AWA-DB beamline and accelerated to

$p = 48 \pm 0.5$ MeV/c. The corresponding electron-beam transverse distributions measured at YAG5 are compared in Fig. 3.6(a,b).

Table 3.1: Comparison between measured and simulated beam parameters at YAG5 for $Q = 1 \pm 0.1$ nC. The experimental setup only allowed for the vertical normalized emittance to be measured. The parameters are all given as RMS quantities and corresponds to the distributions shown in Fig. 3.6.

parameter	experimental conditions		units
	No MLA	MLA	
Simulation with GPT			
momentum $\langle p \rangle$	48	48	MeV/c
σ_x	3.6	3.8	mm
σ_y	4.4	3.9	mm
σ'_x	4.6	1.7	$\times 10^{-2}$ mrd
σ'_y	3.1	1.5	$\times 10^{-2}$ mrd
ε_x	15.6	6.1	μm
ε_y	12.8	5.5	μm
Measurement			
momentum $\langle p \rangle$	48 ± 0.5	48 ± 0.5	MeV/c
σ_x	4.4 ± 0.2	4.0 ± 0.2	mm
σ_y	5.2 ± 0.2	3.7 ± 0.2	mm
σ'_y	4.2 ± 1.3	3.3 ± 1.0	$\times 10^{-2}$ mrd
ε_y	20.5 ± 7.4	11.6 ± 4.3	μm

The distribution originating from the initial (inhomogenized) does not present any distortion except for beam asymmetric and having some $x - y$ coupling. In contrast, the homogenized distribution is cylindrically symmetric and does not show any coupling. To further quantify the improvement we measured the beam vertical emittance using the slit technique. A 100-μm wide horizontal slit was inserted at YAG5 and the transmitted beamlet was observed 3.1 m downstream at YAG6 thereby providing the beam divergence σ'_y. Such a measurement together with the vertical beam-size measurement at YAG5 σ_y provide an estimate of the normalized vertical emittance via $\varepsilon_y = \beta\gamma\sigma_y\sigma'_y$, where $\beta \approx 1$ and $\gamma = 93.9$.

It should be stressed that the reported emittances is the core emittance and does not fully characterize the beam transverse phase space. Nevertheless this quantity provides a figure of merit to investigate the impact of the MLA on the beam quantity. The resulting beamlet distributions at YAG5/6 are shown in Fig. 3.6(b,d) and the measured divergence and resulting emittance compared in Tab. 3.1.

The resulting emittances are comparable with the value simulated with GPT (Fig. 3.5) and indicate a factor ~ 2 improvement for when the homogenized laser beam is employed. The relatively large error bars in Tab. 3.1 are due to hardware uncertainty (mostly the slit width). It should be noted that the errors between the two measurements are correlated, i.e. the uncertainty leads to the upper (resp. lower) value for simultaneously the "MLA" and "No MLA" measurements, thereby giving confidence, despite the large error bar on the emittance, that the emittance reduces when the MLA is used to homogenize the laser beam. It should finally be pointed out that the reported emittance were produced with a nominal setup of the AWA-DB beamline, i.e. no emittance-minimization technique was attempted prior to the measurements.

3.2.2.1 Application of Voronoi diagrams in pepper-pot emittance measurements

In this Section we discuss a possible improvement of the slit emittance measurement method discussed in Sec. 3.2.2 with a Voronoi diagram technique. Voronoi diagram is a method of dividing a plane into subsets with bisectors drawn between given points. It was proposed by G. Voronoi in 1908 [71] and since then has been employed in various fields of Science and Industry, e.g. in image segmentation, tessellation algorithms, computational geometry problems [72]. Besides emittance measurements this method can benefit to charged particle beams phase-space analysis and particle-in-cell codes improvement [73].

To illustrate the process of drawing Voronoi diagram, consider a set of points arranged in (x, y)-plane; see orange circles Fig. 3.7. First, a pair of neighboring points is connected with a line segment and a perpendicular bisector is drawn onto that segment. When bisectors from different segments intersect, they form a Voronoi vortex (intersection point), and Voronoi cells -convex or concave polygons, depending on the number of original points and its position on the diagram; see Fig. 3.7. Note, that for the case of perfectly grid-lined point formation each cell (excluding edge cells) will have exactly four vortices and a rectangular shape with the side equal to the spacing between points. When a distortion is introduced to such formation, the cells become convex polygons, thus as a measure of the distortion the average cell area can be used. Since each cell contains a point of interest in its geometric center, the (x, y)-plane is automatically segmented into regions of interest which can be independently considered for further analysis.

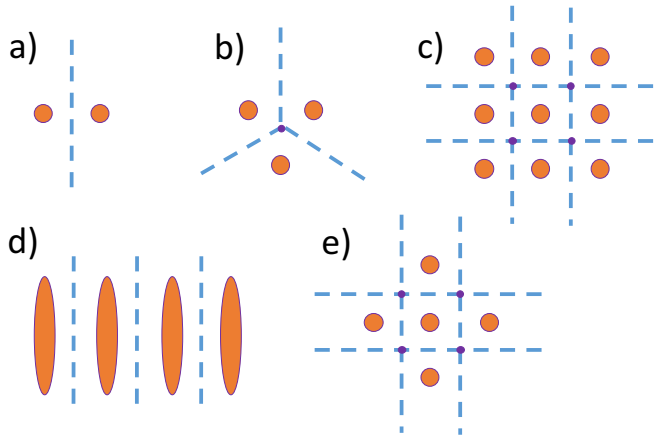

Figure 3.7: Examples of Voronoi diagrams drawn for different arrangements of initial points. a) and b) demonstrate the principle of a diagram, c) - e) display diagrams for most common tungsten mask configurations.

One of the most common methods of measuring charged particles beam emittance is an intercepting tungsten mask or slit. The mask is followed by transverse-density diagnostics

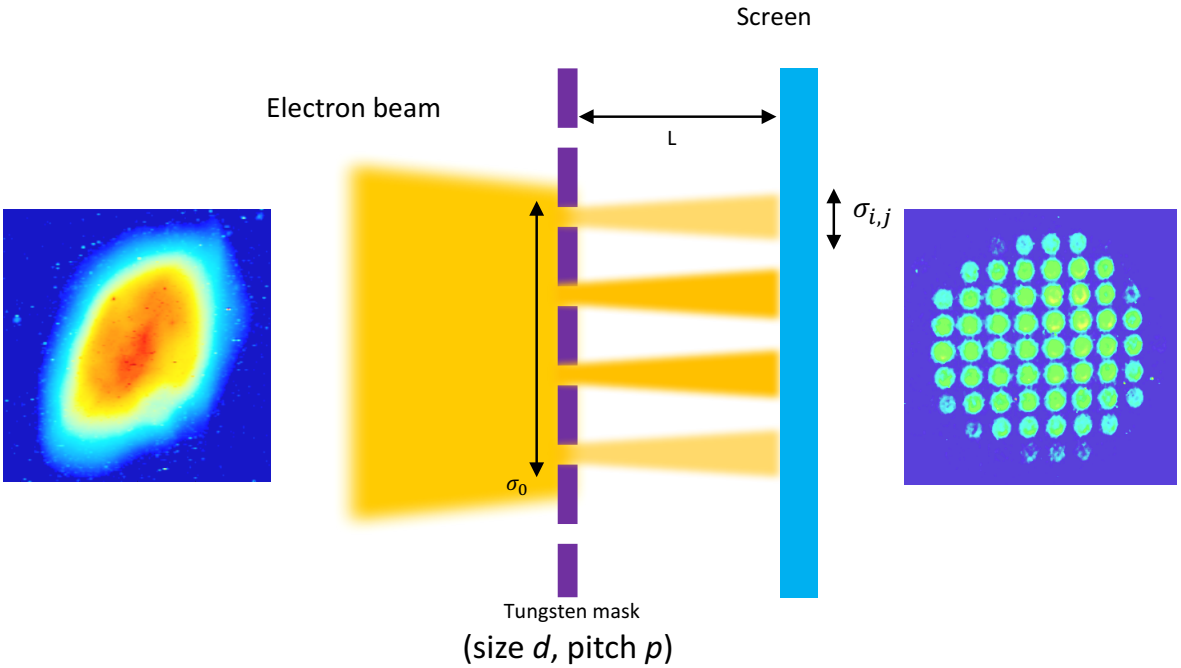

Figure 3.8: Schematics of the pepper pot emittance measurement technique. Electron beam (left inset) is propagated through the tungsten mask with periodic perforation in (x, y)-plane and resulting bunch-lets are recorded at the screen downstream of the mask (right inset).

(typically a scintillating screen) where the bunch-let formation is observed; see Fig. 3.8. The resulting emittance $\epsilon_{rms}^2 =< x^2 >< x'^2 > - < x'x >^2$ is deduced from known parameters of the mask (size d, pitch p), beam size at the mask, distance to the screen L and measured RMS size of each bunch-let [52]. Circular masks of cross- and grid-shape were manufactured and used for 4D emittance measurements at AWA facility [74, 75]. The main purpose of this section is to amend these studies with a new emittance calculation algorithm, described below.

In a first step, all the beamlets are located via 2D peak finding algorithm and initial Voronoi diagram is generated; see Fig. 3.9. The edge polygons are discarded based on the intensity threshold, and given patch [Fig. 3.9 (b)] is further reanalyzed. As it can be seen on Fig. 3.9, some beamlets appear to have peculiar hot spots away from its center,

therefore distorting the Voronoi diagram. To alleviate this problem, a statistical center-of-mass calculation is done to refine the beamlet coordinates and therefore ensure the mesh is equally sparse with each patch containing only one beamlet; see Fig. 3.9 (c). After the mesh refinement, statistical RMS values of σ_x, σ_y and beamlet relative positions are computed. The resulting value of the emittance can be deduced from well-known formula [52]:

$$\epsilon_{rms}^2 \approx \frac{1}{N^2}\left(\left[\sum_{j=1}^{m} n_j(x_{sj}-\bar{x})^2\right]\left[\sum_{j=1}^{m}\left(n_j\frac{\sigma_j^2}{L^2}+n_j(\bar{x_j'}-\bar{x'})^2\right)\right] - \left[\sum_{j=1}^{m} n_j x_{sj}\bar{x_j'} - N\bar{x}\bar{x'}\right]^2\right),$$

where N - total number of particles (integrated intensity of the region of interest), n_j - number of particles traveled through j-th slit (j-th beamlet intensity), m - total number of beamlets analyzed, $\bar{x}$ - mean position of all beamlets, $\bar{x'}$ - mean divergence of all beamlets, σ_j - RMS size of the beamlet, x_{sj} - j-th beamlet position, L - distance between mask and screen.

More densely perforated masks provide better statistical probe of the beam phase space, however, it increases the complexity of the bunch-let formation image analysis. The Voronoi diagram method can serve as fast and yet simple method of image segmentation. The mesh generation procedure is easily accessible via PYTHON-SCIPY package.

To perform pepper-pot emittance measurement procedure, 9 micron circular mask was inserted at the slit location on Fig. 2.5. 1 nC 48 MeV electron beam was then propagated through the mask and the electron distribution was registered at the YAG6 location downstream of the mask. None of the electron emittance, perforation spacing and screen location optimization procedures were applied prior to the experiment, however the acquired data gives a good test case for debugging and testing. The resulting measured normalized core

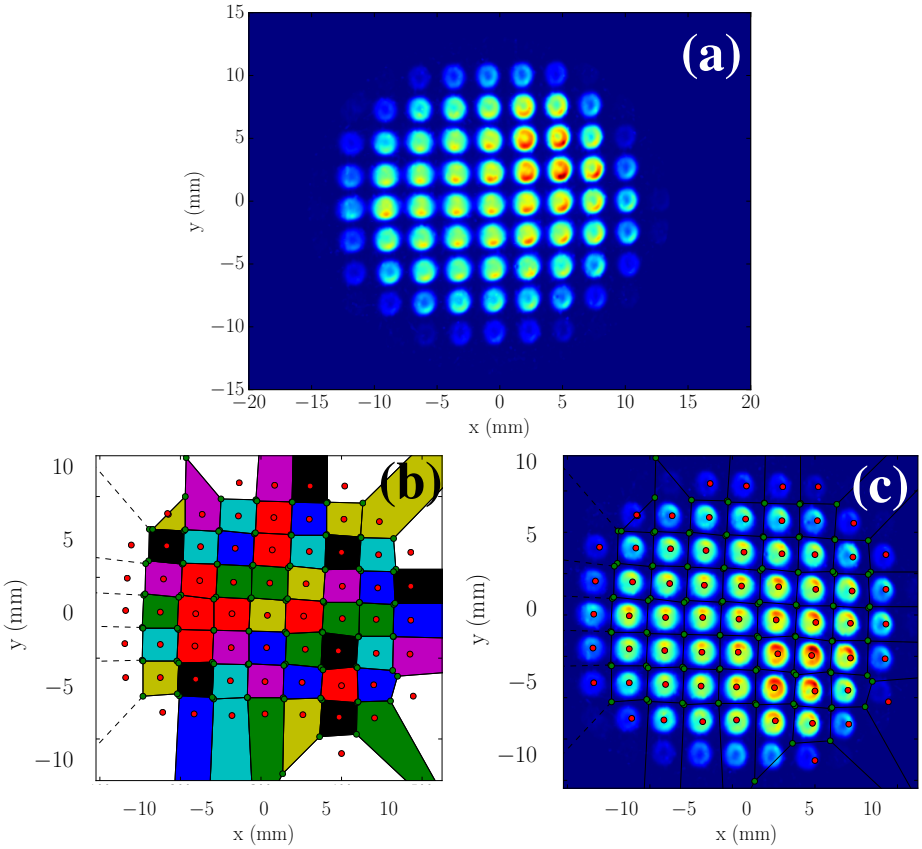

Figure 3.9: Demonstration of Voronoi mesh generation for emittance measurement. (a) Original pepper-pot segmented beam image. (b) and (c) Patches for separate beamlets (randomly colored) and masked beam image respectively.

emittance values are ϵ_x=6.5 μm±0.7 μm and ϵ_y=7.2 μm ±0.9 μm for horizontal and vertical planes respectively for the MLA formed beam.

Note that in pepper-pot emittance measurement and in multi-beam pattern analysis Voronoi diagram remains independent of image rotation angle, which is an advantage in comparison to simple grid-like image segmentation. In conclusion, such a method can improve the accuracy of the emittance measurement by better handling of densely perforated masks. The technique can be also applied for transverse modulation beam image analy-

sis. The applications of Voronoi diagrams in Beam Physics are not limited to the discussed examples.

3.3 Production and transport of multi-beam arrays

In this Section we discuss the formation of transversely-segmented beams – i.e. consisting of an array of beamlets. Such a distribution could have a variety of applications such as described in Refs. [76, 77]. Alternatively, the formed array could produce a transversely modulated beam that could be injected in a transverse-to-longitudinal phase-space exchanger to yield a temporally-modulated beam [78, 79]. The latter opportunity motivated the present work to demonstrate the generation and preservation of an array of beamlets up to the entrance of a transverse-to-longitudinal phase-space exchanger installed in the AWA-DB [80] and recently employed for temporal shaping [81]. Additionally, the multi-beam may serve as a beam-based diagnostic tool, e.g., to investigate nonlinearities of the externally-applied electromagnetic field or measure transfer matrices of beamline elements. In this section, we explore whether the beam transverse electron-beam modulation originating from the laser is preserved during the photoemission processes and low-energy acceleration in the RF gun.

3.3.1 Beam dynamics simulations

Using the particle tracking codes GPT and IMPACT-T [22] we performed simulation of the AWA-DB RF-gun beam dynamics. The preservation of the modulation is affected by space-charge forces which play a dominant role in the beam dynamics in the vicinity of the cathode and in the RF gun. Given the multi-scale nature of our problem, the space-charge

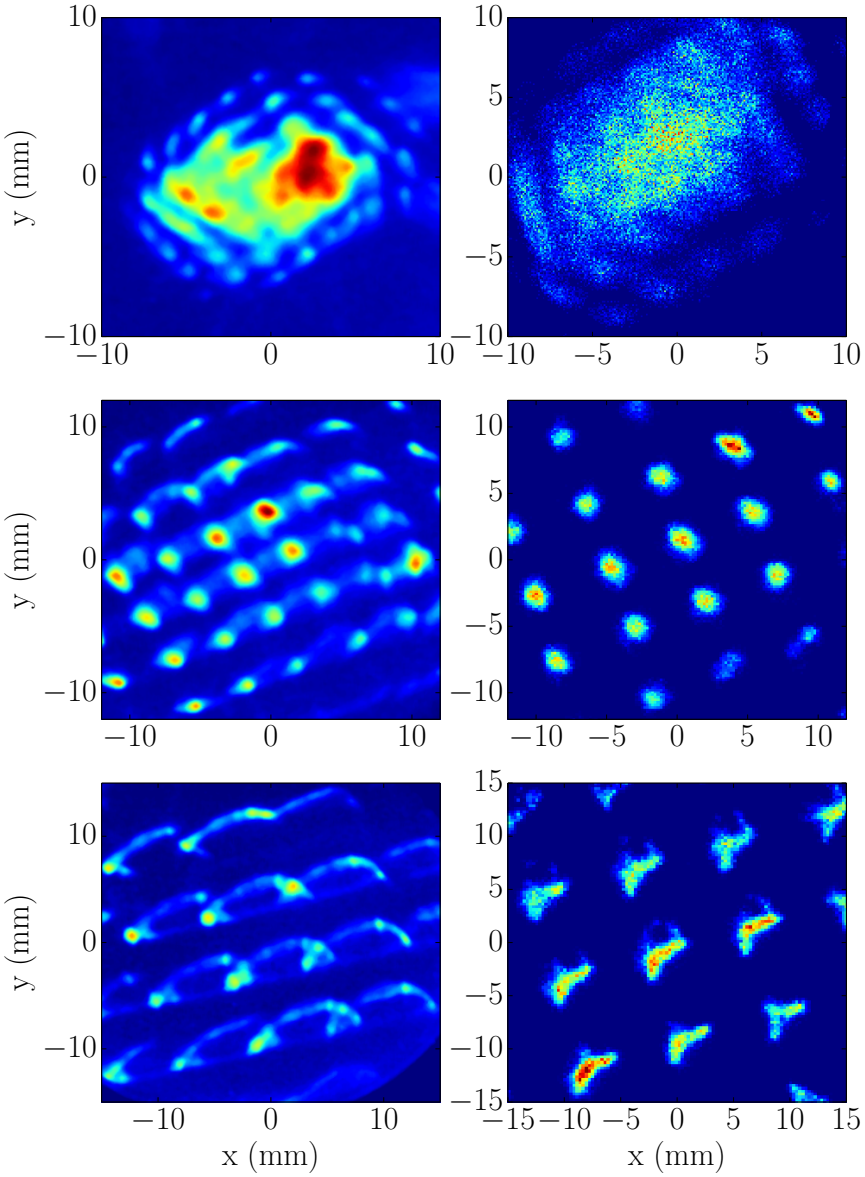

Figure 3.10: Measured (left) and simulated (right) Q=100 pC electron-beam distribution at YAG1 when the UV laser pulse is modulated with the MLA array. The rows correspond to different matching-solenoid current settings of 215 A (upper row), 230 A (middle row) and 290 A (lower row).

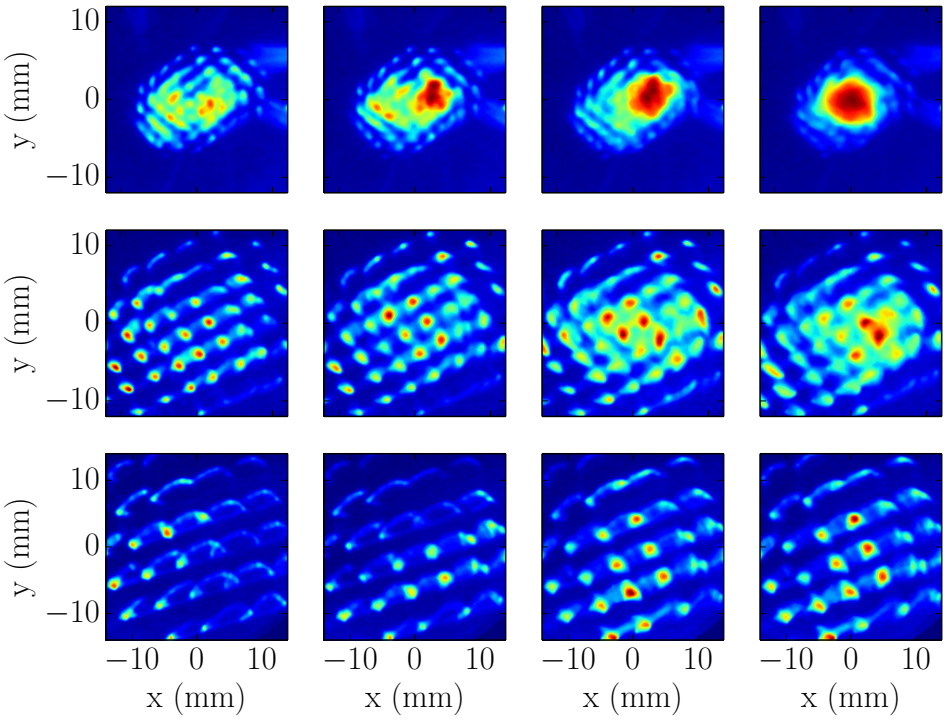

Figure 3.11: False color measured 7 MeV electron beam patterns for various matching solenoid current setting and charge. From left to right: Q=60pC, 80pC, 100pC, 120pC. The images from top to bottom correspond to matching-solenoid currents of 215, 240, and 270 A.

forces are computed with a Barnes-Hut (BH) algorithm [82] available in GPT. This algorithm was successfully tested in recent studies [83, 84] and is described in detail in Chapter 6.

The measured transversely-modulated laser distribution at the photocathode location [similar to Fig. 3.3(b)] was used to generate the input macroparticle distribution for our numerical simulations. An initial intent was to probe whether the modulation could possibly be amplified via collective effects (e.g. implying transverse space charge modulations that will eventually convert into energy modulations) or if they are simply smeared out via thermal-emittance effect as the beam is photo-emitted.

The beamlet pattern was also used to ensure the GPT model could reproduce our experimental observation at low energy (RF-gun only). We compare the simulated and measured

transverse patterns for different matching-solenoid current settings in Fig. 3.10. The beam data and numerical simulations were recorded downstream of the gun using YAG1 at a beam energy of 7 ± 0.5 MeV and bunch charge was set to 150 pC. The observed pattern rotation indicates that the Larmor angle which depends on the beam energy and applied magnetic field agrees qualitatively with the simulation; see Fig. 3.10. The observed discrepancy is caused by the uncertainties on the RF-gun field.

3.3.2 Multi-beam formation downstream of the RF gun

A subsequent experiment investigated the formation of a beamlet array downstream of the RF gun at an energy of 7 ± 0.5 MeV for various operating points of the photoinjector. The incoming laser spot size on the MLA array was chosen to yield an 8×8 beamlet array. The photoemitted electron beam was observed on the YAG:Ce scintillating screen (YAG1 in Fig 2.5) located at $z = 3.1$ m from the photocathode surface. Figure 3.11 displays a sequence of beam distributions recorded at YAG1 for different settings of the focusing-bucking and matching solenoids. Note, that due to the surface space charge effects, the charge associated to each beamlet, and therefore the total maximum charge of the patterned beam, is limited. The total maximum charge of the patterned beam was measured to be approximately ~ 15 nC corresponding to an average charge of $\sim (15\ \text{nC})/(8 \times 8) \simeq 200$ pC per beamlet.

The resulting electron beamlet formations pictured on Fig. 3.11 were analyzed using the same Fourier analysis as the one used in Section 3.1.2 for the UV-laser images. Figure 3.12 (a) summarizes the evolution of the transverse bunching factor at its lowest-frequency maximum versus total bunch charge for different matching solenoid settings. The average beamlet separation d changes from 0.4 mm to 8 mm at YAG1 location with the matching solenoid

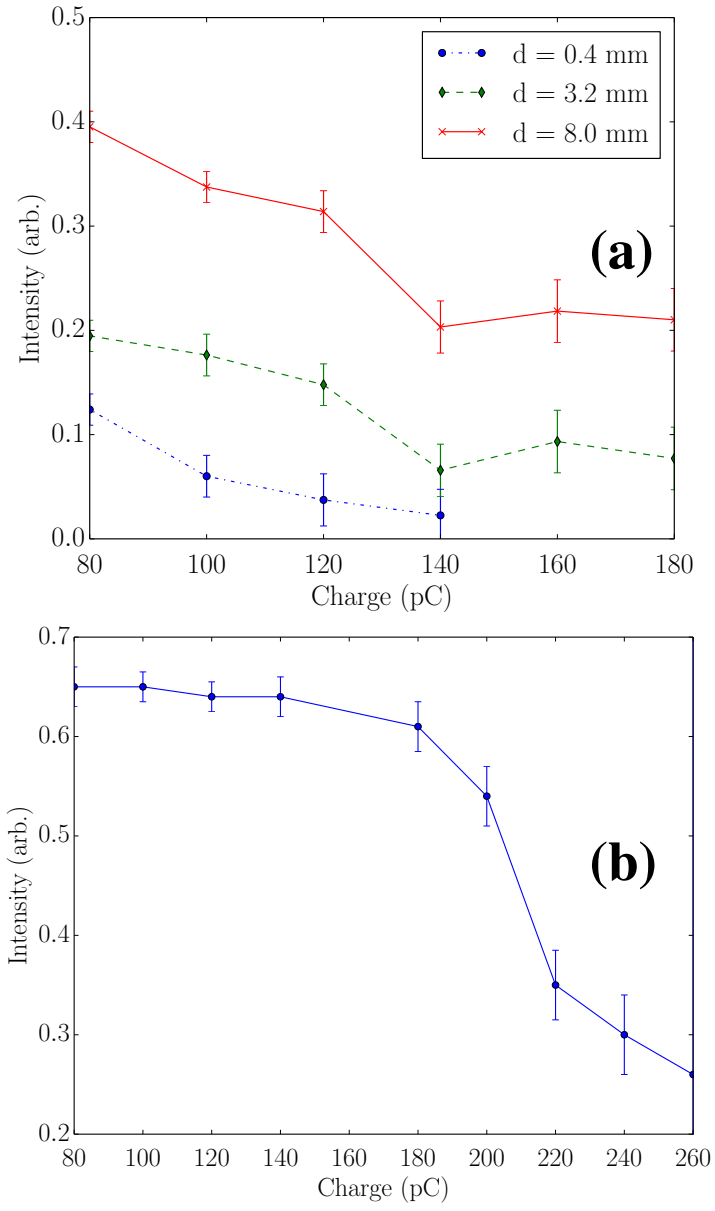

Figure 3.12: Transverse bunching factor evaluated at its lowest-frequency maximum versus bunch charge for the three cases of solenoid settings displayed in Fig. 3.11 with corresponding beamlet spacing d (a) and for the case of a solenoid field of 290 A with associated beamlet spacing of d = 10 mm (b).

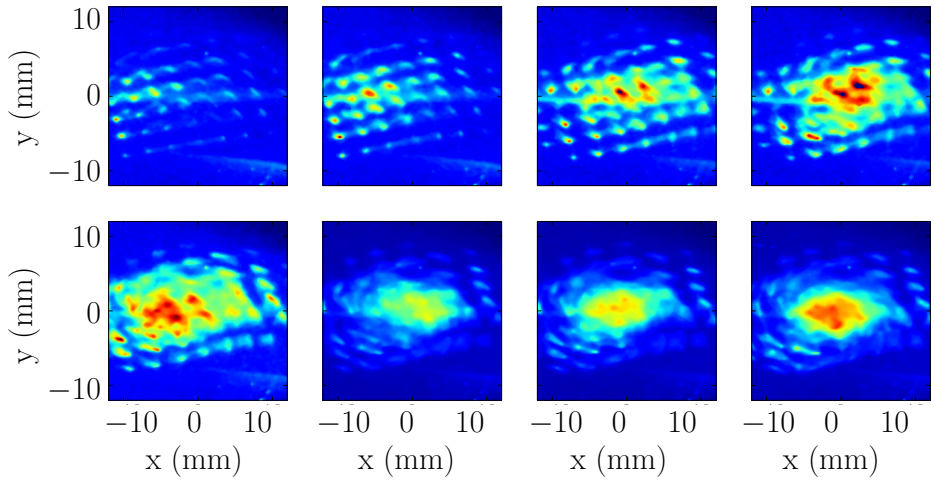

Figure 3.13: False color measured 48 MeV electron-beam patterns for various charges. From left to right and top to bottom: Q = 60, 100, 200, 300, 400, 500, 600, 700 pC with a matching-solenoid current of 240 A.

current increased from 215 A to 270 A. Figure 3.12 (b) gives the evolution of the transverse bunching factor for the case of $d = 10 \pm 0.4$ mm. One can see the modulation is fully determined by solenoid imaging at charges of $Q < 180$ pC.

Finally, it should be noted, that the measurements were taken at YAG1 and do not provide information on possible modulation reappearance at a downstream position along the beamline: the betatron phase advance at a downstream observation point could be such that the modulation is washed out in the position space but prominent in the angular coordinate.

3.3.3 Multi-beam acceleration to 48 MeV

The modulation introduced on the cathode was propagated and preserved through the beamline up to the transverse-to-longitudinal emittance-exchange (EEX) beamline entrance;

see Fig. 3.13. There should be no strong focusing applied along the low-energy beamline as close encounter of the beamlets produces strong distortion as explored in Ref. [69]. Consequently, the low-energy beamline elements should be properly matched to allow the large waist. At medium energy, the transverse space-charge force is significantly decreased and therefore not expected to impact the multi-beam dynamics. In order to avoid a tight waist at low energy we used the linac solenoid LS1 (see Fig. 2.5) to image the beamlet pattern directly on the YAG5 screen located 14 m downstream of the photocathode surface and just prior to the EEX beamline. At this location, the beam energy is measured to be 48 MeV. Figure 3.13 shows the beam distribution at YAG5 for different bunch charge. The typical beamlets separation (center to center) is on the order of $\sim$ 3 mm $\pm$0.3 mm. Such a distribution could be further manipulated using a telescope composed of four quadrupole magnets to generate a train of short bunches along the temporal axis downstream of the EEX beamline [81]. EEX formed bunch train could possibly support the generation of THz radiation using, e.g., coherent transition radiation, or the resonant excitation of wakefields in a high-impedance structure such as a dielectric-lined waveguide [85].

CHAPTER 4
ACCELERATING CAVITY TRANSPORT MATRIX MEASUREMENT

In this Chapter we present the experimental results of the transfer map measurement described in Section 1.3.5.1 Previously, the transverse matrix of a standing-wave accelerating structure (a plane-wave transformer, or PWT) was reported in Ref. [36] and benchmarked against an "augmented" Chambers' model detailed in [33]. This refined model accounts for the presence of higher-harmonic spatial content in the axial field profile $E_z(r = 0, z)$. Here we extend such a measurement to the case of a 1.3-GHz SRF accelerating cavity, detailed in Sec. 2.1.1.1. We note that the measurements performed at the IOTA/FAST facility were in a regime where the energy gain through the cavity is comparable to the beam injection energy [$\gamma_i \sim \gamma' L$].

4.1 Beam dynamics simulations

In order to quantitatively investigate the transverse beam dynamics in the cavity, we consider a monoenergetic distribution of macroparticles arranged on the vertices of a 2×2 transverse grid in the (x, y) plane with distribution $\sum_i \sum_j \delta(x - i\Delta x)\delta(y - j\Delta y)$ where $\delta(x)$ is Dirac's function and taking $\Delta x = \Delta y = 0.3$ mm. The macroparticles, with vanishing incoming transverse momenta and located within the same axial position, are tracked through the cavity field and their final transverse momenta recorded downstream of the cavity. Figure 4.2(a) displays the change in transverse momentum $\delta P_\perp$ imparted by the auxiliary couplers nor-

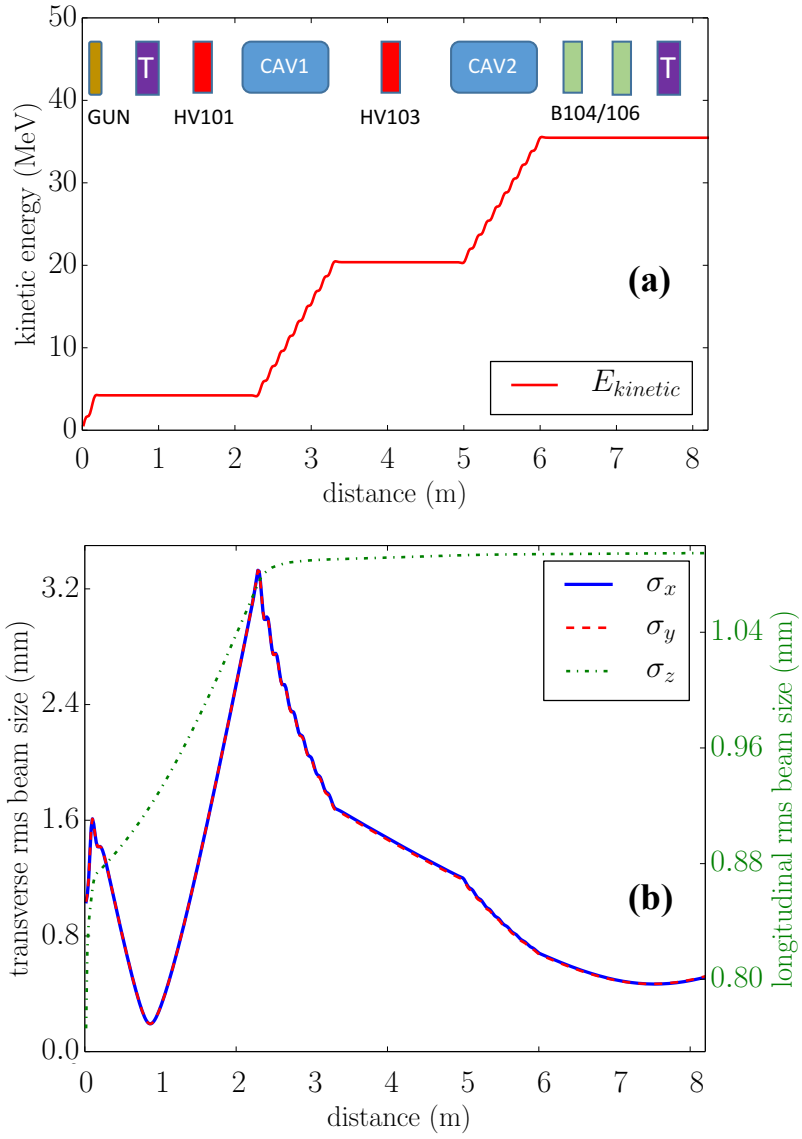

Figure 4.1: Experimental setup under consideration and associated energy gain (a) and transverse and longitudinal bunch sizes (b) simulated with ASTRA . In the diagram displayed in (a), the labels "CAV" , "T", "HV", and "B" respectively correspond to the SRF cavities, the integrated-current monitors (ICM), the magnetic steerers, and beam-position monitors.

malized to the change in longitudinal momentum $\delta P_{\|}$. This is computed as the difference between ASTRA simulations using the cylindrical-symmetric field [Fig. 4.2(b)] from the ones based on the 3D field map [Fig. 4.2(c)]. Figure 4.2(a) indicates a strong dipole-like field and

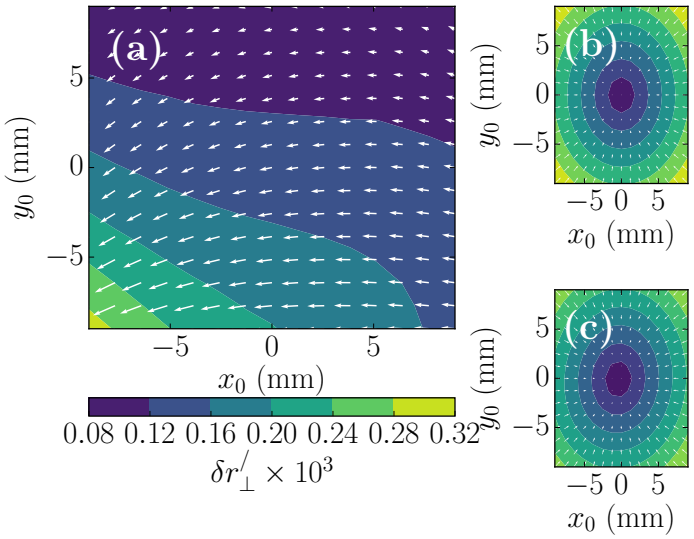

Figure 4.2: Transverse momentum magnitude (false color contours) and directions (arrows) simulated downstream of the cavity as a function of initial positions. Plot (a) displays the momentum-kick contribution from the auxiliary couplers only, i.e. $\delta \boldsymbol{r'}_\perp \equiv \frac{1}{\delta P_\parallel} |\delta \boldsymbol{P}_\perp - k_p \boldsymbol{r}_{\perp,0}|$, where $\delta P_\parallel$ is the increase in longitudinal momentum. Plots (b) and (c) show respectively the transverse momentum simulated using the cylindrical-symmetric (b) and the 3-D field map (c) models for the cavity. Plot (a) is obtained as the difference between plots (c) and (b). These simulations were performed for 10-MeV electrons with $E_0 = 30$ MV/m (corresponding to $\bar{G} \simeq 15$ MeV/m) and $\phi = 0°$.

also hints to the presence of higher-moment components. To further quantify the impact of the auxiliary couplers, we write the change in transverse momentum as an electron passes through the cavity $\delta \boldsymbol{P}_\perp \equiv (\delta p_x, \delta p_y)^T$ as an affine function of the input transverse coordinates $\boldsymbol{r}_{\perp,0} \equiv (x_0, y_0)^T$ (here the superscript ^{T} represents the transpose operator)

$$\delta \boldsymbol{P}_\perp = \boldsymbol{d} + M \boldsymbol{r}_{\perp,0}, \tag{4.1}$$

where $\boldsymbol{d} \equiv (d_x, d_y)$ is a constant vector accounting for the dipole kick along each axis, and $\boldsymbol{M}$ is a 2×2 correlation matrix. The latter equation can be rewritten to decompose the final momentum in terms of the strength characterizing the various focusing components [86]

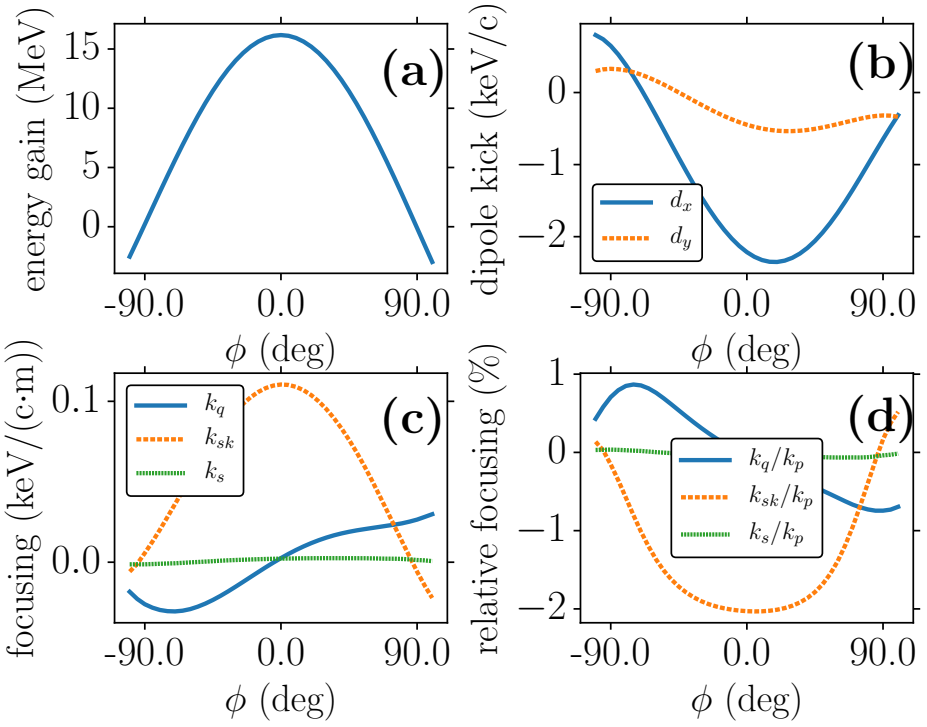

Figure 4.3: Energy gain (a), dipole kicks (b), absolute (c) and relative (d) focusing strengths as function of phase ($\phi = 0$ corresponds to on-crest acceleration). The relative focusing strength is normalized to the ponderomotive focusing strength k_p in Eq. 4.2. The simulation conditions are an injection energy of 10 MeV and $E_0 = 30$ MV/m.

$$\begin{pmatrix} \delta p_x \\ \delta p_y \end{pmatrix} = \begin{pmatrix} d_x \\ d_y \end{pmatrix} + k_p \begin{pmatrix} x_0 \\ y_0 \end{pmatrix} + k_q \begin{pmatrix} x_0 \\ -y_0 \end{pmatrix} + k_{sk} \begin{pmatrix} y_0 \\ x_0 \end{pmatrix} + k_s \begin{pmatrix} y_0 \\ -x_0 \end{pmatrix}, \tag{4.2}$$

where $k_{p,q} \equiv (M_{11} \pm M_{22})/2$, and $k_{sk,s} \equiv (M_{12} \pm M_{21})/2$ respectively account for the axially-symmetric ponderomotive, quadrupole, skew-quadrupole and solenoidal focusing effects. It should be pointed out that the coefficients introduced in the latter equation are implicit functions of the cavity field and operating phase. Furthermore, the linear approximation

resulting in Eq. 4.1 requires validation. In order to find the focusing strength we performed simulations similar to the one presented in Fig. 4.2(c) and directly compute the offset $\boldsymbol{d}$ and correlation matrix $\boldsymbol{M}$ necessary to devise the focusing strengths in Eq. 4.2. Such an analysis was implemented to provide the steering and focusing strength as a function of the injection phase ϕ as summarized in Fig. 4.3. Our analysis confirms the presence of higher-moment components such as quadrupole and skew-quadrupole terms as investigated in Ref. [87]. It also indicates the strength of these quadrupolar components is very small compared to the cylindrical-symmetric ponderomotive focusing, specifically $k_{sk} \sim k_q \sim O(10^{-2} \times k_p)$. Finally, we observe that the solenoidal contribution $k_s \sim O(10^{-4} \times k_p)$ is insignificant. The relatively weak focusing strength arising from the presence of the auxiliary couplers confirm that the transfer matrix will be essentially dominated by the ponderomotive focusing. Therefore we expect the couplers to have negligible impact on the transfer-matrix measurement reported in the next Section. It should however be noted that the time dependence of these effects, especially of the dipole kick, can lead to significant emittance increase via a head-tail effect where different temporal slice within the bunch experience a time-varying kick resulting in a dilution of transverse emittance. Such an effect is especially important when low-emittance low-energy beams are being accelerated in a string of cavities [25, 27, 3].

4.2 Reference orbit method and experimental procedure

The experimental setup is diagrammed in Fig. 4.1(a). In the present experiment the average accelerating gradient of the accelerating cavities was respectively set to $\bar{G}_{CAV1} \simeq$ 15 MeV/m and $\bar{G}_{CAV2} \simeq 14$ MeV/m. The simulated bunch transverse sizes and length along the IOTA/FAST photoinjector appear in Fig. 4.1 for the nominal bunch charge ($Q = 250$ pC) and settings used in the experiment. The corresponding peak current, $\hat{I} \simeq 30$ A, is small

enough to ensure wakefield effects are insignificant – from From Fig. 4 of Ref. [38] we estimate the transverse geometric wakefield to yield a kick on the order of 1 eV/c, i.e., two order of magnitude lower than the dipole kick given in Fig. 4.3 over the range of phase $\phi \in [-30°, 30°]$. The simulated kinetic energy downstream of CAV2 is $K \simeq 34$ MeV consistent with the measured value.

Beam position monitors (BPMs) which were the main diagnostics used duing our experiment. At the time of our measurements, the BPM system was still being commissioned and the resolution was about $\simeq 80$ μm in both dimensions [88].

As the starting point of the transfer-matrix measurement, the beam was centered through both cavities CAV1 and CAV2 using a beam-based alignment procedure. The beam positions (x_i, y_i) [where $i = 1, 2$] downstream of the CAV2 were recorded for two phase settings ($\phi_{1,2} = \pm 30°$) and the function $\chi = \sqrt{(x_1 - x_2)^2 + (y_1 - y_2)^2}$ quantifying the relative beam displacement was evaluated. The settings of the dipole correctors upstream of the cavity CAV2 were then employed as free variables to minimize χ using a conjugate-gradient algorithm.

In order to measure the transfer matrix, we used a standard difference-orbit-measurement technique where beam-trajectory perturbations are applied with magnetic steerers located upstream of CAV2 and resulting changes are recorded downstream of the cavity with a pair of BPMs. In our experiment, the perturbations were applied using two sets of horizontal and vertical magnetic steerers (HV101 and HV103) with locations displayed in Fig. 4.1(a). Orbit perturbations were randomly generated to populate a large range of initial conditions in the 4D trace space $\mathbf{X_i} \equiv (x_i, x_i', y_i, y_i')$. Only the perturbations for which the beam was fully-transmitted were retained [the charge transmission is inferred from two integrated-current monitors (ICM) shown in Fig. 4.1(a)]. For each measured cavity phase point, 20 different sets of perturbations (associated to a set of upstream dipole-magnet settings) were impressed.

The beam was then propagated through CAV2 up to a pair of downstream electromagnetic button-style BPMs. The measurement of beam position with CAV2 "off" and "on", where "off" means zero accelerating gradient, (indirectly) provided the initial $\mathbf{X_i}$ and final $\mathbf{X_f}$ beam positions and divergences respectively upstream and downstream of CAV2.

Correspondingly, given the 4×4 transfer matrix of the cavity R, these vectors are related via $\mathbf{X_f} = R\mathbf{X_i}$. An initial perturbation $\delta\mathbf{X_{0_i}}$ to the nominal orbit $\mathbf{X_{0_i}}$ such that $\mathbf{X_i} = \mathbf{X_{0_i}} + \delta\mathbf{X_{0_i}}$ will result in an orbit change downstream of CAV2 given by

$$\delta\mathbf{X_{0_f}} = R\delta\mathbf{X_{0_i}}. \tag{4.3}$$

Therefore any selected orbit can serve as a reference orbit to find the transformation R, assuming the set of perturbed trajectories around this reference is transformed linearly (which is the essence of the paraxial approximation). Consequently, impressing a set of N initial perturbations $\delta\mathbf{X}_{0_i}^{(n)}$ where $n = [1...N]$ results in a system of N equations similar to Eq. 4.3 which can be casted in the matrix form

$$\Xi_f = R\Xi_i, \tag{4.4}$$

where Ξ_j $(j = i, f)$ are $4\times N$ matrices containing the positions and divergence associated to the N orbit perturbations. This system can then be inverted via a least-squares technique to recover R.

The error analysis includes statistical fluctuations (which arise from various sources of jitter) and uncertainties on the beam-position measurements. The statistical error bars were evaluated using an analogue of a boot-strapping technique. Given that the transformation (4.3) is linear, any couple of initial $\mathbf{X_{k,i}}$ and final $\mathbf{X_{k,f}}$ beam position measurements can define the reference orbit while the other couples $(\mathbf{X_{j,i}}, \mathbf{X_{j,f}})$ for $j \in N \neq k$ are taken as

perturbed orbits and the transfer matrix can be inferred. Consequently, we retrieved the transfer matrix R_j associated to a reference orbit $(\mathbf{X_{k,i}}, \mathbf{X_{k,f}})$. Such a procedure is repeated for all orbits $k \in [1, N]$ and the resulting transfer matrix R_k is recorded. A final step consists in computing the average $\langle R \rangle$ and variance $\sigma_R^2 = \langle R^2 - \langle R \rangle^2 \rangle$ over the N realizations of R_j. Finally, the measured value is reported as $R = \langle R \rangle \pm 2\sigma_R$.

4.3 Transfer matrix measurement results

The elements of the transfer matrix were measured for nine values of phases in the range $\phi \in [-20°, 20°]$ around the maximum-acceleration (or "crest") phase corresponding to $\phi = 0°$.

For each set of perturbation the beam positions along the beamline were recorded over 4 shots to account for possible shot-to-shot variations arising from beam jitter or instrumental error. The corresponding set of 80 orbits were subsequently used in the analysis algorithm described in the previous Section.

The comparison of the recovered transfer matrix elements with the Chambers' model along with the matrix inferred from particle tracking with ASTRA appear in Fig. 4.4. The shaded areas in Fig. 4.4 and subsequent figures correspond to the simulated uncertainties given the CAV2 cavity gradient $\bar{G}_{CAV2} = 14 \pm 1$ MeV/m.

Overall, we note the very good agreement between the measurements, simulations, and theory. The slight discrepancies between the Chambers' model and the experimental results do not appear to have any correlations and are attributed to the instrumental jitter of the BPMs, RF power fluctuations, cavity alignment uncertainties, halo induced by non-ideal laser conditions. During the measurement, we were unable to set the phase of the CAV2 beyond the aforementioned range as it would require a significant reconfiguration of the

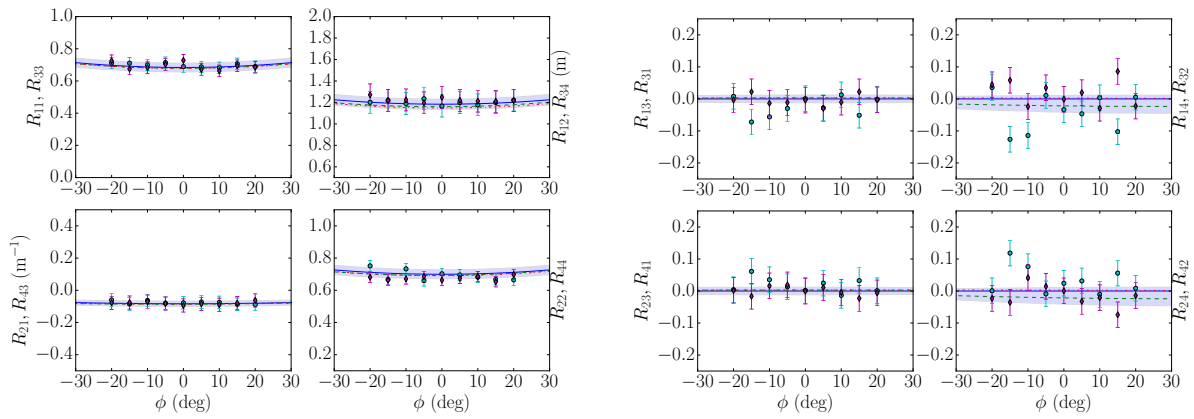

Figure 4.4: Diagonal (left four plots) and anti-diagonal (right four plots) blocks of the transport matrix. The solid (blue) lines represent Chambers' approximation, dashed (green/red) lines are obtained from 3D field map simulations for (x, x') and (y, y') planes respectively, circular markers and purple lozenges correspond to experimental values for (x, x') and (y, y') planes respectively. Shaded area represents matrix element variation due to RF calibration uncertainties (simulation).

IOTA/FAST beamline. Nevertheless we note that this range of phases is of interest to most of the project currently envisioned.

The elements of coupling (anti-diagonal) 2×2 blocks of the 4×4 matrix, modeled in the simulation are about one order of magnitude smaller than the elements of the diagonal block. For instance, considering the x coordinate we find that $R_{13}/R_{11} \sim O(10^{-2})$ and $R_{14}/R_{12} \sim O(10^{-2})$. This finding corroborates with our experimental results which indicate that $R_{13}/R_{11} \lesssim 0.1$ and $R_{14}/R_{12} \lesssim 0.1$; see Fig. 4.4. The latter observation confirms that, for the range of parameters being explored, the 3D effects associated to the presence of the couplers has small impact on the single-particle beam dynamics as already discussed in Sec. 2.1.1.1. The measured matrix elements were used to infer the determinant $|R|$ which is in overall good agreement with the simulation and Chambers' models; see Fig. 4.5.

Finally, the field amplitude in CAV1 was varied, thereby affecting the injection energy in CAV2 and the transfer matrix element of CAV2 measured. Since the beam remained relativistic the change did not affect the injection phase in CAV2. The resulting determinant

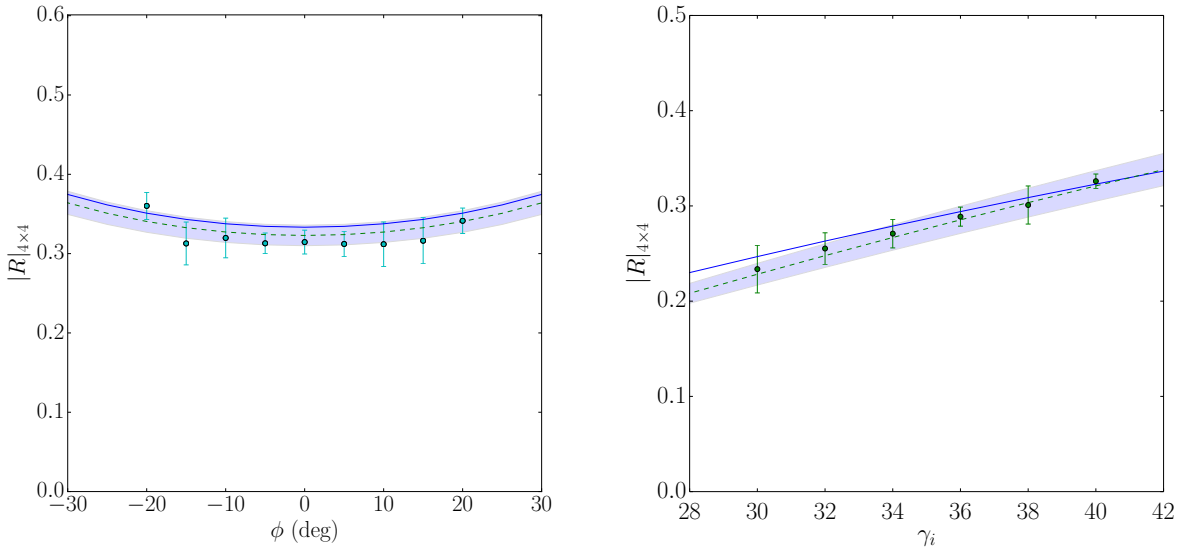

Figure 4.5: (left) Measured 4×4 transfer-matrix determinant (symbols) compared with the Chambers' approximation (solid line) and numerical simulations using the 3D field map (dashed line). The shaded area represents the uncertainty on the simulations due to RF calibration uncertainties. (right) Measured scaling for the 4×4 transfer matrix determinant as a function of injected-beam Lorentz factor γ_i (symbols) compared with the Chambers' approximation (solid line) and numerical simulations using the 3D field map (dashed line). The shaded area represents the uncertainty on the simulations due to RF calibration uncertainties.

(for the 2×2 matrix) is expected to follow an adiabatic scaling γ_i/γ_f. The experimental measurement presented in Fig. 4.5 confirm a scaling in $(\gamma_i/\gamma_f)^2$ as expected for the determinant of the 4×4 transfer matrix.

CHAPTER 5

CANONICAL ANGULAR MOMENTUM DOMINATED BEAMS AND FLAT BEAM GENERATION

In this Chapter we experimentally demonstrate CAM dominated electron beams generation and the process of CAM removal for flat beams generation. In addition, we study the propagation of the horizontal and vertical flat beams through the magnetic bunch compressor; this work was pioneered at Fermilab A0 facility [12, 13, 14, 89].

The IOTA/FAST RF-gun is capable of generating strong residual axial magnetic field at the photoemission location and therefore can produce CAM dominated or magnetized beams. Hereafter we consider the experimental beamline depicted in Fig. 2.1 with the nominal beam parameters provided by Tab. 2.1 and the beamline elements detailed in Tab. 2.2. During the FAST Run-2017 round of experiments CAM beams were produced using bucking solenoid as a source of the axial magnetic field. The main solenoid was used to match initial beam Twiss parameters into the round-to-flat beam (RTFB) adapter. The magnetic field at the cathode as a function of solenoids' currents is plotted in color in Fig. 5.1 (left). The maximum values of currents were limited by the corresponding beam dynamics downstream of the RF gun. The numerically simulated beam envelopes for the magnetized (dashed line) and flat beams (solid line) are presented in Fig. 5.1 (right).

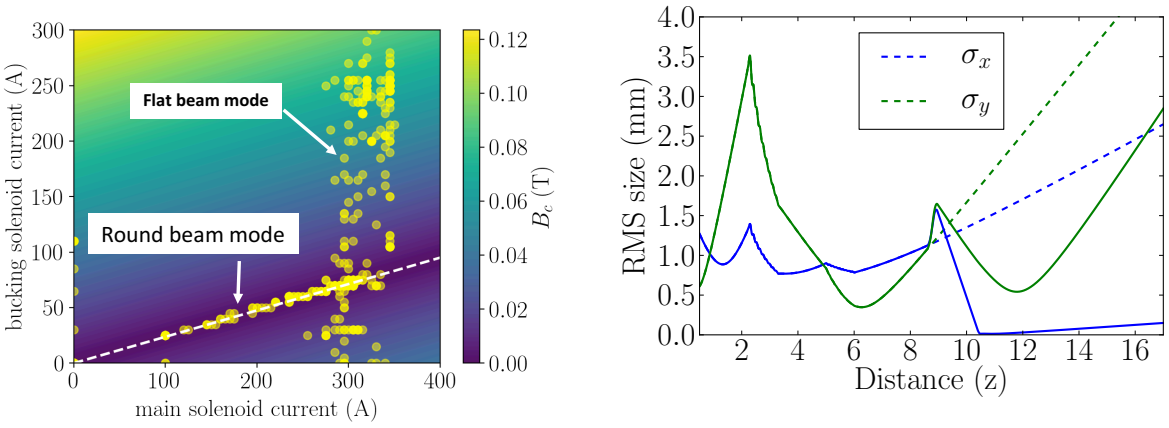

Figure 5.1: (left) Axial magnetic field at the photocathode as a function of bucking and main solenoids at FAST. (right) Corresponding beam dynamics for the case of B_{0z} = 734 Gauss tracked in IMPACT-T.

5.1 Magnetization measurement techniques

In order to perform the round-to-flat transformation described by Eq. (1.29) the first step is to measure the value of CAM provided to the electron beam. There are two methods for this measurement based on the fact that beam has a transverse rotational motion which results in xy-coupling. First method uses a varying quadrupole and infers the CAM from the change in values of second moments of the distribution. The second method is based on the intercepting multi-slit measurement. Additionally, the latter method can be extended to the case of multi-beam array discussed in Chapter 3.

5.1.1 Quadrupole scan technique

Consider the trace-space coordinate vector associated to a CAM beam at a location "0" downstream of the photocathode: $\mathbf{X_0} = (x_0, x_0', y_0, y_0')$. We are interested in measuring the mechanical angular momentum (MAM) $L \equiv \langle x_0 y_0' \rangle - \langle y_0 x_0' \rangle$ which is related to magnetization

introduced in Chapter 1 as $L = 2\mathcal{L}$. Let's characterize the beam distribution at the location "0" with covariance matrix given by Eq. (1.27), where $\langle x^2\rangle = \langle y^2\rangle = \sigma^2$, $\langle xy'\rangle = \langle y'x\rangle = L/2$ and $\langle x'y\rangle = \langle yx'\rangle = -L/2$. Note, that in case of a cylindrical-symmetric beam $\langle xx'\rangle = \langle yy'\rangle = \langle x'x\rangle = \langle y'y\rangle$ and $\langle x'^2\rangle = \langle y'^2\rangle = \sigma'^2$. Additionally, if the beam waist is located at "0", $\langle xx'\rangle = \langle yy'\rangle \equiv 0$. The directly measurable elements of the beam matrix (1.27) are: $\langle x^2\rangle, \langle y^2\rangle, \langle xy\rangle$ and the beam moments matrix is transformed as:

$$\mathbf{\Sigma_1} = \mathbf{R}\mathbf{\Sigma_0}\mathbf{R}^T, \tag{5.1}$$

where $\mathbf{R}$ is the linear transfer matrix. Consider a normal quadrupole placed at "0" followed by a drift space. The transfer matrices of a quadrupole and a drift under thin lens approximation are respectively given by Eqs. (1.21),(1.17), then the transformation of the $\mathbf{\Sigma_0}$ is

$$\mathbf{\Sigma_1} = \mathbf{R_{drift}}\mathbf{R_{quad}}\mathbf{\Sigma_0}(\mathbf{R_{drift}}\mathbf{R_{quad}})^T.$$

Under this transformation the measurable moments of the matrix are:

$$\begin{aligned} \langle x^2\rangle &= 2\langle xx'\rangle d(dq+1) + d^2\sigma'^2 + \sigma^2(dq+1)^2 \\ \langle y^2\rangle &= -2\langle yy'\rangle d(dq-1) + d^2\sigma'^2 + \sigma^2(dq-1)^2 \\ \langle xy\rangle &= Ld^2q. \end{aligned} \tag{5.2}$$

Thus, by measuring $\langle xy\rangle$ moment after the transformation one can infer the MAM as

$$L = \langle xy\rangle/d^2q. \tag{5.3}$$

Here q is the quadrupole strength and d is the drift length. Note, that in practice the calculation of the resulting moment $\langle xy\rangle$ in case of a small L can be altered by finite resolution

of the beam viewer setup. In that case, one can substitute Eq. (1.21) with Eq. (1.22) for the skew quadrupole, then measurable beam matrix elements are:

$$\begin{aligned} \langle x^2 \rangle &= d^2(-Lq + q^2\sigma^2 + \sigma'^2) + 2d\langle xx' \rangle + \sigma^2 \\ \langle y^2 \rangle &= d^2(Lq + q^2\sigma^2 + \sigma'^2) + 2d\langle yy' \rangle + \sigma^2 \\ \langle xy \rangle &= dq\left(d(\langle xx' \rangle + \langle yy' \rangle) + 2\sigma^2\right). \end{aligned} \tag{5.4}$$

Note, that under the assumptions made $|\langle x^2 \rangle - \langle y^2 \rangle| = 2d^2Lq$, or

$$L = |\langle x^2 \rangle - \langle y^2 \rangle|/2d^2q. \tag{5.5}$$

5.1.2 Multislits technique

Rotational motion induced by CAM can be also measured with a commonly used intercepting multi-slits mask. In this case, the mask with vertical or horizontal orientation will produce beamlets that will be titled at some location downstream of the mask. By computing the rotation angle between the mask and the viewer locations, one can infer the amount of mechanical angular momentum in the beam. In order to perform the calculation, the beam sizes at both locations have to registered. Then the multi-slit mask is inserted and the tilt angle θ is determined. The mechanical angular momentum L can then be deduced by a simple kinematic formula provided by Ref. [12]:

$$L = 2p_z\frac{\sigma_1\sigma_2\sin\theta}{D}, \tag{5.6}$$

where $\sigma_{1,2}$ are the measured beam sizes at the multi-slit mask and the screen location respectively, D is the drift length between the mask and the screen. We refer the reader to Refs. [12, 13] for a detailed description of the method.

The measurement process is demonstrated in Fig. 5.2 for different bucking solenoid currents. In the bucked configuration, the horizontal multislits at the X107 location are

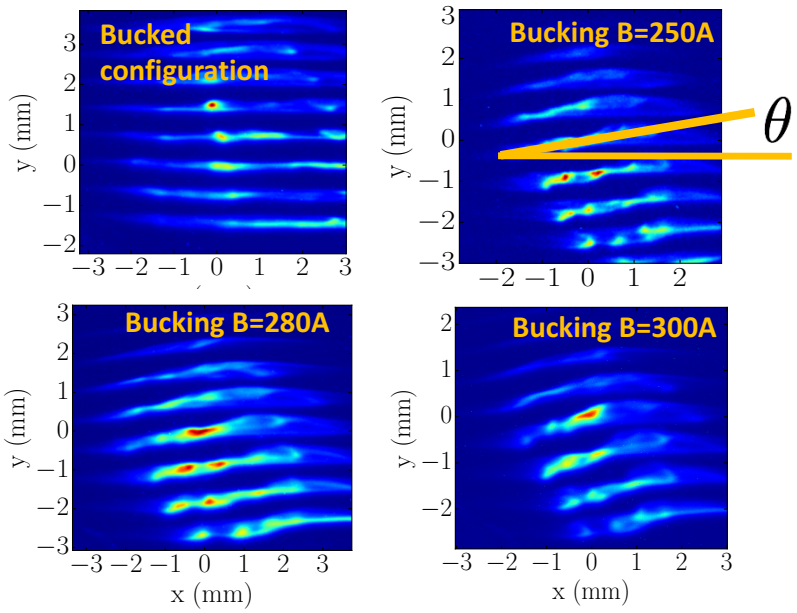

Figure 5.2: CAM value measurement using multi-slit mask at X107 location for different configurations of the FAST RF-gun solenoids.

seen to be horizontal downstream at the X111 screen. With the increase of the bucking solenoid current, the residual axial magnetic field at the photocathode increases, imposing the angular momentum on the beam. Latter results in the beamlets rotation, as depicted in Fig. 5.2.

5.1.3 Electron beam magnetization measurements at FAST facility

The CAM dominated 34 MeVelectron beam was formed with a laser distribution depicted in Fig. 5.3. The value of CAM was measured with both multi-slit and quadrupole scan methods and the results are in a good mutual agreement. After the CAM beam generation, the multi-slits were inserted at X107 location and the slit projections were recorded at X111 location. The magnetic field was reconstructed using the map depicted in Fig. 5.1 and the value of CAM using Eq. (5.6). The results shown in Fig. 5.4 (right) are in a good

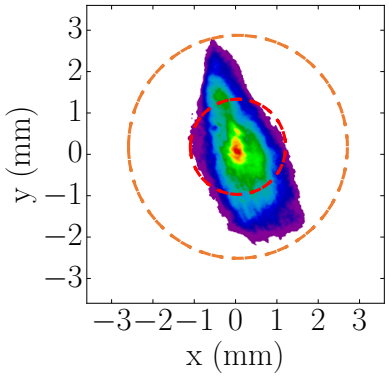

Figure 5.3: Initial asymmetric FAST photocathode laser distribution. The RMS sizes of orange and red circles are 950 μm and 520 μm respectively.

agreement with numerical simulations. For the flat beam generation experiment, we selected the bucking solenoid current of 255 A, which ensured stable machine operation and safe RF-gun vacuum levels. This corresponds to the maximum residual axial magnetic field applied on the cathode of 734 Gauss. Additionally, a quadrupole scan was performed for the selected machine configuration using Eq. (5.3), and the results are also in a good agreement with numerical simulations; see Fig. 5.4 (left). Both techniques were proved to be reliable and

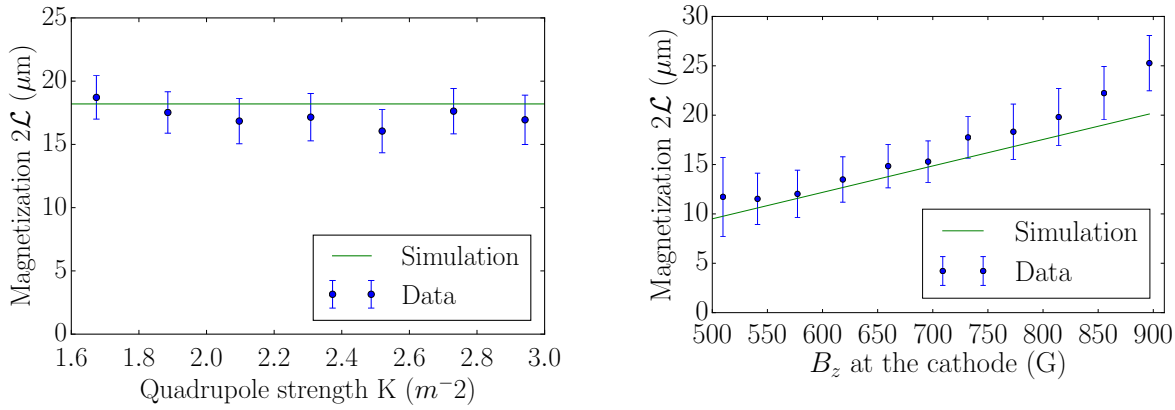

Figure 5.4: (left) Measured CAM using quadrupole scan method and comparison with IMPACT-T simulations. (right) measured CAM as a function of B_{0z} at the photocathode compared with IMPACT-T simulations.

fast for the CAM measurement and can be extended to the higher values of CAM in different experimental conditions.

5.1.4 Method to measure magnetization with MLA formed multi-beams

In this Section, we describe a possible application of the patterned electron beam formed by the MLA setup as a beam-based diagnostic tool for inferring the value of CAM.

We now consider the multi-beam laser distribution discussed in Section 3.3 projected onto a photocathode immersed in an axial magnetic field. The resulting electron beam, composed of multiple beamlets, will therefore undergo a similarity transformation (in the presence of a axisymmetric external focusing) of the form

$$\begin{pmatrix} x \\ y \end{pmatrix} = [k + R(\theta)] \begin{pmatrix} x_c \\ y_c \end{pmatrix}, \tag{5.7}$$

after exiting the magnetic-field region; see Fig. 5.5. In this equation the subscript $_c$ corresponds to the spatial coordinates on the cathode surface, k is a scalar and $R(\theta)$ is the 2×2 matrix associated to a rotation with angle θ. The measurement of the rotation angle and array size provides the value of mechanical angular momentum, similarly to Eq. (5.6):

$$L = \frac{p_z}{D}\left[\left(\frac{n}{2}a_1\right)\right]^2 (M \sin\theta), \tag{5.8}$$

where p_z is the axial momentum, n is a number of beamlets, a_1 is the separation between beamlets at the first viewer, and $M = a_2/a_1$ is the magnification factor between second and first viewer. Relating it to (1.26) one can infer the value of the magnetic field on the cathode B_{0z}.

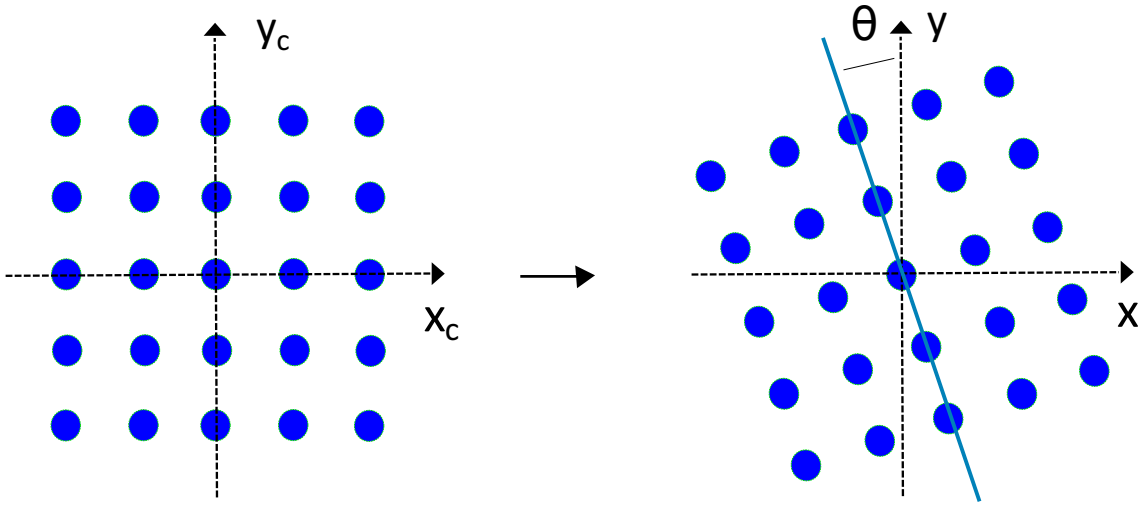

Figure 5.5: Illustration of the similarity transformation between the initial beamlet pattern emitted from the phtocathode (left) as it propagates to a downstream location (right). This schematics assumes the transverse momentum is solely angular in an axisymmetric external-focusing lattice.

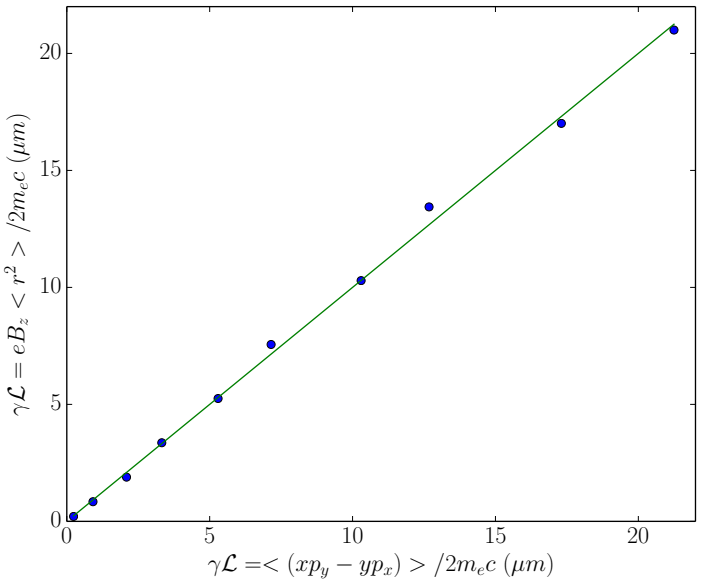

Figure 5.6: Demonstration of the method based on Eq. 5.8 using numerical simulations in IMPACT-T. The magnetization $\mathcal{L}$ is computed from the particle distribution (blue markers) and plotted against the magnetization inferred from the B_{0z} on the cathode surface. The green solid line correspond to the diagonal line.

To validate the proposed method via numerical simulations we used IMPACT-T and considered the AWA-WB beamline diagrammed in Fig. 2.7. Laser multi-beam array was converted into IMPACT-T particle distribution using the method described in Section 3.2. It was then propagated through the beamline and saved at two locations of YAG screens (YAG2 and YAG3 in Fig. 2.7) and away from the waist. The centroids of each beamlet were found and the mechanical angular momentum is inferred from Eq. (5.8). We performed numerical simulations for different B_{0z} field values and results are summarized in Fig. 5.6.

The latter Figure confirms that the CAM (as inferred from the value of B_{0z}) is fully transferred to the MAM. Some systematic discrepancies ($\langle 5\%$) are observed as $\mathcal{L}$ increases and most likely due to the contribution of nonlinear terms in multipole expansion of $B(z)$ not accounted for in Eq. 1.3 (which assumes a paraxial linear approximation).

The simulations demonstrate that illuminated cathode with a patterned laser beam provides a simple method to measure the MAM. It should be noted, that the fundamental systematic error may come from diagnostic cameras mutual misalignment. In a case of low $\mathcal{L}$, a longer distance between two screens has to be employed. Additionally, this technique provides an excellent determination of the magnetic axis and probes the laser spot alignment.

To extract the rotation angle and the beamlet separation, one can calculate beamlet positions using conventional 2D peak finding algorithm. However, this method becomes not very robust when the beamlet formation size at the location of the second screen is bigger than the screen size.

Another approach is to utilize projections $\langle \tilde{I}(k_x) \rangle$ and $\langle \tilde{I}(k_y) \rangle$ of the images in reciprocal Fourier space calculated via 2D fast Fourier transform (FFT). In this case, the tilt of the image will result in a difference between the locations of first harmonics; see Fig. 5.7. The tilt angle can be then computed as $\tan\theta = k_{x_1}/k_{y_1}$, where $k_{(x,y)_1}$ is the coordinate of the first-harmonic peak of the spatial bunching factor along the corresponding axis. Such an analysis assumes the beamlet-pattern periodicity along the two directions is identical (which is the case in our experiment). The full-width half-maximum (FWHM) sizes of the peaks in Fig. 5.7 are then accounted as errorbars of the measurement.

5.1.4.1 Proof-of-principle experiment at AWA facility

Proof-of-principle electron beam experiment was performed at AWA-WB beamline. A 12×12 laser beamlet pattern with rms duration of 6 ps was formed by using the technique from Section 3.3. In the experiment, the total charge was 60 pC per bunch, resulting in $\sim$ 420 fC per beamlet.

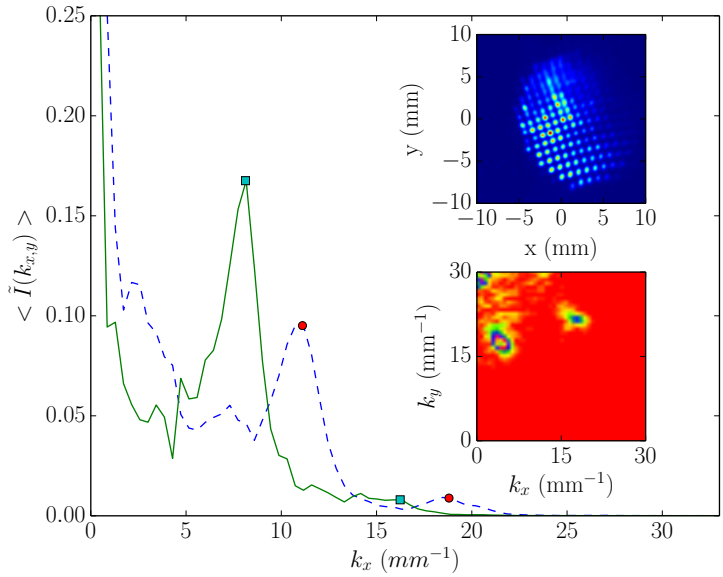

Figure 5.7: Bunching factor as function of horizontal k_x (solid trace) and vertical k_y (dashed trace) spatial frequency. The ratio of the lowest-frequency peaks k_{y1}/k_{x1} provides a measurement of the pattern rotation angle with respect to the horizontal axis. This data is extracted from the corresponding beam image (upper inset) and from projections of its 2D FFT image (lower inset).

The three solenoids depicted in Fig. 2.7 were controlled independently via unipolar power supplies. We started with the normal operational configuration where the bucking and focusing solenoids had opposite polarities which yields relatively low magnetization of the beam. The bucking solenoid current was slowly decreased to 0 A and the induced rotation of the beamlet formation was observed at YAG1 and YAG2 locations; see Fig. 5.8. Note, that initial pattern rotation in Fig. 5.8 for the case of $B_{0z} = 0$ is occuring due to Eq. (1.13). Then the polarity of the bucking and focusing solenoids was flipped and the bucking solenoid current was ramped up to -500A, applying the maximum achievable magnetic field at the photocathode. Total of 20 bucking solenoid current values were used to reach the maximum field at the cathode surface of $\simeq$ 1400 Gauss.

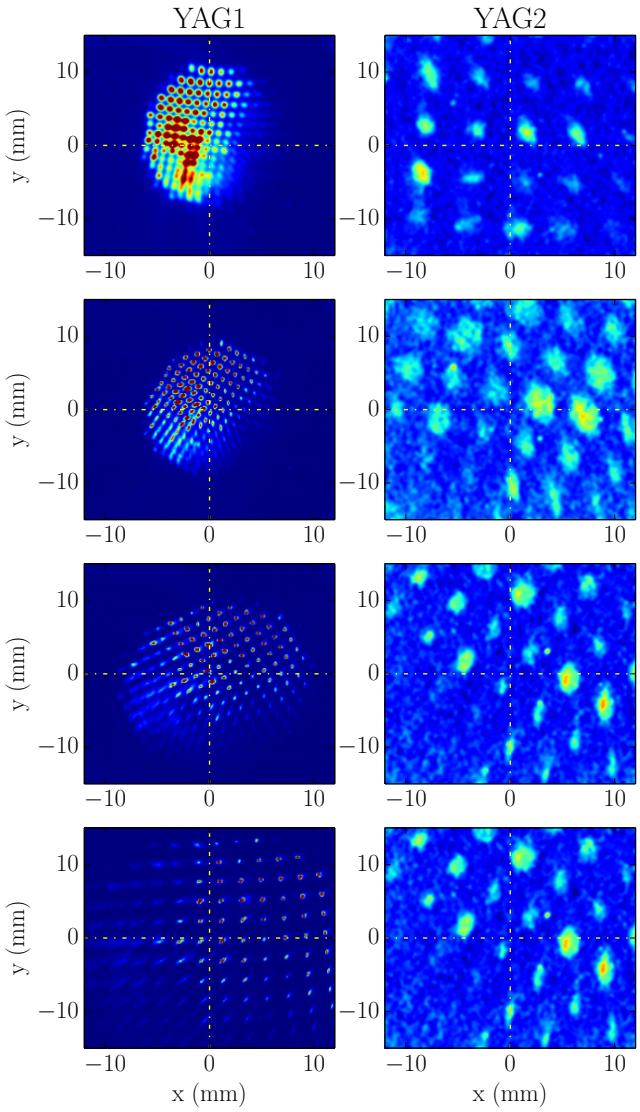

Figure 5.8: Beamlet-pattern distribution on YAG1 (left column) and YAG2 (right column) for different settings of the magnetic field on the photocathode B_{0z} = 0, 200, 500, 1000 Gauss (from top to bottom) at the AWA-WB beamline. The radial momentum yields to substantial magnification at YAG2 in addition to the rotation.

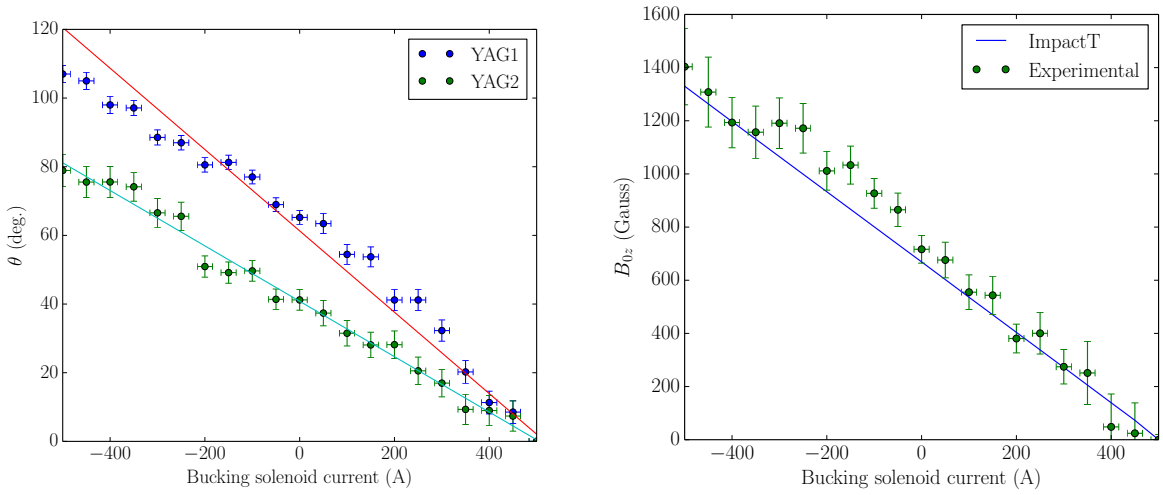

Figure 5.9: (left) Rotation angle of the beamlet pattern at screens YAG1 (left) and YAG2 (right) as a function of the bucking-solenoid magnetic field. The lines correspond to a linear regression of the experimental data. (Right) Comparison between IMPACT-T simulations (solid blue line) and experimentally recovered values of B_{0z} (symbols with error bars) from Fig. 5.8.

The beamlet pattern at the two screens YAG1 and YAG2 makes a different rotation angle. The rotation of the pattern between the two screens θ increases with the magnetization, as it can be seen in Fig. 5.9. In the latter picture the data point were obtained from the 2D FFT technique detailed in the previous Section. From the inferred rotation angle θ, the MAM was recovered via Eq. 5.8.

The retrieved value of the B_{0z}, the applied field on the cathode surface, computed using the data of Fig. 5.9 for different currents of the bucking solenoids are reported in Fig. 5.9. Specifically, the retrieved values are computed via $B_{z0} = \frac{2m_e c^2 L}{ec} r^2$ where L is found from Eq. 5.8. These values are in very good agreement with IMPACT-T simulations of the measurement which includes a model of the solenoids simulated with POISSON [90].

5.2 Electron beam simulations and flat beam generation

In order to investigate the mapping of the eigenemittances defined by Eq. (1.28) due to CAM, we first performed a numerical simulation of the RTFB transformation in IMPACT-T [22]. We converted a laser distribution at FAST photocathode into a macroparticle distribution similarly to Sec. 3.2.1. As displayed in Fig. 5.3 the initial laser distribution is asymmetric, therefore the axisymmetric flat beam solution given by Eq. (1.30) can only be a first order approximation. The correct settings of the RTFB adapter have to be found and optimized numerically. Note, that the solutions given by Eq. (1.30) will be identical for both orange and red circles in Fig. 5.3 and won't depend on the value of L. The particle distribution was generated with a value of CAM measured in Section 5.1.3 (see Fig. 5.4, left) and then propagated through the FAST low-energy beamline. The numerical beamline model included the RF gun phase, gradient, solenoids, booster cavities' phases and gradients values of the real machine. In case of a low beam charge (Q=20 pC), the three thick-lens RTFB adapter model was numerically optimized with the conjugate-gradient method using MAGNETOPTIMIZER [45]. The optimized quadrupole currents were then dialed back into the machine and the CAM removal process recorded at X111 location; see Tab. 2.2 for the beamline element references. The resulting comparison between experiment and simulations is presented in Fig. 5.10. One can see a good agreement between the numerically optimized solutions and the measured real beam distributions. The generated flat beam was propagated downstream of the RTFB adapter to ensure full transmission to the low energy adsorber. After the flat beam generation, the initial emittance measurement was performed with a quadrupole scan technique. The beam transverse distribution was registered at the X121 location as a function of quadrupole Q120 current. FAST beamline was implemented into ELEGANT tracking code and the function SDDSEMITMEAS was invoked to fit the beam

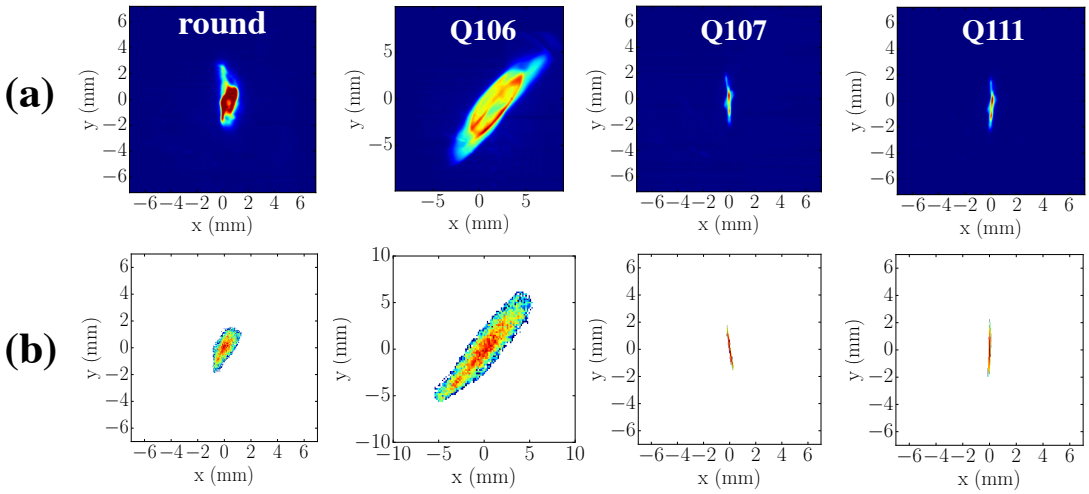

Figure 5.10: Demonstration of the CAM removal process in the experiment (a) and simulations (b) for the case of a vertical flat beam. The beam transverse distribution was recorded at X111 location. See Fig. 2.1 and Tab. 2.2 for the beamline details.

distribution emittances to the experimental data. For the details on beam image analysis procedure please see App. A.2. The initially recorded emittance values were not quite in agreement with the prediction given by Eq. 1.28, therefore we performed the optimization of the round-to-flat beam transformation.

5.2.1 Flat beam adapter optimization

In order to optimize the mapping of the eigenemittances onto resulting flat beam emittances, we developed a beam-based optimization tool using the pyACL framework [51]. In the optimization procedure, skew quadrupoles Q106, Q107 and Q111 were used as free variables, while all the quadrupole magnets downstream of the Q111 were turned off. We set

the ratio between beam transverse sizes at two locations (d_1, d_2) (corresponding to the screen X111/X121 positions) as a target function as:

$$\rho = \sqrt{\left(\frac{\sigma_{x,y}}{\sigma_{y,x}}\right)^2_{d_1} + \left(\frac{\sigma_{x,y}}{\sigma_{y,x}}\right)^2_{d_2}} = \sqrt{\left(\frac{\beta_{x,y}\epsilon_{x,y}}{\beta_{y,x}\epsilon_{y,x}}\right)^2_{d_1} + \left(\frac{\beta_{x,y}\epsilon_{x,y}}{\beta_{y,x}\epsilon_{y,x}}\right)^2_{d_2}}. \tag{5.9}$$

In Eq. (5.9), maximizing σ_x/σ_y means horizontal flat beam optimization and σ_y/σ_x corresponds to the case of vertical flat beam optimization. In this procedure, the optimizer will alternate between the two screens until the specified convergence threshold is reached. Note, that using two consequent locations effectively removes the dependancy from $\beta_{x,y}$ in Eq. (5.9) as betatron functions could only have one local minima in the free space, thus optimizing $\epsilon_{x,y}$. The method was found to be efficient and fast to optimize the flat beam

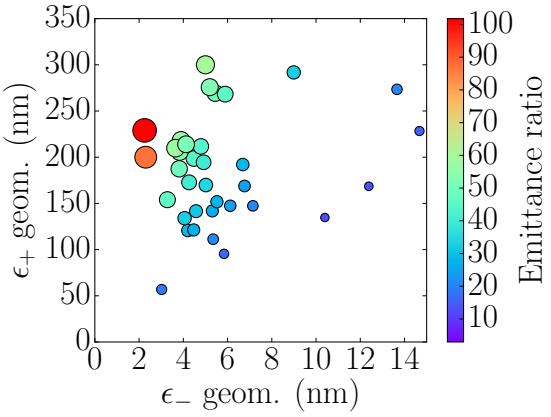

Figure 5.11: Demonstration of beam-based optimization of the eigenemittance mapping for the case of vertical/horizontal flat beam. The size (color) of the bubbles increases with the measured beam flatness ratio. Red bubbles correspond to the best emittance ratios obtained for horizontal/vertical flat beams.

emittances. However, the beam optics constraints and the screen resolution are the main limitations of this technique. In order to further optimize the resulting flat beam emittances, a direct single-shot emittance measurement is required, e.g. with an intercepting mask. The

performance of the beam-based flat beam optimizer is demonstrated in Fig. 5.11 and the resulting beam images are presented in Fig. 5.12.

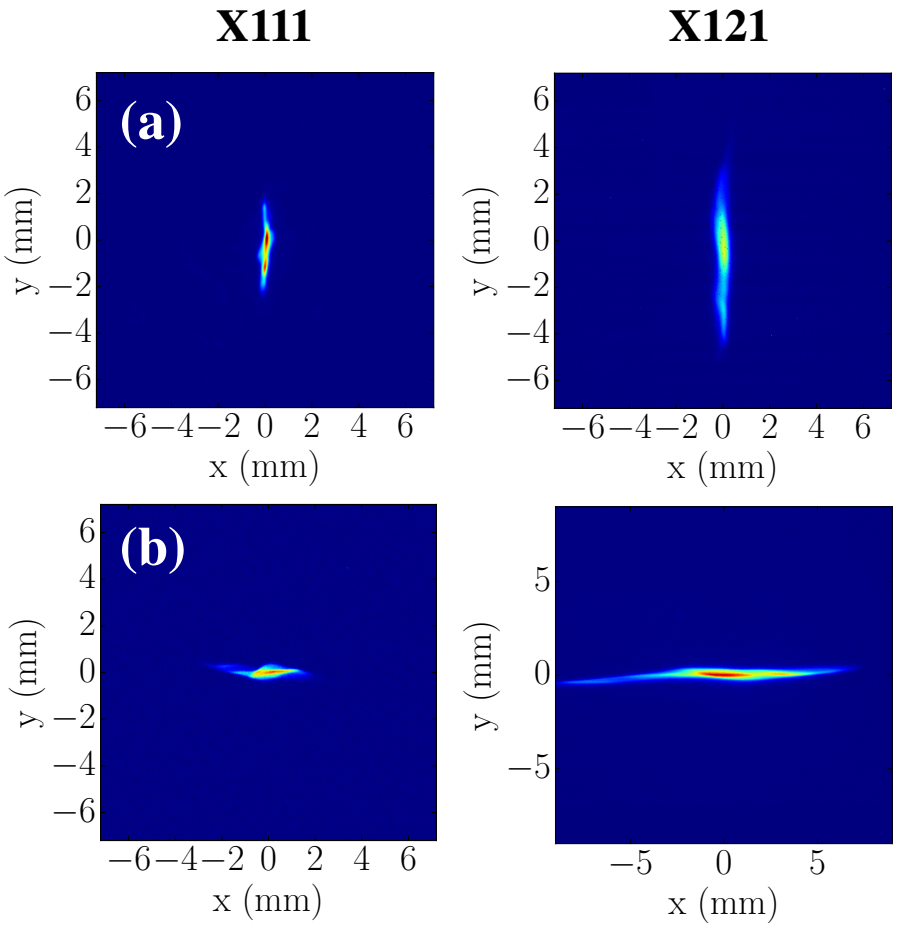

Figure 5.12: Measured optimized vertical and horizontal flat beams produced from the beam with CAM due to the residual magnetic field of 734 Gauss at the photocathode.

5.2.2 Flat beam emittance measurement

The final emittance measurement after the RTFB adapter optimization was performed using a quadrupole scan technique. The resulting flat beam normalized emittances generated

from the beam with CAM of approximately $L = 18$ μm were measured to be: $\epsilon_x = 0.13$ μm, $\epsilon_y = 14.4$ μm for the vertical flat beam and $\epsilon_x = 0.17$ μm, $\epsilon_y = 12.7$ μm for the horizontal flat beam. The beam images for the aforementioned cases are depicted in Fig. 5.12 and the emittance measurements are summarized in Tab. 5.1.

Table 5.1: Resulting measured emittances for the cases of vertical and horizontal round-to-flat beam transformation compared with numerical simulations in IMPACT-T.

Experimental results			
Norm. emit.	Vert. fb	Hor. fb	Units
ϵ_x	0.13 ± 0.03	12.7 ± 2.79	μm
ϵ_y	14.4 ± 3.17	0.17 ± 0.04	μm
ϵ_{4D}	1.37 ± 0.42	1.47 ± 0.49	μm
IMPACT-T simulations			
ϵ_x	0.08	17.7	μm
ϵ_y	18.0	0.10	μm
ϵ_{4D}	1.20	1.33	μm

The numerical simulations of the RTFB transform in IMPACT-T for the best possible flatness indicate a good agreement with the measured upper emittance, while the lower geometric emittance is found to be $\epsilon_- = 0.015$ μm for the case of vertical and $\epsilon_- = 0.018$ μm for the case of horizontal flat beams. The discrepancy between the simulations and measurement is attributed to a few factors. First, the quadrupole scan technique is limited by a finite pixel size of the YAG viewer which in case of FAST beamline corresponds to σ_{res} =9 μm. Measuring extremely low emittances with the quadrupole scan requires longer baselines and optics adjustment. In the case of a flat beam, the high emittance asymmetry is a limitation to both of these requirements. Second, the RTFB transformer optimization routine based on quadrupole scan is not exact and has to be improved with a direct emittance measurement. Additionally, a fourth quadrupole in the RTFB adapter would improve the flat beam solution stability. The numerical simulations indicate a dependancy of the flat beam

emittances from the phases of the booster cavities [89]. Due to RF-uncertainty of about 1 MV/m in both booster cavities, the degree of freedom associated with the minimizing of the energy spread was not available for a fine optimization. All aforementioned limitations impact the measured value of the RMS beam size σ_{mes} as [13]:

$$\sigma_{mes} = \sqrt{\sigma_0^2 + \sigma_{res}^2 + (\eta\delta)^2},$$

where σ_0 is the real RMS beam size, η is the RTFB adapter dispersion and δ is the energy spread. The error in measured σ_{mes}, in turn, propagates to the resulting emittance value. Last but not least, the simulated best flat beam emittances correspond to the emittance ratio of about 1000 which was proved to be very difficult to achieve in the real beamline [14].

5.3 Flat beam compression in the chicane

Transverse and longitudinal beam dynamics of a flat beam in the FAST chicane was numerically investigated in great detail in [89]. In brief, a transverse emittance growth is expected during the flat beam compression in the chicane due to space-charge and coherent synchrotron radiation (CSR) effects in chicane doglegs; see Fig. 1.2. It was found that the emittance growth occurs mostly when the bunch length is the shortest, and additionally horizontal emittance growth was much larger than vertical [91]. The final emittance degradation associated to the induced energy spread over one dipole magnet in the bending plane is given by [92, 93]:

$$\epsilon_{x,f} \approx \sqrt{\epsilon_{x,i}^2 + \epsilon_{x,i}\beta_{x,f}\langle\Delta x'^2\rangle}, \tag{5.10}$$

where $\epsilon_{x,f}$ is the final emittance, $\epsilon_{x,i}$ is the initial emittance, $\beta_{x,f}$ is the betatron function at the end of the bunch compressor and $\Delta x' \approx \theta\delta/2E$. In the latter expression δ corresponds to

the energy spread induced by the CSR effects, θ = 18 degrees for FAST bunch compressor and E is the total energy of the electron beam. When the value of $\epsilon_{x,i}$ is large, the resulting emittance is mostly unaffected by the CSR induced angular spread. Thus, in case of a horizontal flat beam, since the emittance in the bending plane is $\epsilon_x \gg \epsilon_y$, therefore making the beam not succeptable to the emittance growth in that plane during compression. This fact also implies that the total ϵ_{4D} will be less degraded after the bunch compressor, making the application of flat beams beneficial to for the beam transport of short bunches.

A numerical model for FAST beamline with chicane parameters presented in Tab. 2.1 was implemented in the IMPACT-T code. The simulations included space-charge forces and one-dimensional CSR effects when particles were propagated through the chicane. In order to introduce the energy spread required for bunch compression (see Sec. 1.5), the second cavity was run off-crest. The maximum compression in the FAST beamline corresponds to the second booster cavity phase to be -30 degrees off-crest, and maximum decompression is achieved when it is +30 degrees off-crest. Numerical model also included the experimental RTFB adapter settings. The resulting lower emittance ϵ_- as a function of second booster cavity phase is plotted in Fig. 5.13. As expected, when ϵ_- is mapped onto horizontal plane, it is significantly degraded after the maximum compression (factor of 6 growth). Additionally, when ϵ_- is mapped onto vertical plane, the emittance dilution for the maximum compression is about factor of 1.75 due to the large value of ϵ_+ in the horizontal plane. It has been shown via numerical simulations that the emittance growth in the latter case can be further mitigated by adjusting the beam focusing in the chicane [89].

The experimentally measured compressed vertical and horizontal emittances are presented in Fig. 5.13. The emittance growth is an excellent agreement with the previous experimental conclusions and numerical simulations for both cases of round and flat beam [91, 89]. In the case of a maximally compressed vertical flat beam, the lower emittance growth is about factor of 4. For the maximally compressed horizontal flat beam the emit-

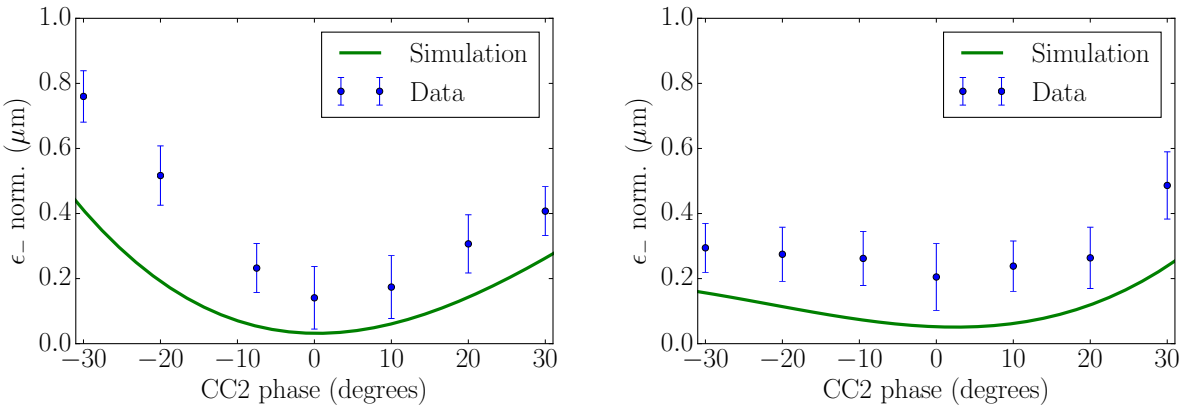

Figure 5.13: Compressed vertical (left) and horizontal (right) flat beam lower emittances measured as a function of the second booster cavity phase compared with IMPACT-T simulations.

tance dilution is only factor of 1.5, which is consistent with IMPACT-T simulations. Figure

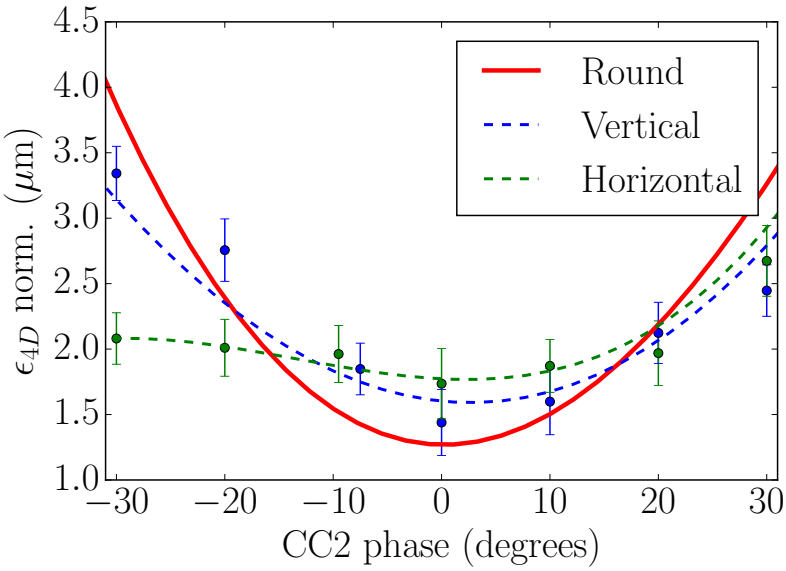

Figure 5.14: Measured ϵ_{4D} as a function of second booster cavity phase for both vertical and horizontal flat beams. Solid line corresponds to the simulated case of a round non-magnetized beam of the same RMS size at the photocathode. Dashed lines are drawn for reference.

5.13 shows the resulting comparison between measured experimental values and simulations.

The dilution of the upper emittance ϵ_+ in both horizontal and vertical flat beam cases measured to be much less significant (about 15% in case of maximum compression), which is within the estimated error bar for all the measurements. In Fig. 5.14 total ϵ_{4D} growth for flat beam compression is compared to the case of a round beam of the same charge and size at the photocathode. Vertical flat beam does not present a significant improvement in ϵ_{4D} preservation, while horizontal flat beam demonstrates factor of 2 improvement in ϵ_{4D} dilution.

In conclusion, an experimental setup with a CAM beam transformed into a compressed horizontal flat beam can be considered for future operations where the preservation of the total ϵ_{4D} is critical. At FAST, such a setup can lead to a better quality beam to be delivered to the high-energy beamline and IOTA ring. Additionally, a reverse flat-to-round tranformation can be performed after propagating through the bunch compressor. This technique can serve as a method of transporting and manipulating CAM beams in the accelerator.

CHAPTER 6

BUNCH SHAPING IN LONGITUDINAL SPACE-CHARGE AMPLIFIER (LSCA)

Longitudinal-space-charge-driven micro-bunching instabilities arising in bunch compressors were predicted and observed over the last decade [94, 95, 96]. It was recently proposed to employ such micro-bunching instability mechanism to form attosecond structures on the bunch current distribution for the subsequent generation of cohrent radiation pulses [97].

A possible beam line configuration capable of enabling the micro-bunching instability is relatively simple. It essentially consists of focusing sections where energy modulations due to the longitudinal space-charge (LSC) impedance accumulate, followed by a longitudinally-dispersive section. The latter section, by introducing an energy dependent path length, converts the incoming energy modulation into a density modulation. Such an elementary cell is often referred to as a LSC amplifier (LSCA). Most of the beamlines studied so far consider a longitudinally-dispersive section arranged as a bunch compression chicane; see Fig. 6.1. Several of these LSCA modules are concatenated to result in a large final density modulation. We further assume the compression process in the chicane is linear [the incoming longitudinal phase space (LPS) does not have any nonlinear correlations]. Such a modulated beam, when participating in a radiation-generation process, can produce coherent radiation at wavelengths comparable to the spectral range of the final density modulations.

We first introduce a fully three dimensional (3D) multi-scale space-charge algorithm adapted from Astrophysics [82]. The algorithm is used to discuss some limitations of the one-dimensional LSC impedance model commonly employed in LSCA investigations. Using the

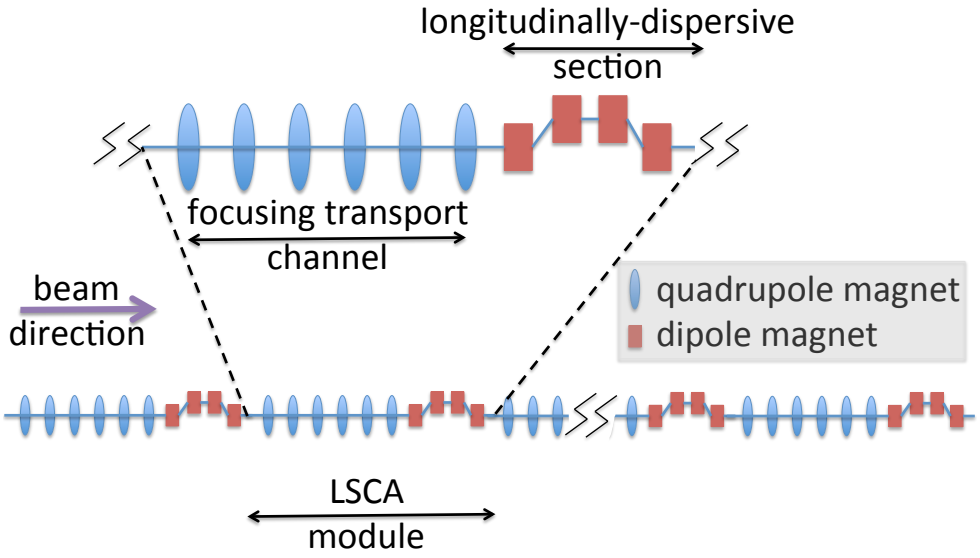

Figure 6.1: Overview of a cascaded longitudinal-space-charge amplifier (LSCA) composed of several LSCA modules. Each LSCA module incorporate a focusing channel and a longitudinally dispersive section. The (red) rectangles and (blue) ellipses respectively represent dipole and quadrupole magnets.

latter benchmarked algorithm, we then investigate a possible LSCA beamline configuration similar to the one studied in [97]. Finally, we estimate the generation of undulator radiation seeded by the LCSA. In contrast to Ref. [97], our study considers the case of a 300-MeV electron beam produced in a conventional superconducting linac, e.g. FAST injector.

6.1 Mechanism for longitudinal space charge amplifiers

Charged-particle beams are subject to self interaction via velocity and radiation fields. In absence of radiation processes (i.e. acceleration), the effect of velocity fields (i.e. space charge) dominates and its regime varies with the bunch density. Under a simple 1D approximation, a comparison of the Debye length λ_D to the root-mean-squared (rms) transverse beam size $\sigma_\perp$ and mean inter-particle distance $\Lambda_p \simeq n_e^{-1/3}$ (where n_e is the electronic density)

provides a criterion to assess the importance of space charge effects on the beam dynamics. When $\sigma_\perp < \lambda_D$ space charge effects are significant and often computed using the mean-field approximation (i.e. the space charge force is derived from the electrostatic potential associated to the particle distribution) commonly implemented in particle-in-cell (PIC) algorithms. However, when $\lambda_D < \Lambda_p$, particle-to-particle "binary" interactions play an important role and are needed to be accounted for [17].

As the beam is accelerated the transverse and longitudinal space-charge forces reduce respectively as $O(1/\gamma^2)$ and $O(1/\gamma^3)$ where γ is the Lorentz factor. At the macroscopic level, e.g. for spatial scale comparable to the bunch sizes, the space charge can be accurately described by a mean field approach [98]. However, in high-brightness beams – beams with low fractional momentum spread – the weakened longitudinal-space charge (LSC) force can still influence the beam dynamics at a microscopic level – i.e. for spatial scales smaller than the bunch sizes – and small density modulations (e.g. due to noise or imperfections) can result in LCS-driven energy modulations. In this latter regime, the LSC is generally treated with a one-dimensional (1D) model.

To illustrate the main results of the 1-D model, we consider a simple beam line consisting of a drift with length L_d (where the beam is transversely contained) followed by a chicane with longitudinal dispersion R_{56}. It is customary to characterize the strength of the micro-bunching instability by associating the density gain defined as

$$G(k) = \frac{b_i(k)}{b_f(k)}, \tag{6.1}$$

where $k \equiv \frac{2\pi}{\lambda}$ and λ is the observation wavelength and $b_{i,f}$ are respectively the initial and final bunching factors defined in Eq. (1.5). The gain for this simple beam line can be shown to be proportional to the impedance $Z(k,r)$ [99] following

$$G = Ck|R_{56}|\frac{I}{\gamma I_A}\frac{4\pi L_d|Z(k,r)|}{Z_0}e^{-\frac{1}{2}C^2k^2R_{56}^2\sigma_\delta^2}, \tag{6.2}$$

where $I_A = 17$ kA is the Alfvèn current, σ_δ is the rms fractional energy spread, C is the energy chirp defined in Sec. 1.5, and $Z_0 \equiv 120\pi$ is the free-space impedance.

The exponential term in Eq. 6.2 induces a high-frequency cut-off of the modulation

$$R_{56} \approx -\frac{c}{\omega\sigma_\delta}. \tag{6.3}$$

Note, that after traveling through a BC, the modulation wavelength will be shortened by a compression factor $\kappa \equiv (1+R_{56}C)$. Although the impedance $Z(k,r)$ is partially determined by the properties of the wakefields inside the BC [99], the LSC has much stronger effect in amplifying density modulations [97, 100]. For a transversely Gaussian cylindrically-symmetric beam the LSC impedance is given by [101]

$$Z(k) = -i\frac{Z_0}{\pi\gamma\sigma_\perp}\frac{\xi_{\sigma_\perp}}{4}e^{\xi_{\sigma_\perp}^2/2}\mathrm{Ei}(-\frac{\xi_{\sigma_\perp}^2}{2}), \tag{6.4}$$

where $Z_0 = 120\pi$ is the free-space impedance, $\mathrm{Ei}(x) \equiv -\int_{-x}^{\infty} dte^{-t}/t$, $\sigma_\perp$ is the rms beam size and $\xi_{\sigma_\perp} \equiv k\sigma_\perp/\gamma$. Similar expression for a transversely uniform beam is provided in [102].

The maximum of the Eq. 6.4 is achieved at $\xi_{\sigma_\perp} \approx 1$, therefore the optimal wavelength of the density modulation will be located around

$$\lambda_{opt} = 2\pi\sigma_\perp/\gamma. \tag{6.5}$$

6.2 Simulation procedure and benchmarking

The nature of space charge forces lies in particle-to-particle Coulomb interaction. Direct summation of the forces yields to $O(N^2)$ growth where N is the number of macroparticles, which makes it impossible to compute at large N. Several approximation techniques can be used: mean-field on a grid approximation [21], one-dimensional space charge impedance [101], analytical sub-beams or ensembles model [103], rigid-slice approximation [98]. All of those methods reduce the problem's complexity via some approximations which ultimately limits the maximum attainable spatial resolution. Most recent attempt used a three-dimensional-grid space charge algorithm based on a periodic boundary [97].

From another point of view, space charge problem is very similar to the well-known N-body problem in celestial mechanics. One of the most effective algorithms for the gravitational N-body problem is the so called "tree" or Barnes-Hut (BH) algorithm [82], which scales as $O(N \log N)$. In this section we present the results obtained using a modified version of the code available at [104]. Such approach was successfully employed to simulate early beam dynamics in photocathode and laser ion cooling [83, 105].

In brief the BH algorithm initially embraces the bunch distribution in a cubic cell called a root cell. The root cell is divided into 8 sub-cells recursively, until it reaches the point where a single sub-cell contains just one particle. Then forces only between nearby cells are calculated directly, and the cells far away from each other are treated as two large macroparticles with the total charge placed in the cell's center of mass. The process of calculating net forces starts from the root cell and recursively parses the cell hierarchy until reaches the size of the smallest cell that is predefined as a precision parameter. Thus, the algorithm is significantly faster than a direct summation method. BH method in particle tracking, however, does not preserve full Hamiltonian, yet for relatively small precision parameter the difference between

direct summation is comparably small [82]. Note, that direct summation part of the BH algorithm also requires potential smoothing to avoid singularities.

Another more efficient Fast Multipole Method (FMM) algorithm has been recently developed [106, 107] and will be eventually used in further refinement of our work. Though FMM algorithms are more sophisticated and precise, still BH method is comparably accurate and faster than FMM and it can be embedded in time-stepping integrators [108].

For the studies we used the BH algorithm as an external script within the ELEGANT simulations. At a user-specified axial locations along the accelerator beam line, space charge kicks were applied. Our approach is to follow the quasi-static approximation [109]. The distribution at the defined axial location is recorded and a Lorentz transformation to the bunch's rest frame is performed. The BH algorithm is then utilized to obtain the 3D electrostatic field $\mathbf{E}'$ in the bunch's rest frame. We should point out that the BH algorithm returns the field directly evaluated at each macro-paticle locations (so that there is not need for interpolation as in a grid-based algorithm). The electrostatic field is subsequently transformed in the laboratory frame via a Lorentz boost. The resulting electromagnetic fields $(\mathbf{E}, \mathbf{B})$ in the laboratory frame are used to apply the corresponding Lorentz force $\mathbf{F} = q[\mathbf{E} + c\boldsymbol{\beta} \times \mathbf{B}]$ on each of the macroparticles [q and $\boldsymbol{\beta}$ are respectively the charge and reduced velocity ($\beta \equiv \sqrt{1 - \gamma^{-2}}$) of the considered macroparticle].

The distribution is finally passed back to ELEGANT and tracked up in the given optical lattice to the next space charge kick where the above process repeats. We henceforth refer to the combination of the BH algorithm with ELEGANT as "ELEGANT-BH".

Our implementation relies on an impulse approximation so that only the momentum, i.e. not the position, of the macroparticles is altered by the space charge kick. We assumed there is no magnetic field in the rest frame. Although this assumption is not strictly valid, it was shown to hold for beams with low energy spread typically generated from photoinjectors [110].

In order to gain confidence in the implemented space charge calculation procedure, several validation tests were conducted; see A.1. In this section we only focus on the benchmarking of Eq. 6.4 with ELEGANT-BH. We considered initial bunch distributions with modulated current profiles of the form

$$f(\mathbf{x}) \quad = \quad T(x,y)L(z)\,[1 + m\cos kz], \tag{6.6}$$

where $\mathbf{x} \equiv (x, y, z)$, m and k are respectively the modulation amplitude and spatial wavenumber, and $L(z)$ and $T(x, y)$ are respectively the nominal longitudinal and transverse beam distributions.

The modulation along the axial z direction leads to an energy modulation due to the LSC impedance and eventually produces further current modulation depending on the longitudinal dispersion of the beamline. From the definition of the impedance, and given the Fourier-transformed longitudinal electric field $\widetilde{E}_z(k)$ and current distribution $\widetilde{I}(k)$, the longitudinal impedance can be recovered as

$$Z(k) = -\frac{\widetilde{E}_z(k)}{\widetilde{I}(k)}. \tag{6.7}$$

A comparison of the simulated LPS (after one space charge kick with ELEGANT-BH) with the initial one appears in Fig. 6.2(a,b) and demonstrates the salient features of the modulations and especially the $\pi/2$ shift between the final energy modulations and the initial density modulations; see Fig. 6.2(c).

The Fourier transform of the initial current distribution was performed using a fast-Fourier transform (FFT) algorithm. Likewise, the mean energy of thin axial slices within the final LPS density distribution was computed thereby providing the energy modulation dependence on z, $\Delta\mathcal{E}_z(z)$. The extracted energy modulation $\Delta\mathcal{E}_z(z)$ is Fourier transformed to

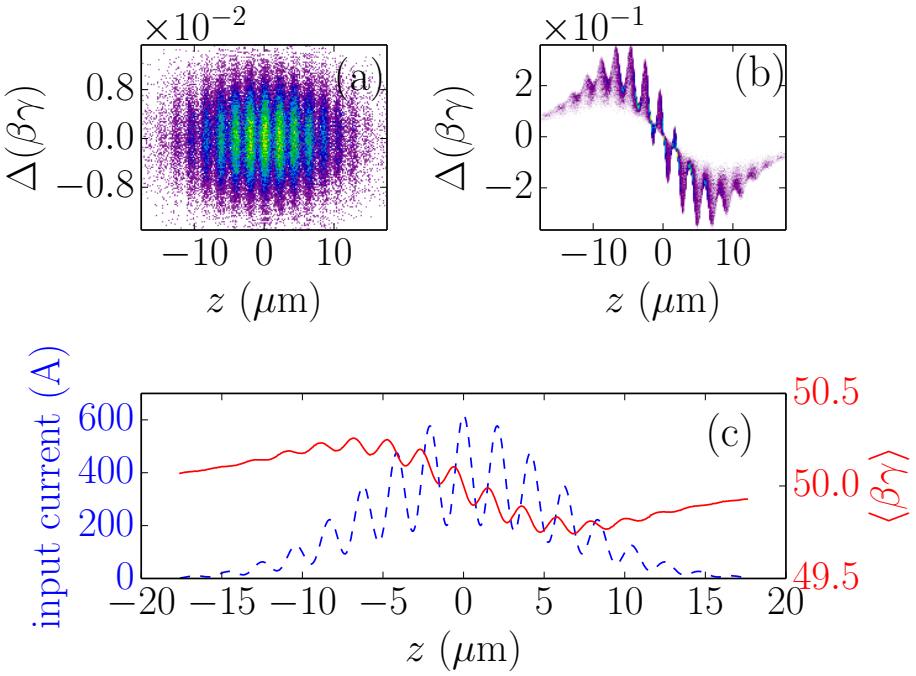

Figure 6.2: LPS distribution for a density-modulated Gaussian beam before (a) and after (b) the application of one space charge kick. Corresponding induced energy modulation (red solid trace) computed from image (b) and current distribution (blue dash trace) obtained from image (a); lower plot (c).In the upper images $\Delta(\beta\gamma)$ refers to the normalized momentum spread.

yield $\Delta\widetilde{\mathcal{E}}_z(k)$ from which the axial electric field $E_z(k)$ was inferred. The resulting impedance evolution as a function of k obtained is compared against Eq. 6.7 in Fig. 6.3. The studies were carried out using different number of macroparticles ($N = [1, 2, 5, 10] \times 10^6$) to ensure the convergence and satisfy the statistical limit [111, 112]. The number of FFT bins n_b was also tuned to minimize discretization effects while varying k. As the wavenumber k value decreases, the bunch duration length was increased to ensure the number of macroparticles per bin remains constant and guarantees a sufficient number of modulations occurs within the bunch. In our simulations we set this ratio to be typically $N/n_b \approx 5000$. Figure 6.3 points to small differences between the `LSCdrift` element in ELEGANT that assumes transverse

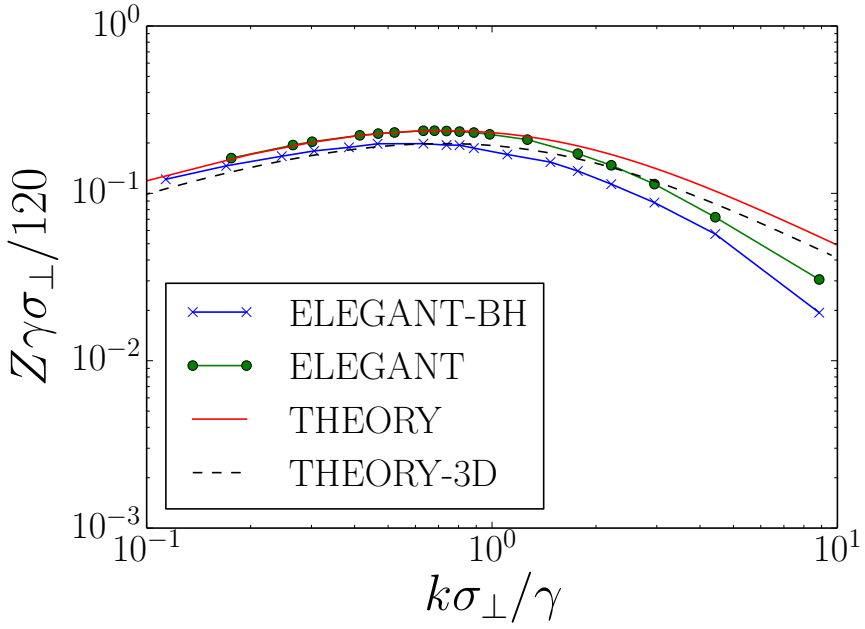

Figure 6.3: Comparison of the longitudinal space-charge impedance computed from Eq. 6.4 ("THEORY"), from Eq. 6.8) ("THEORY-3D"), with the ones retrieved from simulation with ELEGANT built-in `LSCdrift` element ("ELEGANT"), and ELEGANT-BH ("ELEGANT-BH").

distribution to be uniform [23, 102] and Eq. 6.4. The ELEGANT-BH performs full three-dimensional space charge force calculation and therefore inherits both the transverse and longitudinal effects in LSC impedance. Such effects were previously recognized [113] and are attributed to the radial dependence of the axial space charge field conferring a similar dependence on the impedance. To further explore longitudinal space charge impedance radial dependence we performed an analysis over thin radial slices $[r, r+\delta r]$ where $\delta r = 0.05 r_0$. The results of such an analysis are summarized in Figs. 6.3, 6.4 for a beam following a transerse

Gaussian distribution of the form $f(r) \propto \exp[-r^2/(2r_0^2)]$. Figure 6.3 compares the numerical results with the expected radial dependence analytically derived in Ref. [113][1]

$$\begin{aligned} Z(k,r) &= \frac{4\pi k}{\gamma^2}\int f(r')r'dr'\,[(\theta(r-r') \\ &\quad \times K_0(\frac{kr}{\gamma})I_0(\frac{kr'}{\gamma}) + \\ &\quad +\theta(r'-r)K_0(\frac{kr'}{\gamma})I_0(\frac{kr}{\gamma})\Big)\Big], \end{aligned} \tag{6.8}$$

where $\theta(r)$ is the Heaviside step function, K_0 and I_0 are modified Bessel functions, $f(r)$ is the distribution function. A noteworthy consequence of the observed strong radial dependence for a Gaussian transverse distribution is the effective smearing of the axial modulation which will effectively result in weaker integrated energy modulations.

As a final note, we point out that in the case of a parabolic $f(r) = f_0(a^2 - r^2)\theta(r-a)$ and uniform $f(r) = f_0\theta(r-a)$ distribution an analytical form of the impedance can be retrieved [here a, f_0, and $\theta(r)$ are respectively the radius, normalization factor, and Heaviside function]. It is especially found that the parabolic transverse distribution yields an impedance with weaker dependence on the radius compared to a Gaussian transverse distribution; see Fig. 6.4. These observations suggest a possible use of transverse electron-beam shaping [114, 115] as ways of controlling the micro-bunching instability.

6.3 LSCA simulations for FAST facility

In this Section we explore the possible use of a staged LSCA beam line to produce micro-bunching structure with spatial scale corresponding to the ultraviolet regime, so $\lambda < 400$ nm. For our simulations we considered the configuration available at the FAST facility; see

[1] We started with the Green's function for a δ ring derived as Eq. (35) of Ref. [113] and applied the Bessel recursive relation to further simplify it. In addition we explicitly wrote the $\mathbf{dr'}$ of Ref. [113] as $2\pi r'dr'$.

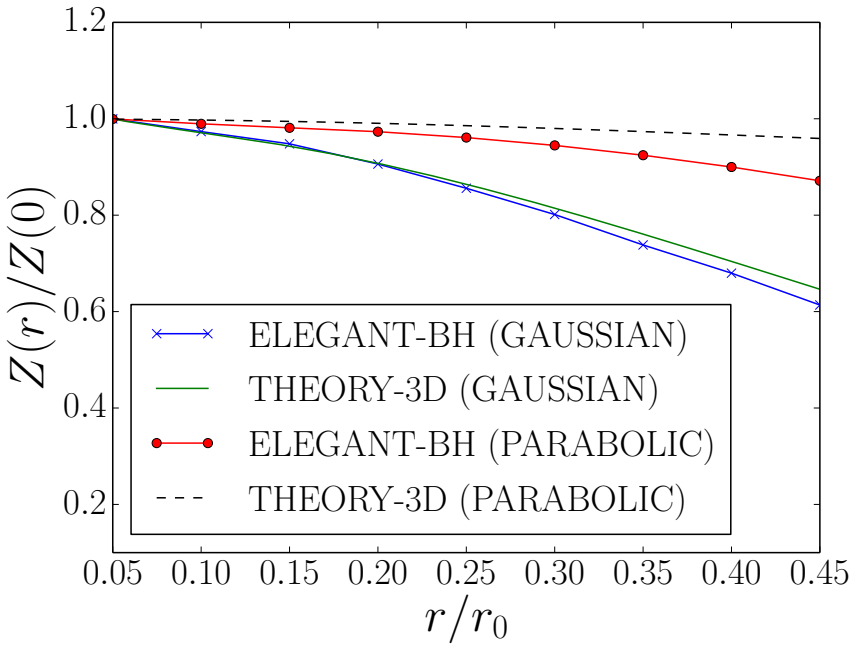

Figure 6.4: Radial dependence of $Z(r)$ for a fixed value of k. The green and blue traces respectively correspond to the impedance with Gaussian transverse distribution from Eq. 6.8 and ELEGANT-BH. The parameter r_0 is the rms transverse size of the distribution.

Fig. 2.1. We ammend the existing beamline with the possible LSCA setup diagrammed in Fig. 6.5. Conversely a ~ 70 m transport beamline downstream of the cryomodule, with proper optics, could accommodate the formation of broadband density modulation with UV spectral content; see Fig. 6.5.

6.3.1 Initial beam parameters and LSCA beamline configuration

A numerical optimization of the electron-beam formation and acceleration to ~ 50 MeV was carried out with ASTRA for various charges [48]. The results combined with a mild bunch compression in the 50-MeV bunch compressor chicane, could produce bunches with

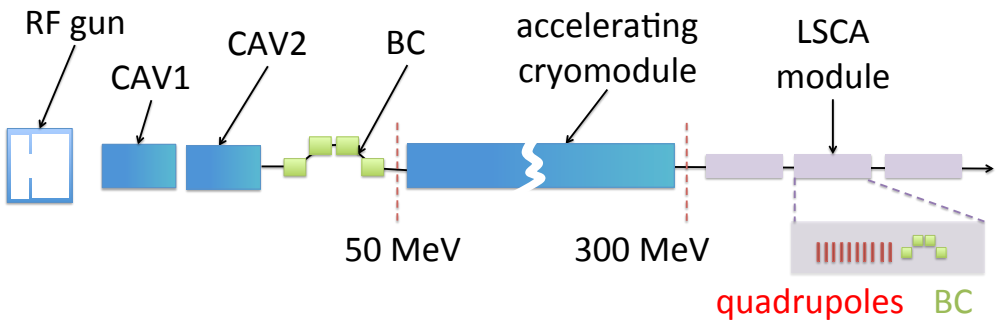

Figure 6.5: Overview of the proposed LSCA setup at FAST facility. The legend is as follows: "CAVx": accelerating cavities, "BC": magnetic chicane bunch compressor, the thin (red) rectangles and (green) square symbols respectively represent the quadrupole and dipole magnets.

peak current on the order of ~ 500 A and slice parameters gathered in Table 6.1 [116]. These parameters were used to generate initial distribution used in all the ELEGANT-BH simulations presented below. For simplicity we consider all the LSCA modules to be similar: they consist of 4 FODO-cell sections each followed by small bending angle chicanes. The only difference between the modules is the R_{56} parameters associated to the chicanes as explained below. The horizontal dispersion introduced by the chicanes is minimal and does not break the periodicity of the FODO cells. The settings of quadrupole magnets arranged as a FODO cell were optimized using single-particle dynamics simulations. The corresponding beam size evolution along one LSCA module appears in Fig. 6.6.

In our simulation we model the evolution of a thin longitudinal slice of the bunch with an equivalent peak current and slice parameters listed in Table 6.1. The slice is assumed to have a longitudinal Gaussian distribution (to avoid complication arising from sharp transition of a uniformly-distributed slice). The transverse distribution is also chosen to be Gaussian along the horizontal (x) and vertical (y) axis. Likewise, the divergence and energy distribution are all taken to be Gaussian.

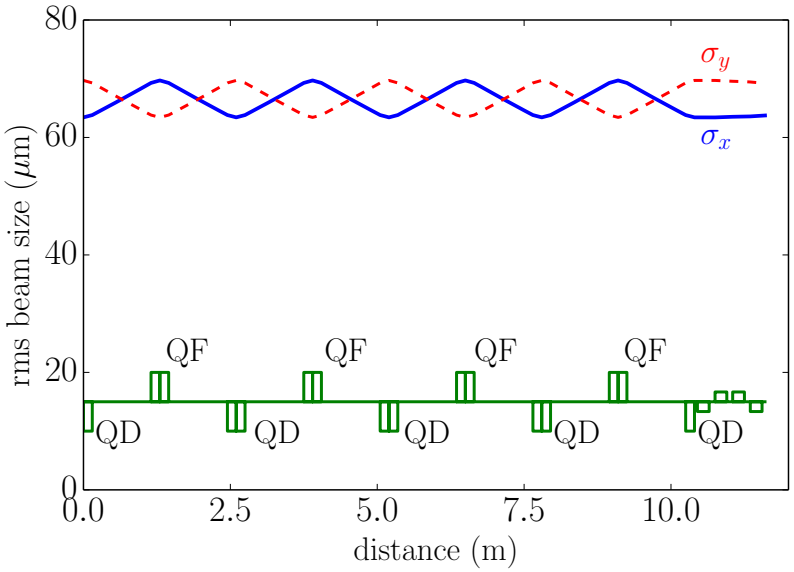

Figure 6.6: Horizontal (blue) and vertical (red) rms beam size evolution in one LSCA module. The envelopes are obtained in the single-particle dynamics limit. The green diagram indicates the location of the focusing (QF) and defocusing (QD) quadrupole magnets while the four smaller rectangles (at distance > 12 m) represent the chicane dipole magnets.

Table 6.1: Beam parameters considered for the LSCA simulations using the setup of Fig. 6.1.

Parameter, Symbol	**Value**	**Units**
Transv. spot size, $\sigma_{x,y}$	68.0	μm
Charge, Q	20.0	pC
Lorentz factor, γ	600	–
RMS bunch duration, τ	19	fs
Peak current, I	415	A
Transv. emittance, $\varepsilon_{x,y}$	5×10^{-8}	m
Frac. momentum spread, σ_δ	10^{-4}	–
Number of macroparticles, N	$[1-10] \times 10^6$	–

6.3.2 Optimization of one LSCA module and cascaded LSCA

We start with the optimization of one LSCA module consisting of several FODO sections and one BC. We varied two parameters at this point: the quadrupole magnet distance in the FODO sections and the bending angle in the chicane which affects its longitudinal dispersion R_{56}. As the goal of this study is to reach the shortest wavelength possible at FAST, we focus on small R_{56} values. Figure 6.7 provides the bunching factor in the frequency range $\omega \in [1{\times}10^{14}, 5{\times}10^{16}]$ Hz for varying value of $R_{56} \in -[2, 0.1]$ mm. Figure 6.7 also indicates that the high-frequency content suppression is following the expected scaling of Eq. 6.3. For the considered case of betatron function and reachable energy the optimum wavelength is $\lambda_{opt} \approx$ 750 nm (corresponding to $\omega_{opt} \approx 2.5 \times 10^{15}$ Hz), the broadband feature of the amplification process has spectral content up to $\lambda \sim 190$ nm (corresponding to $\omega \sim 1 \times 10^{16}$ Hz).

The simulations presented in Fig. 6.7 are performed with $N = 10^7$ macro-particles (while the slice actually contains $N_e = 125 \times 10^6$ electrons). Therefore the noise floor [111, 112] of the bunching factor is $\simeq 1/\sqrt{N_e} \simeq 9 \times 10^{-5}$ while our simulations are limited to noise floor of $\simeq 1/\sqrt{N} \simeq 3 \times 10^{-4}$. To verify the limited number of macro-particles does not significantly affect the retrieved gain we carried out numerical simulation for different values of N and found no dependence as seen in Fig. 6.8. In the latter case the longitudinal dispersion was set to $R_{56} = 364$ μm corresponding to an optimum wavelength of $\lambda_{opt} \simeq 750$ nm. The gain averaged over the 10 simulation is $\langle G \rangle = 23.6$ and its standard deviation $\langle G^2 \rangle^{1/2} = 1.28$ corresponding to a fractional spread of ~ 6 %. This result essentially demonstrates that our gain-calculation technique is independent of the number of macroparticles used in the simulation.

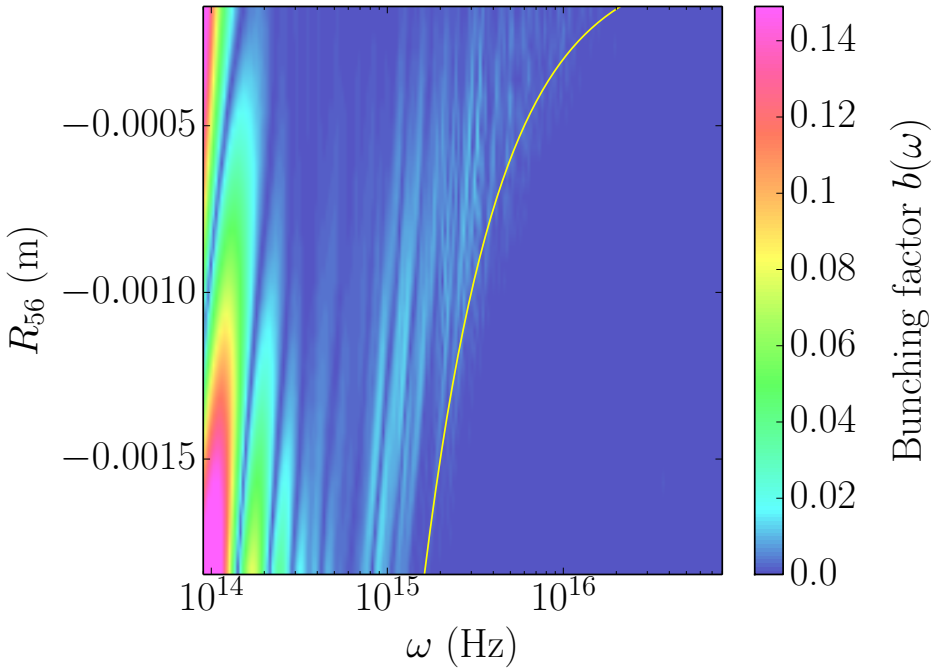

Figure 6.7: The evolution of the longitudinal dispersion R_{56} as a function of the modulation wavelength ω after passing through FODO+BC. The superimposed yellow curve represents the exponential cut-off in Eq. 6.3.

The striations observed along the frequency axis in Fig. 6.7 arises from the initial shot-noise[2]. The LSCA process, being seeded by the initial shot-noise in the beam, fluctuates shot-to-shot as different beam distribution is realized. Consequently, to perform noise-insensitive bunching factor analysis, we carried out 20 ELEGANT-BH runs for given lattice settings with different initial random seeds in order to generate independent realizations of initial bunch distribution. As an example we evaluated the bunching factor computed over the spectral region of interest $\omega \in [1 \times 10^{13}, 9 \times 10^{16}]$ Hz statistically averaged over the 20 independent runs appears in Fig. 6.9 (blue trace) and demonstrates that, in average, the frequency in the range $\omega \in [3 \times 10^{14}, 1 \times 10^{16}]$ Hz is associated with enhanced value of the bunching factor. Likewise, an average gain curve over the region of interest can be computed; see Fig. 6.10. In

[2]The same random realization of the initial distribution was used while scanning the value of R_{56}.

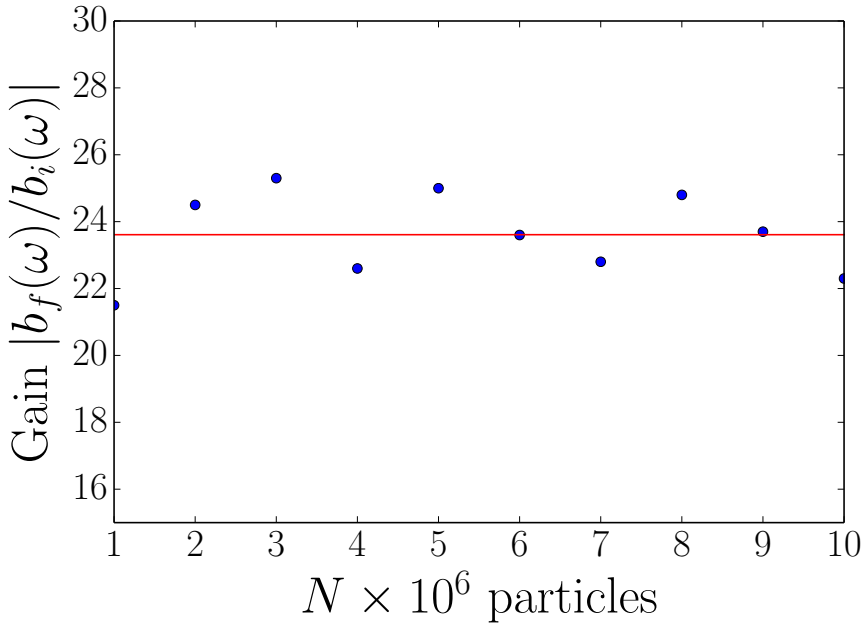

Figure 6.8: Gain for the first LSCA module as function of number of macro-particles N representing the beam (filled circles). The selected longitudinal dispersion and associated optimum wavelength are respectively $R_{56} = 364$ μm, and $\lambda_{opt} \simeq 750$ nm. The red trace represents the mean gain value obtained by averaging over the 10 simulation sets.

the case of a superconducting linac operating in a burst mode this type of average gain curve will practically be generated over a single burst (corresponding to a 1-ms RF macropulse accelerating 3000 statistically-independent bunches in the case of the FAST facility).

The latter figure reports the gain computed as the ratio between the final and initial bunching factors $|b_f(\omega)/b_i(\omega)|$. To smooth out the shot-to-shot nature of the gain, the presented gain is averaged over 20 random realizations of the initial macro-particle distribution.

We note that by introducing a chirp C it is possible to compress the optimum modulation wavelength to shorter value given by $\lambda_{comp} \simeq \lambda_{opt}/\kappa$ where the compression factor κ was introduced above.

To simulate a 3-stage LCSA module, we iterated the process described in the previous section for each stage so to ensure the R_{56} is properly optimized. The simulations were carried

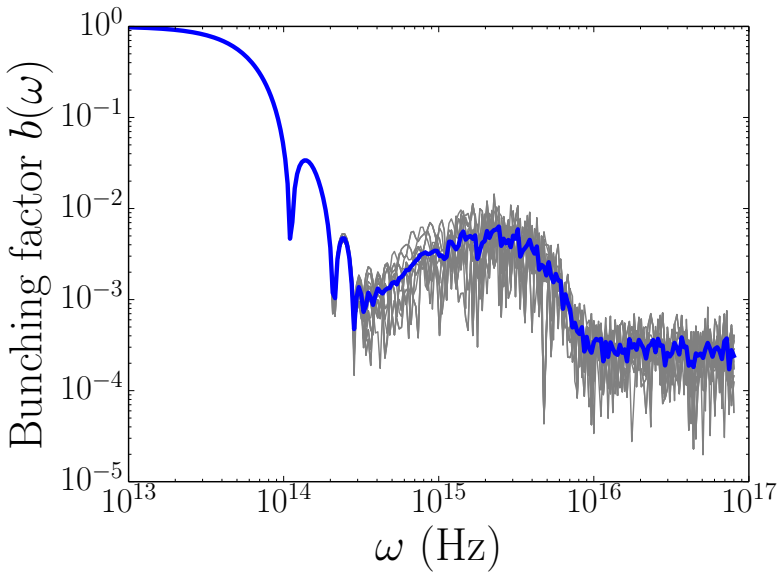

Figure 6.9: Bunch factor evaluated downstream of one LCSA module with R_{56} = 364 μm. The gray traces represent the bunching factors computed for 20 independent realizations of the initial bunch distributions while the solid blue trace corresponds to the averaged value.

out in a piecewise fashion. First, the FODO channel of stage n was simulated with space charge, the output was passed to the subsequent BC. The R_{56} was optimized to provide the largest bunching factor at the selected wavelength. The resulting distribution was rematched and then passed to the $n+1$ FODO channel where the process was repeated. As mentioned earlier the chicane has small R_{56} and single-particle dynamics does not affect the matching. However, in the presence of space charge for a 300-MeV beam, we find that the matching is significantly deteriorated therefore requiring rematching of the beam parameters after each module. The final optimized values for the R_{56} for first, second and third stage are respectively -364, -279, and -142 μm.

The total length of cascaded LSCA configuration is 28 m. This distance was selected based on the FAST lattice parameters and the amount of energy modulation acquired for one FODO cell. We note that other configurations are also possible (e.g. with longer drifts).

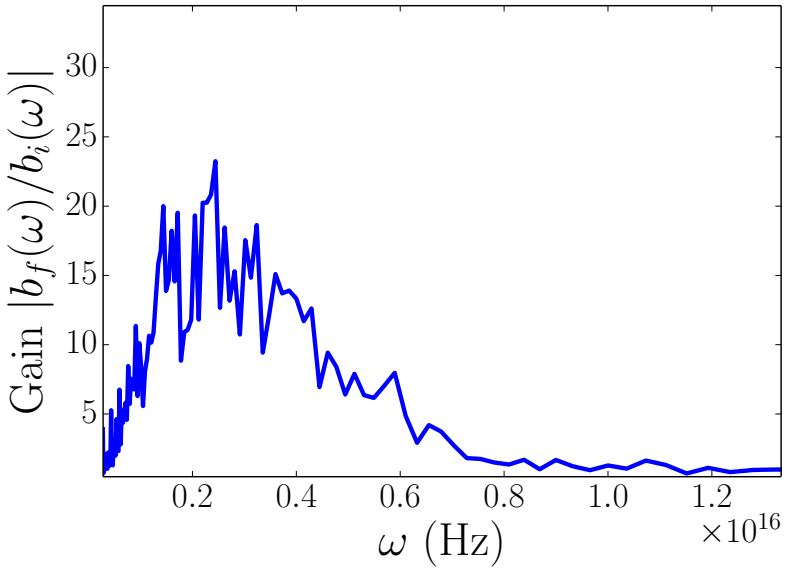

Figure 6.10: Gain curve as a function of frequency in the interval where significant gain is obtained. The curve is computed for a single (the first) LSCA module.

Evolution of the LPS associated to the 500-A slice being tracked throughout the LSCA modules appears in Fig. 6.11. At $\gamma = 600$ strong density modulations start to form downstream of the second LSCA module. The shortest microstructures in the LPS are achieved as the LSC-induced modulation has its local correlation C_{loc} satisfying $R_{56} = -1/C_{loc}$ giving rise to structured density profile with shortest temporal scale on the order of $\tau \simeq R_{56}\sigma_{\delta,u}/c$. Eventually the LPS becomes strongly disrupted as seen in Fig. 6.11(d) and Fig. 6.12.

The microbunches have durations of the order of hundred femtoseconds and could in principle lead to the generation of attosecond radition pulse; e.g. when co-propagated with ultrashort laser pulse in an undulator; see Ref. [97]. Because of the local energy chirp, additional effects related to wakefields and interactions with CSR radiation should also be taken into account.

Figure 6.13 represents the evolution of the bunching factor after each LSCA stage averaged over 20 random realizations of the initial bunch distribution. The broad spectral

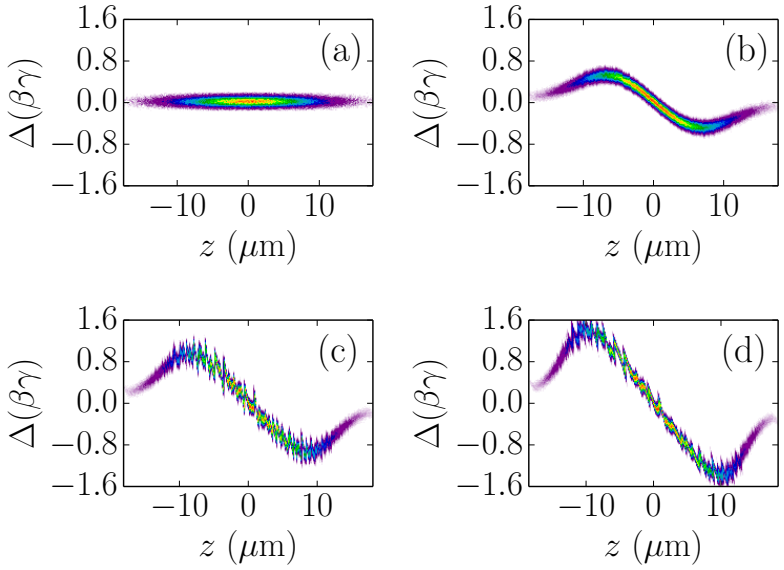

Figure 6.11: Snapshots of LPS evolution along the cascaded LSCA: initial (Gaussian) bunch before (a) and after passing through one (b), two (c) and three (d) LSCA modules. The Lorentz factor is $\gamma = 600$ and 10^7 macroparticles were used in these simulations.

features of the bunching factor observed in Fig. 6.7 are preserved until the end of the final stage. From the evolution of the bunching factor we inferred a total gain of $G \approx 500$ (evaluated at the optimum wavelength) for the considered three-stage LSCA .

One limitation found in the present study is the cumulated energy spread which leads to transverse emittance growth via chromatic aberration. This emittance dilution eventually leads to the suppression of the modulation (via an angular smearing effect). Overall, this effect results in saturation of the gain in the final stages as seen in Fig. 6.13. We actually find that gain for the first and second stage is $G \approx 20$ while it is only $G \approx 1.3$ for the last stage.

We finally point out that increasing the energy would provide a path to shorter wavelength as expected from the scaling described by Eq. 6.5. Such an opportunity is depicted in

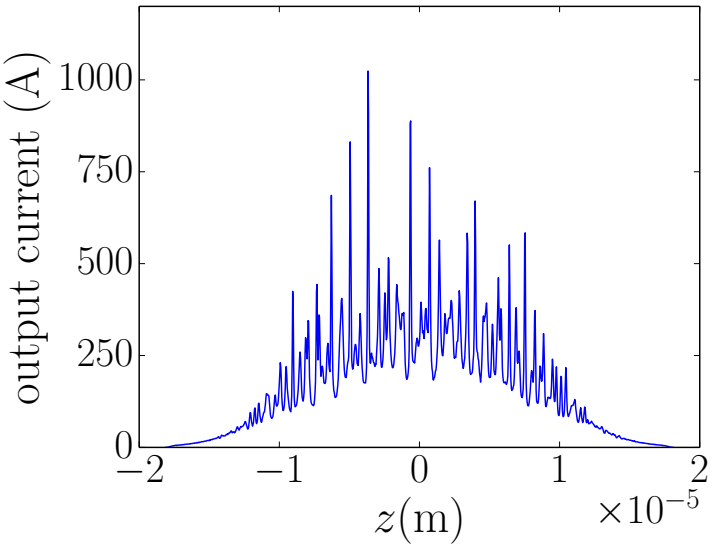

Figure 6.12: Final current profile downstream of the last LSCA module. Here the number of macro-particles was taken to be $N = 10^7$.

Fig. 6.14. Again the simulation qualitatively captures the expected scaling for the optimum frequency $\omega_{opt} \equiv 2\pi c/\lambda_{opt}$ (though the striations prevent from a quantitative comparison).

6.3.3 Compressed case

In the previous sections we specialized to the case where the incoming LPS is uncorrelated. Introducing a LPS chirp can significantly decrease the wavelength to lower values well in the ultraviolet (UV) range. As an example, we computed the final bunching factor obtained from the same setup as in the previous section with an initial LPS with a chirp $C \equiv \frac{d\delta}{dz}\big|_0 =$ 1667 m^{-1}. This chirp is numerically applied and corresponds to the value that would result in a maximum compression downstream of the three BCs used in the LSCA module. The

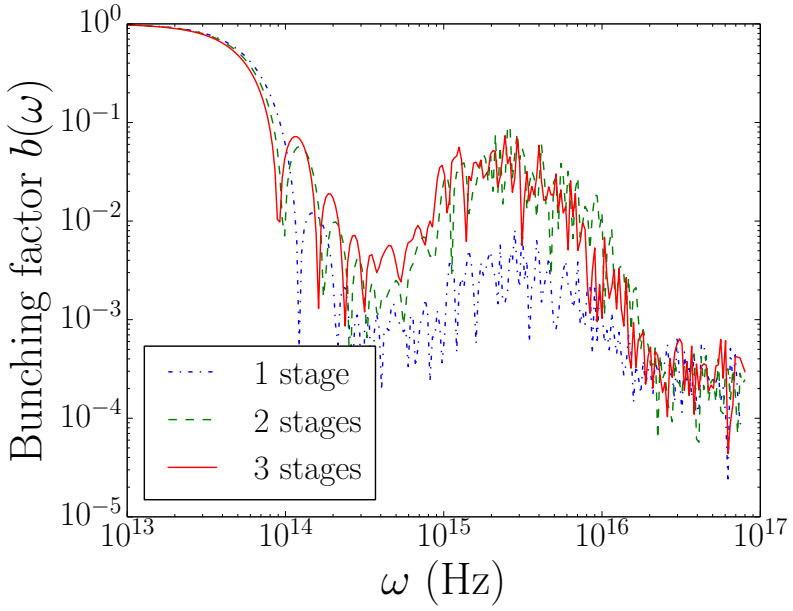

Figure 6.13: Bunching factor extracted from the LPS's shown in Fig. 6.11. The blue, red, and green traces respectively correspond the the bunching factor downstream of the first, second and final LSCA stages.

resulting bunching factor has significant content ($b_f \simeq 1\%$) at $\lambda \approx 140$ nm (ω=1.4·10^{16} Hz); see Fig. 6.15 (green trace).

Here we stress that, for simplicity, the chirp was "numerically applied" just before the last bunch compressor (thus its large value). In practice such a large chirp might be challenging to achieve using conventional off-crest operation of the linac (especially given the low operating frequency of the considered superconducting linac 1.3 GHz). However, we note that advanced technique such as the application of a nonlinear chirp with a dielectric-lined waveguide might provide the required chirp [117]. Additionally, milder compression might be implemented (corresponding to much lower chirps).

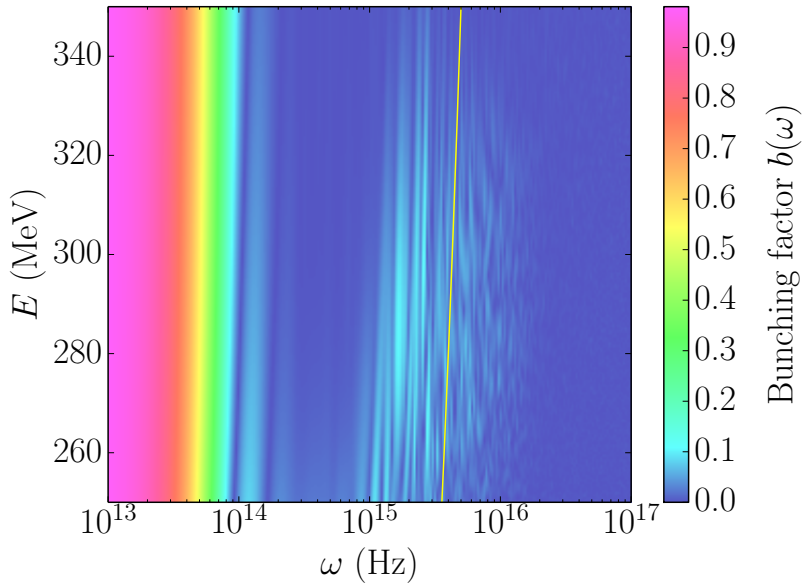

Figure 6.14: Evolution of the bunching factor $b(\omega)$ as a function of bunch energy. The superimposed yellow line represents the optimal wavelength λ_{opt}.

6.3.4 Radiation mechanism

The electromagnetic radiation emitted by a bunch of electrons has its spectral-angular fluence given by

$$\frac{dW}{d\omega d\Omega} = [N + N(N-1)b(\omega)^2]\frac{dW}{d\omega d\Omega}\Big|_1, \tag{6.9}$$

where $\frac{dW}{d\omega d\Omega}\Big|_1$ represents the single-electron radiation spectral fluence associated to the considered electromagnetic process. The latter equation assumes the beam follows line-charge distribution. In practice when the beam has a transverse extent the radiation is suppressed $\frac{dW}{d\omega d\Omega} \rightarrow \frac{dW}{d\omega d\Omega} \times \mathcal{F}$ where a multiplicative suppression factor ($\mathcal{F} \leq 1$) has to be included [118]. In principle any radiation mechanisms can be considered. Here we consider the case when the beam simulated in the previous section is passed through an undulator magnet thereby

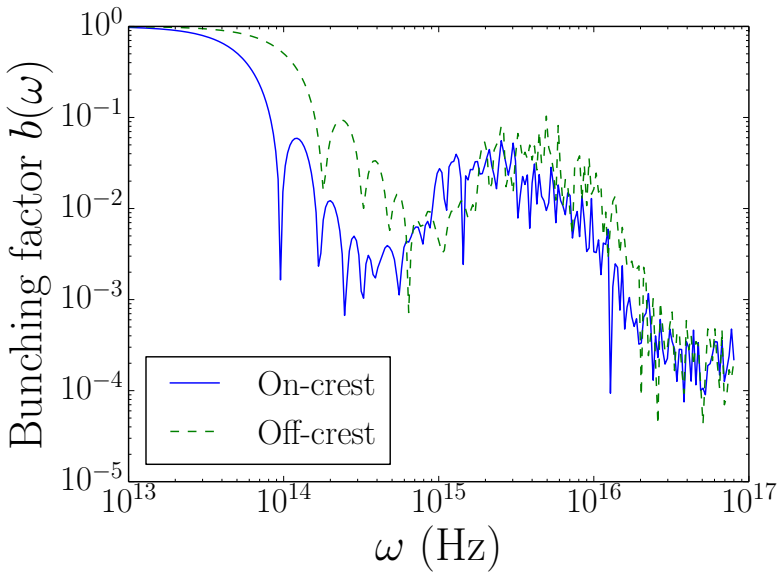

Figure 6.15: Simulated bunching factor downstream of the third LSCA stage for the case of an uncompressed (blue) and compressed (green) incoming beam. The simulations are performed with 10^7 macroparticles.

generating undulator radiation (UR). The fundamental wavelength of UR is related to the undulator period λ_u via

$$\lambda = \frac{\lambda_u}{2\gamma^2}\left(1 + \frac{K^2}{2} + \gamma^2\theta^2\right), \tag{6.10}$$

where θ is the direction of observation with respect to the electron-beam direction and the undulator parameter is $K \equiv \frac{eB}{k_u mc}$, where B is the undulator peak field, $k_u \equiv \frac{2\pi}{\lambda_u}$, and e, and m are respectively the electronic charge and mass. In order to reach ultraviolet wavelength on axis ($\theta = 0$) for $\gamma = 600$ we select an undulator period of $\lambda_u = 5$ cm and a tunable $K \in [0.49, 3.9]$. The latter parameters correspond to the `U5.0` ALS undulator [119]. The range of attainable undulator parameters would allow for radiation to be generated within the spectral range $\lambda \in [78, 498]$ nm which covers the range where LSCA-induced micro-bunching is sustained.

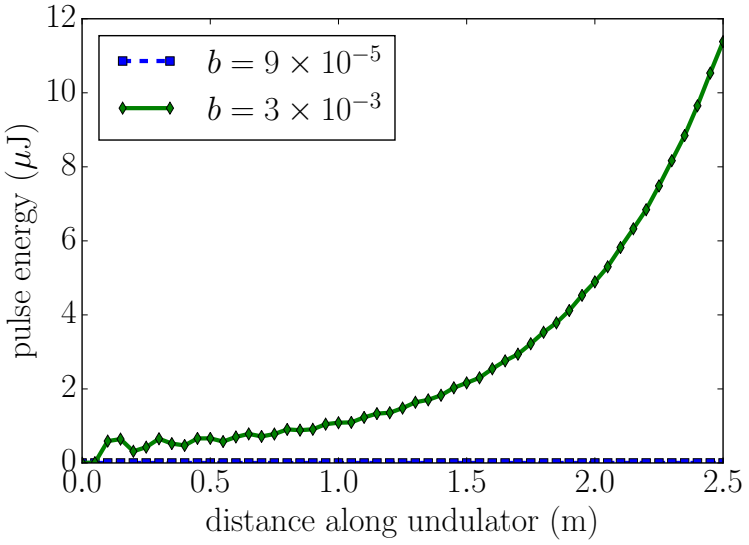

Figure 6.16: Evolution of the undulator radiation for $\lambda = 235.5$ nm for a scaled bunching factor of 3×10^{-3} (blue trace, diamond symbols). The radiation produced by a beam without micro-bunching modulations, e.g. with bunching factor $b = 1/\sqrt{N_e} \simeq 9 \times 10^{-5}$, is also displayed (green trace, square symbols) for comparison.

Table 6.2: Electron-beam and undulator parameters used for the GENESIS simulations.

Parameter, Symbol	**Value**	**Units**
Transv. spot size, $\sigma_{x,y}$	50.0	μm
Lorentz factor, γ	600	–
Peak current, I	500	A
Transv. emittance, $\varepsilon_{x,y}$	5×10^{-8}	m
Frac. momentum spread, σ_δ	5×10^{-4}	–
Undulator period, λ_u	5.0	cm
Undulator parameter, K	2.18	–
Radiation wavelength, λ	235.5	nm

To quantitatively assess the properties of undulator radiation produced seeded by a LSCA-microbunched beam, we employ the program GENESIS [120]. The beam parameters are consistent with the beam parameters generated downstream of the LCSA; see Tab. 6.2. For our simulation we rescale the bunching factor obtained with $N = 10^7$ macroparticles, see

Fig. 6.15, to the real number of electron in the considered axial slice $N_e = 1.2 \times 10^8$ following $b(\lambda) \rightarrow \sqrt{\frac{N}{N_e}} b(\lambda)$ where $\sqrt{\frac{N}{N_e}} \simeq 0.29$. This scaled bunching factor obtained for a specific wavelength is then used as an input in the steady state GENESIS simulation. The simulated evolution of the radiation pulse energy along the undulator length appears in Fig. 6.16. In the latter Figure we considered a wavelength of $\lambda = 235.5$ nm with a scaled bunching factor of $\simeq 3 \times 10^{-3}$ (i.e. a nominal bunching factor of 1×10^{-2} in Fig. 6.15). Our simulations demonstrate that UV pulses with energies on the order of ~ 10 μJ could be reached downstream of a meter-scale section of the undulator three orders of magnitudes above the "shot-noise" radiation of 9 nJ (achieved with an initial shot-noise bunching factor of $b = 1/\sqrt{N_e}$).

CHAPTER 7

CONCLUSIONS

Electron accelerators are a valuable part of current accelerator technology advancement and will contribute to the future machines as well. In the present work, we focused on several electron beam shaping methods.

We demonstrated the possible use of a microlens array to control the transverse distribution of a photocathode laser pulse and associated photoemitted electron bunches. We especially confirmed that this simple and rather inexpensive setup could be used to homogenize the beam transverse distribution thereby improving the transverse emittance. Additionally, we investigated the generation of patterned electron beams consisting of multiple transversely-separated beamlets. The latter type of beam could be used for various application and could yield temporally-modulated electron beam when combined with a transverse-to-longitudinal emittance-exchange beamline but also serve as a beam-based diagnostics. We illustrated the application of the patterned beam to diagnose the magnetization of a magnetized beam (by using the beam evolution to infer the the axial magnetic applied at the photocathode surface). The application of patterned beams could be further extended to explore, e.g, nonlinearities in linear accelerators and characterize beamline element (transfer matrix measurement). Given its simplicity, low cost and versatility we expect the results of this research to motivate further applications to photoemission electron sources and laser-heater system.

We have measured the transfer matrix of a 1.3-GHz SRF accelerating cavity at the IOTA/FAST facility. The measurements are found to be in good agreement with numerical simulations and analytical results based on the Chambers' model. In particular, the contri-

butions from the auxiliary couplers are small and does not affect the 4×4 matrix which can be approximated by a symmetric 2×2-block diagonal matrix within our experimental uncertainties. Furthermore, the electromagnetic-field deviations from a pure cylindrical-symmetric TM_{010} mode do not significantly affect the *single-particle* beam dynamics. It should however be stressed that nonlinearities along with the time-dependence of the introduced dipole, and non-cylindrical-symmetric first order perturbations contribute to transverse-emittance dilutions [121, 27]. Investigating such effects would require beams with ultra-low emittances.

A unique capability of the IOTA/FAST photoinjector to produce highly magnetized beams was utilized to generate vertical and horizontal flat beams with the ratio of 100. The lower emittance in the latter type of beams corresponds to below-thermal emittance of the photoinjector and can pave the way for multiple future experiments at FAST. Such experiments include dielectric laser acceleration [122], phase-space manipulation and acceleration in dielectric lined waveguides [123, 117, 124], plasma wakefield acceleration [125, 126], microundulator radiation [49]. Low emittance flat beams could also serve as a probe for high-order mode auxiliary couplers studies in the ILC-type cryomodule. Additionally, magnetized beams could be injected into IOTA for microbunching supression [127].

Using a grid-less code adapted from Astrophysics we have investigated three-dimensional effects in the LSC impedance and confirmed that the one-dimensional often used LSC impedance model is a good approximation. Additionally we benchmarked the radial dependence of the space-charge impedance with the analytical results developed in Ref. [113]. Finally, we confirmed the possible use of a cascaded LSCA scheme to produce femtosecond microstructures in the beam current with spectral range attaining the ultraviolet domain using electron-beam parameters achievable at FAST facility.

REFERENCES

[1] B. Aune, *et al.*, "The superconducting TESLA cavities," Phys. Rev. ST Accel. Beams, **3**, 092001, (2000).

[2] N. Phinney, N. Toge and N. Walker (Eds), "ILC Reference Design Report Volume 3 - Accelerator," arXiv:0712.2361 [physics.acc-ph] (2007)

[3] J. N. Galayda, "The New LCLS-II Project : Status and Challenges," in Proceedings of the International Linear Accelerator Conference (LINAC2014), JACoW, Geneva, Switzerland, p. 404 (2014).

[4] M. Popovic and R. P. Johnson, "Muon acceleration in a superconducting proton Linac," Nucl. Phys. Proc. Suppl. **155**, 305, (2006).

[5] S. Holmes, P. Derwent, V. Lebedev, S. Mishra, D. Mitchell, V. P. Yakovlev, "PIP-II Status and Strategy," in Proceedings of the 2015 International Particle Accelerator Conference (IPAC15), JACoW, Richmond, VA, USA, p. 3982, (2015).

[6] R.D. Kephart, B.E. Chase, I.V. Gonin, A. Grassellino, S. Kazakov, T.N. Khabiboulline, S. Nagaitsev, R.J. Pasquinelli, S. Posen, O.V. Pronitchev, A. Romanenko, V.P. Yakovlev, "SRF Compact Accelerators for Industry & Society," in Proceeding of International Conference on RF Superconductivity (SRF2015), JACoW, Whistler, BC, Canada, p. 1467, (2015).

[7] S. Antipov, D. Broemmelsiek, D. Bruhwiler, D. Edstrom, E. Harms, V. Lebedev, J. Leibfritz, S. Nagaitsev, C.S. Park, H. Piekarz, P. Piot, E. Prebys, A. Romanov, J. Ruan, T. Sen, G. Stancari, C. Thangaraj, R. Thurman-Keup, A. Valishev, and

V. Shiltsev. "Iota (integrable optics test accelerator): facility and experimental beam physics program," *Journal of Instrumentation*, 12(03):T03002, (2017).

[8] S. Abeyratne *et. al.*, MEIC Design Summary. (2015).

[9] G. I. Budker and A. N. Skrinsky. "The electron Cooling and New Possibilities in Elementary Particle Physics," *Sov. Phys. Usp.*, **21**, p. 277–298, (1978). *Usp. Fiz. Nauk* **124**, p. 561 (1978).

[10] N. S. Dikansky, I. N. Meshkov, and A. N. Skrinsky. "Electron Cooling and Its Applications in Elementary Particle Physics," *Nature*, **276**, pp. 763–767, (1978).

[11] Ya. Derbenev. "Adapting optics for high-energy electron cooling," UM-HE-98-04-A, (1998).

[12] Y. E Sun, P. Piot, K. J. Kim, N. Barov, S. Lidia, J. Santucci, R. Tikhoplav, and J. Wennerberg. "Generation of angular-momentum-dominated electron beams from a photoinjector," *Phys. Rev. ST Accel. Beams*, **7**, p. 123501, (2004).

[13] Yin-e Sun. *"Angular-momentum-dominated electron beams and flat-beam generation"*. PhD thesis, Chicago U., (2005).

[14] P. Piot, Y.-E Sun, and K.-J. Kim. "Photoinjector generation of a flat electron beam with transverse emittance ratio of 100," *Phys. Rev. ST Accel. Beams*, **9**, p. 031001, (2006).

[15] D. J. Jackson. *Classical Electrodynamics*. Wiley, New York, (1998).

[16] H. Goldstein, C.P. Poole, and J.L. Safko. *Classical Mechanics*. Addison Wesley, (2002).

[17] M. Reiser. *Theory and design of charged particle beams*. Wiley, New York, (1995).

[18] H. Busch. "Berechnung der bahn von kathodenstrahlen im axialsymmetrischen elektromagnetischen felde," *Annalen der Physik*, 386(25), pp. 974–993, (1926).

[19] R. Brinkmann, Ya. Derbenev, and K. Flottmann. "A low emittance, flat-beam electron source for linear colliders," *Phys. Rev. ST Accel. Beams*, **4**, p. 053501, (2001).

[20] I. L. Klimontovich. "The kinetic theory of electromagnetic processes," *Springer Verlag Springer Series on Synergetics*, **10**, (1983).

[21] K. Flöttmann, Astra reference manual, available from DESY (`http://www.desy.de/~mpyflo/`), Hamburg, Germany (unpublished).

[22] J. Qiang, "Impact-t reference manual," *LBNL-62326*, (2007).

[23] M. Borland, "elegant: A flexible sdds-compliant code for accelerator simulation," *Advanced Photon Source*, LS-287, (2000).

[24] Karl L. Brown and R. Servranckx. "First- and second-order charged particle optics," *AIP Conf. Proc.*, **127**, pp. 62–138, (1985).

[25] P. Piot, M. Dohlus, K. Flottmann, M. Marx, and S. G. Wipf. "Steering and focusing effects in TESLA cavity due to high order mode and input couplers," *Conf. Proc.*, C0505161:4135, (2005).

[26] M. Dohlus, I. Zagorodnov, E. Gjonaj, and T. Weiland. "Coupler Kick for Very Short Bunches and its Compensation," *Conf. Proc.*, C0806233:MOPP013, (2008).

[27] A. Lunin, I. Gonin, N. Solyak, and V. Yakovlev. "Final Results on RF and Wake Kicks Caused by the Couplers for the ILC Cavity," *Conf. Proc.*, C100523:WEPE034, (2010).

[28] N. Baboi, M. Dohlus, C. Magne, A. Mosnier, O. Napoly, and H. W. Glock. "Investigation of a high-Q dipole mode at the TESLA cavities," in *Particle accelerator.*

Proceedings, 7th European Conference, EPAC 2000, Vienna, Austria, Vol. 1-3, pp 1107–1119, (2000).

[29] P. Piot and Y.E. Sun. "Note on the transfer matrix measurement of a tesla cavity," *FNPL Note*, (2004).

[30] A. Halavanau, N. Eddy, D. Edstrom, A. Lunin, P. Piot, J. Ruan, J. Santucci, and N. Solyak. "Preliminary Measurement of the Transfer Matrix of a TESLA-type Cavity at FAST," in *Proceedings, 7th International Particle Accelerator Conference (IPAC 2016): Busan, Korea*, p. TUPMY038, (2016).

[31] A. Halavanau, N. Eddy, D. Edstrom, A. Lunin, P. Piot, J. Ruan, and N. Solyak. "Measurement of the Transverse Beam Dynamics in a TESLA-Type Superconducting Cavity," in *Proceedings, 28th International Linear Accelerator Conference (LINAC16): East Lansing, Michigan*, p. MOP106018, (2017).

[32] E.E. Chambers. "Radial transformation matrix, standing wave accelerator," *HEPL TN-68-17 and HEPL 570*, (1968).

[33] J. Rosenzweig and L. Serafini. "Transverse particle motion in radiofrequency linear accelerators," *Phys. Rev.*, E **49**, pp. 1599–1602, (1994).

[34] S. C. Hartman and J. B. Rosenzweig. "Ponderomotive focusing in axisymmetric rf linacs," *Phys. Rev.*, E **47**, pp. 2031–2037, (1993).

[35] S. C. Hartman, "The UCLA high-brightness RF photoinjector", Ph.D. Dissertation, University of California, Los Angeles, USA (1994).

[36] S. Reiche, J. B. Rosenzweig, S. Anderson, P. Frigola, M. Hogan, A. Murokh, C. Pellegrini, L. Serafini, Gil A. Travish, and A. Tremaine. "Experimental confirmation

of transverse focusing and adiabatic damping in a standing wave linear accelerator," *Phys. Rev.*, E **56**, pp. 3572–3577, (1997).

[37] A. Lunin, N. Solyak, A. Sukhanov, V. Yakovlev, "Coupler RF Kick in the Input 1.3 GHz Accelerating Cavity of the LCLS-II Linac," in Proceedings of the 2015 International Particle Accelerator Conference (IPAC15), JACoW, Richmond, VA, USA, 571 (2015).

[38] K. L. F. Bane et al. "Wakefield and RF Kicks Due to Coupler Asymmetry in TESLA-Type Accelerating Cavities," *Conf. Proc.*, C0806233:TUPP019, (2008).

[39] K. J. Kim. "Round-to-flat transformation of angular-momentum-dominated beams," *Phys. Rev. ST Accel. Beams*, **6**, p. 104002, (2003).

[40] K. Kubo. "How to calculate intrinsic emittances from 4-dimensional beam matrix." *ATF Internal Report, ATF-99-02*, (1999).

[41] S. Nagaitsev and A. Shemyakin. "Beam emittance calculation in the presence of an axially symmetric magnetic field," FERMILAB-TM-2107, (2000).

[42] S. Lidia. "Emittance compensation of intense, magnetized beams and optimization of photoinjectors," *LUX Tech Note-012, LBNL-56558* (2012).

[43] Karl L. Brown. "A First and Second Order Matrix Theory for the Design of Beam Transport Systems and Charged Particle Spectrometers," *Adv. Part. Phys.*, **1**, pp. 71–134, (1968).

[44] E. Thrane *et. al.*, "Photoinjector production of a flat electron beam." *Conf. Proc.*, p. TU404, (2002).

[45] A. Halavanau, MagnetOptimizer available from `https://github.com/NIUaard/MagnetOptimizer`, (2017).

[46] D. Edwards, H. Edwards, N. Holtkamp, S. Nagaitsev, J. Santucci, R. Brinkmann, K. Desler, K. Flottmann, I. Bohnet, and M. Ferrario. "The Flat beam experiment at the FNAL photoinjector." *eConf*, C000821:MOB13, (2000).

[47] P. Piot and Y. E. Sun. "Generation and dynamics of magnetized electron beams for high-energy electron cooling," *FERMILAB-CONF-14-142-APC* (2014).

[48] P. Piot *et. al.*, "Beam dynamics simulations of the nml photoinjector at fermilab." *Proceedings of IPAC'10*, Kyoto, Japan, p. 4316, (2010).

[49] C. Prokop, "Advanced Phase Space Manipulations at the Fermilab's Advanced Superconducting Test Accelerator", Ph.D. Dissertation, Northern Illinois University, DeKalb, IL, USA (2014).

[50] E. Harms *et. al.*, "The Advanced Superconducting Test Accelerator at Fermilab," *ICFA Beam Dyn.Newslett.*, **64**, pp. 133–156, (2014).

[51] P. Piot and A. Halavanau. "A high-level Python interface to the Fermilab ACNET control system," *FERMILAB-CONF-16-464-AD-APC*, (2016).

[52] Min Zhang. "Emittance formula for slits and pepper pot measurement," report FERMILAB-TM-1988, (1996).

[53] E. McCrory, N. Eddy, F.G. Garcia, S. Hansen, T. Kiper, M. Sliczniak, "BPM Electronics Upgrade for the Fermilab H- Linac Based Upon Custom Downconverter Electronics," in Proceedings of the 2nd International Beam Instrumentation Conference (IBIC13), Oxford, UK, 396 (2013).

[54] High frequency structure simulator. Software available from ANSYS.

[55] N. Juntong and R. M. Jones. "Hom and FP Coupler Design for the NLSF High Gradient SC Cavity," *Conf. Proc.*, C110904, pp. 325–327, (2011).

[56] P. M. Lapostolle, A. L. Septier, R.H. Helm, and R. Miller. *Linear Accelerators*. North-Holland Publ., Amsterdam, (1969).

[57] T. J. Peterson and J. G. Weisend II. "TESLA & ILC Cryomodules," pp. 117–145, (2016).

[58] R. Marwan, "Phase Space Manipulation in High-Brightness Electron Beams," Ph.D. Dissertation, Northern Illinois University, DeKalb, IL, USA (2011).

[59] M.E. Conde, *et al, Proceedings of IPAC'10*, Kyoto, Japan, paper THPD016, (2010).

[60] P. Schreiber, S. Kudaev, P. Dannberg, U. D. Zeitner, "Homogeneous led-illumination using microlens arrays," Proceedings of SPIE, **5942** (2005).

[61] F.M. Dickey and S.C. Holswade, *Laser Beam Shaping: Theory and Techniques*, Optical Science and Engineering, Taylor & Francis (2000).

[62] Y. Shibata, T. Takahashi, T. Kanai, K. Ishi, M. Ikezawa, J. Ohkuma, S. Okuda, T. Okada, "Diagnostics of an electron beam of a linear accelerator using coherent transition radiation," Phys. Rev. E, **50**, pp. 1479-1484 (1994).

[63] W. S. Graves, F. X. Kärtner, D. E. Moncton, and P. Piot, "Intense Superradiant X Rays from a Compact Source Using a Nanocathode Array and Emittance Exchange", Phys. Rev. Lett., **108**, p. 263904 (2012).

[64] O. Chubar, A. Fluerasu, L. Berman, K. Kaznatcheev, and L. Wiegart, "Wavefront propagation simulations for beamlines and experiments with SRW", J. Phys. Conf. Ser., **425**, 162001 (2013).

[65] SUSS MicroOptics techinfo sheet 10, "Beam homogenizing", (2008).

[66] Python NUMPY library.

[67] S.B. van der Geer, *et al,* "3D space-charge model for GPT simulations of high brightness electron bunches", Institute of Physics Conference Series, **175**, 101 (2005).

[68] F. Zhou, I. Ben-Zvi, M. Babzien, X. Y. Chang, A. Doyuran, R. Malone, X. J. Wang, and V. Yakimenko, "Experimental characterization of emittance growth induced by the nonuniform transverse laser distribution in a photoinjector", Phys. Rev. ST Accel. Beams, **5**, 094203 (2002).

[69] M. Rihaoui, P. Piot, J. G. Power, Z. Yusof, and W. Gai. "Observation and simulation of space-charge effects in a radio-frequency photoinjector using a transverse multibeamlet distribution", Phys. Rev. ST Accel. Beams, **12**, 124201 (2009).

[70] K. Flottmann "Note on the thermal emittance of electrons emitted by cesium telluride photocathodes", report DESY-TESLA-FEL-97-01, (1997).

[71] G. Voronoi. *J. Reine Angew. Math*, **134**, pp. 198–287, (1908).

[72] Franz Aurenhammer. "Voronoi diagrams& a survey of a fundamental geometric data structure," *ACM Comput. Surv.*, 23(3), pp. 345–405, (1991).

[73] Phuc T. Luu, T. Tuckmantel, and A. Pukhov. "Voronoi particle merging algorithm for {PIC} codes," *Computer Physics Communications*, **202**, pp. 165 – 174, (2016).

[74] J. G. Power, Manoel Eduardo Conde, W. Gai, F. Gao, R. Konecny, W. Liu, Z. Yusof, Ph Piot, and M. Rihaoui. "Pepper pot Based Emittance Measurements of the AWA Photoinjector," *Conf. Proc.*, C070625:4393, (2007).

[75] J. Power, M. Conde, W. Gai, W. Liu, and P. Piot. "Pepper-Pot Based Diagnostics for the Measurement of the 4D Transverse Phase Space Distribution from an RF Photoinjector at the AWA," Vancouver, Canada, p. TH5RFP005, (2010).

[76] V. Marx, "Neurobiology: Brain mapping in high resolution", Nature, **503**, 147-152 (2013).

[77] T. Kondoh, J. Yang, Y. Yoshida, H. Kashima, K. Kan, K. Norizawa, A. Ogata, and S. Tagawa. "Spatial resolution and contrast of the intensity modulated electron beam by the photocathode rf gun for the radiation therapy." *Proceedings of EPAC08, Genoa, Italy*, p. tupp121 (2008).

[78] P. Piot, Y.-E Sun, J. G. Power, and M. Rihaoui. "Generation of relativistic electron bunches with arbitrary current distribution via transverse-to-longitudinal phase space exchange," *Phys. Rev. ST Accel. Beams*, **14**, p. 022801, (2011).

[79] Y.-E Sun, P. Piot, A. Johnson, A. H. Lumpkin, T. J. Maxwell, J. Ruan, and R. Thurman-Keup, "Tunable subpicosecond electron-bunch-train generation using a transverse-to-longitudinal phase-space exchange technique", Phys. Rev. Lett., **105**, p. 234801 (2010).

[80] Y. E. Sun, J. G. Power, K. J. Kim, P. Piot, and M. M. Rihaoui, "Design study of a transverse-to-longitudinal emittance exchange proof-of-principle experiment", Proceedings of 2007 Particle Accelerator Conference (PAC07), JACoW, pp. 3441-3443 (2007).

[81] G. Ha, M. H. Cho, W. Namkung, J. G. Power, D. S. Doran, E. E. Wisniewski, M. Conde, W. Gai, W. Liu, C. Whiteford, Q. Gao, K.-J. Kim, A. Zholents, Y.-E Sun, C. Jing, and P. Piot, "Precision control of the electron longitudinal bunch shape using an emittance-exchange beam line", Phys. Rev. Lett., **118**, p. 104801 (2017).

[82] J. Barnes and P. Hut, "A hierarchical O(N log N) force-calculation algorithm", Nature, **324**, pp. 446-449 (1986).

[83] J.M. Maxson, I.V. Bazarov, W. Wan, H.A. Padmore, and C.E. Coleman-Smith, "Fundamental photoemission brightness limit from disorder induced heating", New Journal of Physics, **15** (10), p. 103024 (2013).

[84] A. Halavanau and P. Piot, "Simulation of a cascaded longitudinal space charge amplifier for coherent radiation generation", Nuclear Instruments and Methods in Physics Research Section A, **819**, pp. 144-153 (2016).

[85] Q. Gao, G. Ha, C. Jing, S. P. Antipov, J. G. Power, M. Conde, W. Gai, H. Chen, J. Shi, E. E. Wisniewski, D. S. Doran, W. Liu, C. E. Whiteford, A. Zholents, P. Piot, and S. S. Baturin. "Observation of high transformer ratio of shaped bunch generated by an emittance-exchange beam line," *Phys. Rev. Lett.*, **120**, p. 114801, (2018).

[86] Z. Li, J.J. Bisognano, B.C. Yunn, "Transport properties of the CEBAF cavity," in Proceedings of the 1993 Particle Accelerator Conference (PAC93), JACoW, Washington D.C, 179 (1993).

[87] D. Dowell, "Cancellation of RF coupler-induced emittance due to astigmatism," preprint arXiv:1503.09142 [physics.acc-ph] also available as report SLAC-PUB-16896 (2015).

[88] D. P. Juarez-Lopez, "Beam position monitor and energy analysis at the Fermilab Accelerator Science and Technology facility," M.S. Thesis, University of Guanajuato, Mexico (2015).

[89] J. Zhu, P. Piot, D. Mihalcea, and C. R. Prokop, "Formation of Compressed Flat Electron Beams with High Transverse-Emittance Ratios," Phys. Rev. ST Accel. Beams **17**, p. 084401 (2014).

[90] Poisson Superfish simulation software, available from `http://laacg.lanl.gov/laacg/services/download_sf.phtml` reports LA-UR-87-126 and LA-UR-87-115, (1987)

[91] K. L. F. Bane *et. al.* "Measurements and Modeling of Coherent Synchrotron Radiation and its Impact on the LCLS Electron Beam," *Phys. Rev. ST Accel. Beams*, **12**, p. 030704, (2009).

[92] Ya. S. Derbenev, J. Rossbach, V. D. Shiltsev, and E. L. Saldin. "Microbunch radiative tail - head interaction," (1995).

[93] C. Mitchell, J. Qiang, and P. Emma. "Longitudinal pulse shaping for the suppression of coherent synchrotron radiation-induced emittance growth," *Phys. Rev. ST Accel. Beams*, **16**, p. 060703, (2013).

[94] H. Loos, R. Akre, A. Brachmann, and F.-J. Decker. "Observation of coherent optical transition radiation in the LCLS linac," *SLAC-PUB-13395*, (2008).

[95] P. Piot *et. al.*, "Emittance and energy spread studies in the Jefferson Lab free-electron laser," *Proceedings of EPAC*, Vienna, Austria, (2000).

[96] M. Borland. "Modeling of the microbunching instability," *Phys. Rev. ST Accel. Beams*, *11*, p. 030701, (2008).

[97] M. Dohlus, E. A. Schneidmiller, and M. V. Yurkov. "Generation of attosecond soft x-ray pulses in a longitudinal space charge amplifier," *Phys. Rev. ST Accel. Beams*, **14**, p. 090702, (2011).

[98] A. Burov. "Head-tail modes for strong space charge," *Phys. Rev. ST Accel. Beams*, **12**, p. 044202, (2009).

[99] E.L. Saldin, E.A. Schneidmiller, and M.V. Yurkov. "An analytical description of longitudinal phase space distortions in magnetic bunch compressors," *Nuclear Instruments and Methods in Physics Research Section A: Accelerators, Spectrometers, Detectors and Associated Equipment*, 483(1–2), pp. 516 – 520, (2002).

[100] Dohlus M., Schneidmiller E., Yurkov M. V., Henning C., and Gruner F. J. "Longitudinal space charge amplifier driven by a laser-plasma accelerator," *Proc. SPIE*, p. 87791T, (2013).

[101] M. Venturini. "Models of longitudinal space-charge impedance for microbunching instability," *Phys. Rev. ST Accel. Beams*, **11**, p. 034401, (2008).

[102] Z. Huang, M. Borland, P. Emma, J. Wu, C. Limborg, G. Stupakov, and J. Welch. "Suppression of microbunching instability in the linac coherent light source," *Phys. Rev. ST Accel. Beams*, **7**, p. 074401, (2004).

[103] M. Krasilnikov. Space charge algorithm for the multi ensemble model. *Nuclear Instruments and Methods in Physics Research Section A: Accelerators, Spectrometers, Detectors and Associated Equipment*, 558(1), pp. 69 – 73, (2006).

[104] J. Barnes, TREECODE reference manual (unpublished), available from `https://www.ifa.hawaii.edu/~barnes/treecode/treeguide.html`.

[105] G. Haaf, S. H. W. Wouters, S. B. van der Geer, E. J. D. Vredenbregt, and P. H. A. Mutsaers. "Performance predictions of a focused ion beam from a laser cooled and compressed atomic beam," *Journal of Applied Physics*, **24**, p. 116, (2014).

[106] B. Erdelyi. "The fast multipole method for n-body problems," *AIP Conf. Proc. 1507, 387*, (2012).

[107] Erdelyi B. Abeyratne S., Manikonda S. "A novel differential algebraic adaptive fast multipole method," *Proceedings of IPAC'13*, Shanghai, China, pp. 1055-1057, (2013).

[108] M. Winkel, R. Speck, H. Hubner, L. Arnold, R. Krause, and P. Gibbon, Comp. Phys. Comm., **183**, p. 880, (2012).

[109] J. Qiang and S. Lidia and R. D. Ryne and C. Limborg-Deprey, Phys. Rev. ST Accel. Beams, **9**, p. 044204, (2006).

[110] A. Candel et al., Proc. of 2008 International Linear Accelerator Conference (LINAC08), Victoria, BC, Canada, p. 313 (2008).

[111] C. J. Hirschmugl, M. Sagurton and G. P. Williams, "Multiparticle coherence calculations for synchrotron-radiation emission," Phys. Rev. A **44**, p. 1316, (1991).

[112] R.R. Lindberg and K.-J. Kim. "Collective and individual aspects of fluctuations in relativistic electron beams for free-electron lasers," Proc. of 2012 International Free Electron Laser Conference (WEPD26), p. 421, (2012).

[113] J. Wu, Zh. Huang, and P. Emma, "Analytical analysis of longitudinal space charge effects for a bunched beam with radial dependence," Phys. Rev. ST Accel. Beams, **11**, p. 040701, (2008).

[114] J. Maxson, J. Kiefer H. Lee, A.C. Bartnik, and I. Bazarov. *Phys. Rev. ST Accel. Beams*, **18**, p. 023401, (2015).

[115] Cui Xiohao Jiao Yi. "Generate uniform transverse distributed electron beam along a beam line," *ArXiv:1504.06945 [acc-phys]; submitted to Chinese Physics C*, 2015.

[116] C. R. Prokop, P. Piot, B. E. Carlsten, and M. Church. "Beam dynamics performances and applications of a low-energy electron-beam magnetic bunch compressor," *Nucl. Instrum. Meth.*, A **719**, pp. 17–28, (2013).

[117] F. Lemery and P. Piot. "Ballistic bunching of photoinjected electron bunches with dielectric-lined waveguides," *Phys. Rev. ST Accel. Beams*, 17(11), p. 112804, (2014).

[118] E. L. Saldin, E. A. Schneidmiller, and M. V. Yurkov. "A Simple method for the determination of the structure of ultrashort relativistic electron bunches," *Nucl. Instrum. Meth.*, A **539**, pp. 499–526, (2005).

[119] E. Hoyer, J. Chin, K. Halbach, W. V. Hassenzahl, D. Humphries, B. Kincaid, H. Lancaster, and D. Plate. "The U5.0 undulator for the ALS." *Conf. Proc.*, C910506, pp. 2721–2723, (1991).

[120] S. Reiche. *Nucl. Instrum. Meth. Sec. A*, pp. 429:243, (1999).

[121] A. Saini, A. Latina, A. Lunin, K. Ranjan, N. Solyak, and V. Yakovlev. "Study of Coupler's Effects on ILC Like Lattice." *Conf. Proc.*, C100523, p. THPD088, (2010).

[122] E. A. Peralta *et. al.*, "Demonstration of electron acceleration in a laser-driven dielectric microstructure," *Nature*, **503**, pp. 91–94, (2013).

[123] P. Piot, C. Behrens, C. Gerth, M. Dohlus, F. Lemery, D. Mihalcea, P. Stoltz, and M. Vogt. "Generation and characterization of electron bunches with ramped current profiles in a dual-frequency superconducting linear accelerator," *Phys. Rev. Lett.*, **108**, p. 034801, (2012).

[124] F. Lemery, "Beam Manipulations and Accelerations with Dielectric-Lined Waveguides" Ph.D. Dissertation, Northern Illinois University, DeKalb, IL, USA (2015).

[125] G.G. Manahan, A.F. Habib, P. Scherkl, P. Delinikolas, A. Beaton, A. Knetsch, O. Karger, G. Wittig, T. Heinemann, Z.M. Sheng, J.R. Cary, D.L. Bruhwiler, J.B. Rosenzweig, and B. Hidding. "Single-stage plasma-based correlated energy spread

compensation for ultrahigh 6d brightness electron beams," *Nature communications*, **8**, p. 15705, (2017).

[126] L. Yi, A. Pukhov, and B. Shen. "Direct acceleration of electrons by a CO2 laser in a curved plasma waveguide," *Scientific reports*, **6**, p. 28147, (2016).

[127] C.-Y. Tsai, D. Douglas, R. Li, and C. Tennant. "Linear microbunching analysis for recirculation machines," *Phys. Rev. Accel. Beams*, **19**, p. 114401, (2016).

[128] P. M. Lapostolle. "Effets de la charge d'espace dans un accélérateur linéaire à protons," *Rep. CERN-AR-Int-SG-65-15*, (1965).

[129] I. M. Kapchinsky and V. V. Vladimirsky. "Limitations of proton beam current in a strong focusing linear accelerator associated with the beam space charge," *Proc. Int. Conf. on High Energy Accel.*, p. 274, (1959).

[130] F. Löhl, S. Schreiber, M. Castellano, G. Di Pirro, L. Catani, A. Cianchi, and K. Honkavaara. "Measurements of the transverse emittance at the flash injector at desy," *Phys. Rev. ST Accel. Beams*, **9**, p. 092802, (2006).

[131] C. Gulliford, A. Bartnik, I. Bazarov, L. Cultrera, J. Dobbins, B. Dunham, F. Gonzalez, S. Karkare, H. Lee, H. Li, Y. Li, X. Liu, J. Maxson, C. Nguyen, K. Smolenski, and Z. Zhao. "Demonstration of low emittance in the cornell energy recovery linac injector prototype," *Phys. Rev. ST Accel. Beams*, **16**, p. 073401, (2013).

[132] I. Bazarov, B. M. Dunham, and C. K. Sinclair. "Maximum achievable beam brightness from photoinjectors," *Phys. Rev. Lett.*, **102**, p. 104801, (2009).

APPENDIX

A.1 Space charge algorithm validation

To gain confidence in the algorithm developed we benchamark our simulations in the macroscopic regime and rely on both analytical results and simulations carried out with the ASTRA program [21].

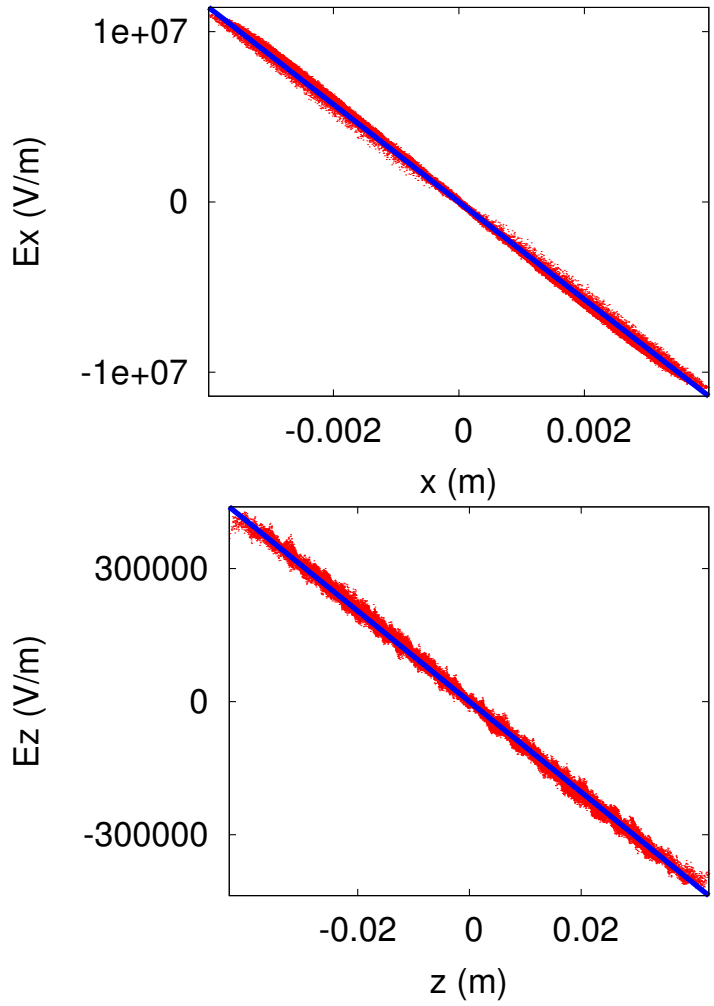

Figure A.1: Transverse (top plot) and longitudinal (lower plot) electric fields experienced by the macropaticle simulated with ELEGANT-BH (symbols) and obtained from Eq. A.1 (lines).

We first consider a 3D homogeneous ellipsoidal bunch with electric field linearly dependent on the position within the charge distribution as [128]

$$\begin{aligned} E_u(u) &= \frac{C}{\gamma^2}\frac{(1-f)u}{r_u(r_x+r_y)r_z}, \\ E_z(z) &= \frac{Cf}{r_x r_y r_z}z, \end{aligned} \tag{A.1}$$

where $C \equiv 3Q/(4\pi\epsilon_0)$, $u \in [x, y]$, $r_{x,y,z}$ are the ellipsoid semiaxes, $f \approx \sqrt{r_x r_y}/3\gamma r_z$ and Q is the bunch charge. The simulated fields are in excellent agreement with the analytical expressions given by Eq. A.1 as shown on Fig. A.1. To assess longer-term tracking, we

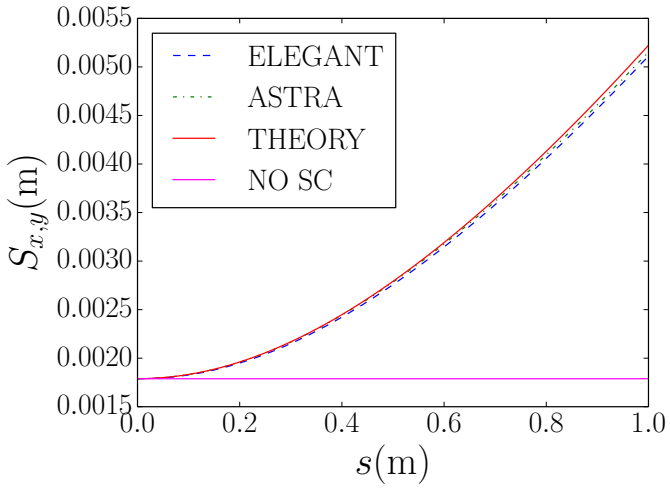

Figure A.2: Comparison of the beam envelope evolution along a 1-m drift. Eq. A.2 solution (red), is compared against ASTRA (green), and ELEGANT-BH simulation (blue). The magenta line corresponds to no space charge case.

compared the evolution of the beam envelope over a drift space. For a stationary uniform beam the transverse envelope evolution is governed by [129]

$$S''_{x,y} - \frac{\varepsilon^2_{rx,ry}}{S^3_{x,y}} - \frac{K_p}{2(S_{x,y}+S_{y,x})} = 0, \tag{A.2}$$

where $S_{x,y}$ is the rms beam size in x, y, $\varepsilon_{rx,ry}$ is the corresponding geometric emittance and K is a space charge perveance defined, for a parabolic current profile, as $K_p \equiv (QI\lambda)/(20\sqrt{5}\pi\epsilon_0 mc^3\gamma^3\beta^2)$ where Q is the bunch charge, I the peak current, λ the RF wavelength, and m the electron mass. Figure A.2 compares the solution of Eq. A.2 against the beam envelope simulated with ELEGANT-BH. The geometric emittance was taken to be very low ($\varepsilon_{x,y} = 1 \times 10^{-11}$ m) for these studies so that when space charge was turned off the beam envelope (dashed line) stayed quasi-constant.

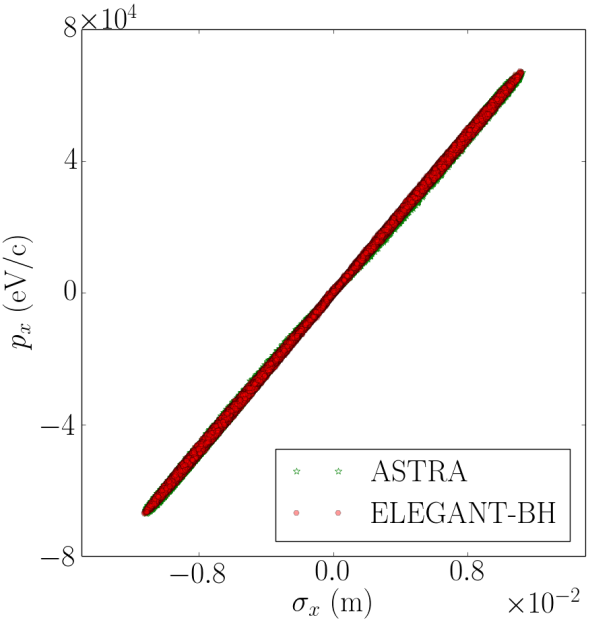

Figure A.3: Comparison of the beam phase space in ASTRA and ELEGANT-BH simulations.

Finally Fig. A.3 compares the final transverse phase space at $s = 1$ m obtained with ELEGANT-BH and ASTRA. These two computer programs despite their very different space charge algorithms are in very close agreement. The code ASTRA relies on the same quasi-electrostatic approximation as used in ELEGANT-BH but implements a cylindrical-symmetric space charge algorithm using a $r - \phi$ two-dimensional grid for depositing the charge and solving Poisson's equation in the bunch frame [21].

A.2 Transverse beam image analysis

Electron beam transverse density images were analyzed using statistical image moments calculation code. In order to compute the moments, we implemented and modified the technique discussed in [13, 130, 131, 132].

A typical beam image background contains white noise that is mostly produced by sporadic X-ray photons generated by the dark current in the beamline. A common recipe to alleviate this noise is to perform a background subtraction, however some portion of it will still be present due to randomness of the dark current induced radiation. This problem is commonly treated by selecting the region of interest for statistical calculation. In our

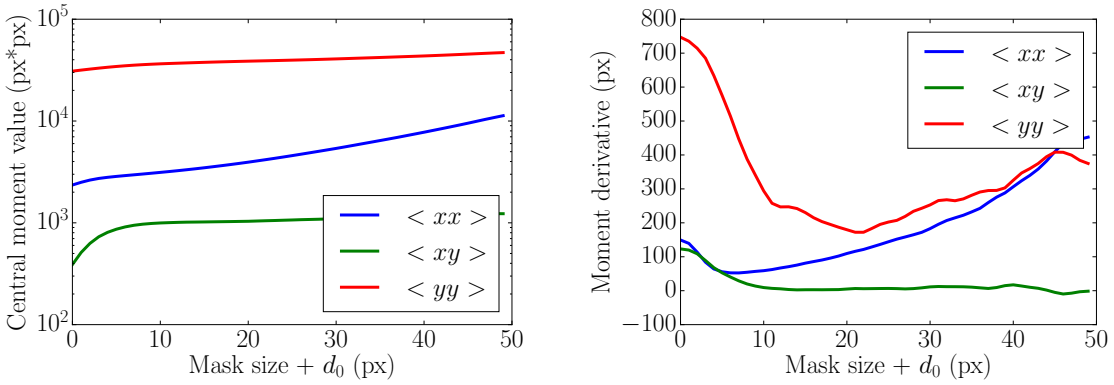

Figure A.4: (left) Calculated beam moments as a function of scanning mask size. (right) Beam moments' derivative as a function of scanning mask size. The minima determine the final region of interest.

method, we start with a small circular region of interest with the size d_0 placed in a center-of-mass of the image. It is then continiously morphed into a three-parametric ellipse and the values of image moments are computed as a function of a scanning mask size. The final mask sizes are determined by the location of the first derivative minima of the moments; see Fig. A.4. These sizes correspond to the area of interest where the signal-to-noise ratio is

the highest. After the areas of interest are determined for each of the beam image moment, the statistical calculation is performed. As an example, Figure A.5 shows an electron beam

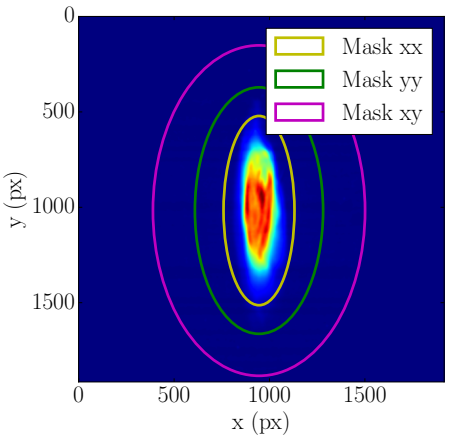

Figure A.5: Example beam image picture and the applied masks for the areas of interest for each image moment.

focused in horizontal plane and the corresponding masks, determined by Fig. A.4 (right). The elliptical shape of the mask is preferred over rectangular as it better mimics the beam shape, therefore improving signal-to-noise ratio. This technique can be easily extened to the case of skew quadrupole scan images, where the beam elliptical masks would be rotated by 45 degrees. Overall, the method demonstrates improved accuracy and reliability in the analysis of various experimental beam images from both AWA and FAST facility.